SANDIA REPORT SAND83—0278 • Unlimited Release • UC—66

Printed July 1983

Modeling and Analysis of Drag-Bit Cutting

SAND--83-0278

DE83 015634

Daniel V. Swenson

Prepared by
Sandia National Laboratories
Albuquerque, New Mexico 87185 and Livermore, California 94550
for the United States Department of Energy
under Contract DE-AC04-76DP00789

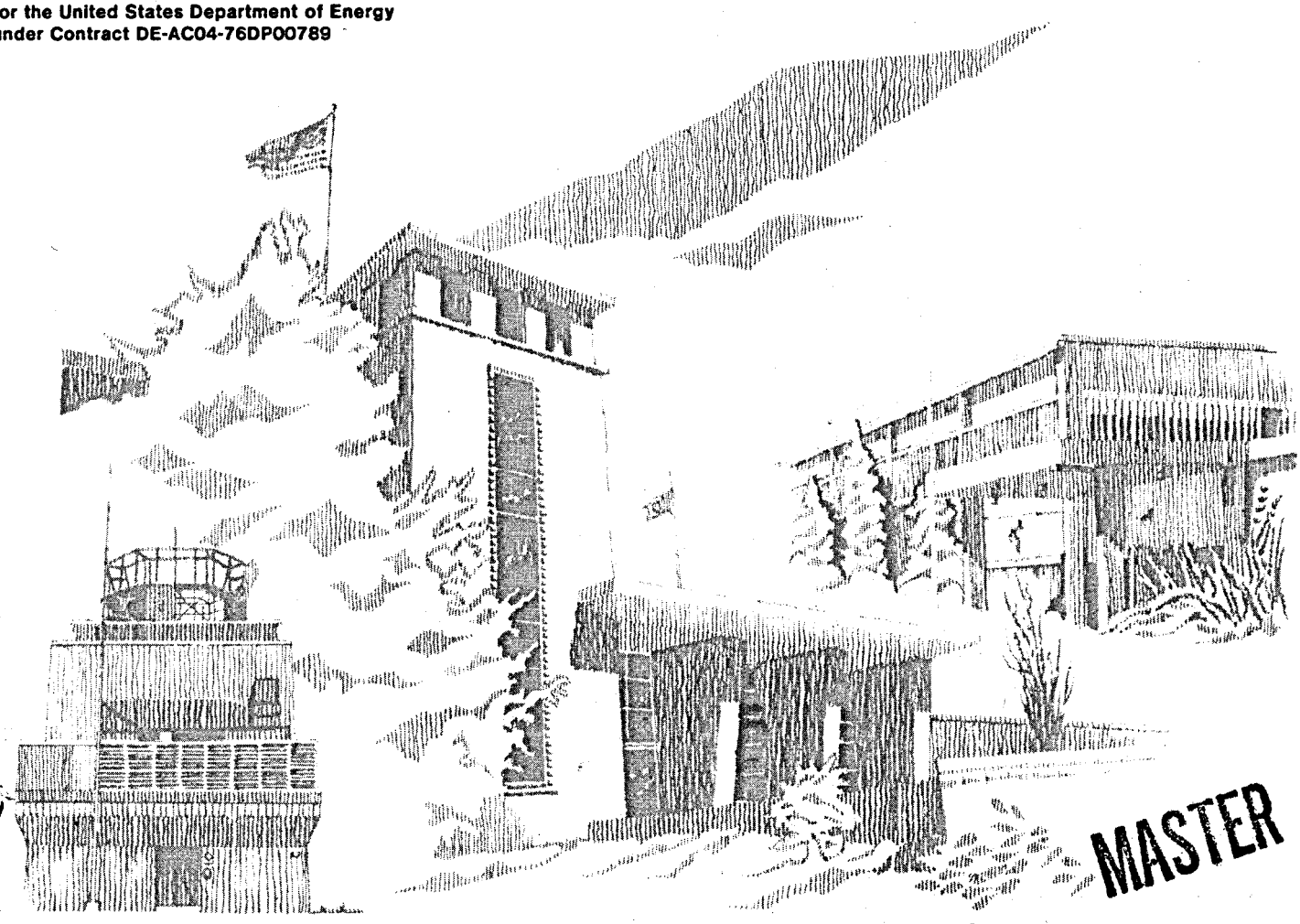

DISCLAIMER

Issued by Sandia National Laboratories, operated for the United States Department of Energy by Sandia Corporation.

Printed in the United States of America
Available from
National Technical Information Service
U.S. Department of Commerce
5285 Port Royal Road
Springfield, VA 22161

NTIS price codes
Printed copy: A05
Microfiche copy: A01

SAND83-0278

MODELING AND ANALYSIS OF DRAG-BIT CUTTING

D. V. Swenson
Division 1524

Sandia National Laboratories
Albuquerque, NM 87185

ABSTRACT

This report documents a finite-element analysis of drag-bit cutting using polycrystalline-diamond compact cutters. To verify the analysis capability, prototypic indention tests were performed on Berea sandstone specimens. Analysis of these tests, using measured material properties, predicted fairly well the experimentally observed fracture patterns and indention loads. The analysis of drag-bit cutting met with mixed success, being able to capture the major features of the cutting process, but not all the details. In particular, the analysis is sensitive to the assumed contact between the cutter and rock.

Calculations of drag-bit cutting predict that typical vertical loads on the cutters are capable of forming fractures. Thus, indention-type loading may be one of the main fracture mechanisms during drag-bit cutting, not only the intuitive notion of contact between the front of the cutter and rock. The model also predicts a change in the cutting process from tensile fractures to shear failure when the rock is confined by in-situ stresses. Both of these results have implications for the design and testing of drag-bit cutters.

Table of Contents

ACKNOWLEDGEMENTS

I am grateful to R. K. Thomas, R. L. Johnson, and L. M. Taylor for their help in developing the constitutive models. This work was supported by the Geothermal/Hydropower Technology Division of the Department of Energy, through J. T. Finger and J. R. Kelsey at Sandia. Atkinson-Noland & Associates performed the material tests, while Division 1542 at Sandia performed the verification tests. The single cutter tests were performed by J. Finger and D. Zeuch.

1.0 - INTRODUCTION

As part of a Department of Energy program to develop new drilling and completion techniques for geothermal wells, Sandia has been involved in the design and development of polycrystalline diamond compact (PDC) bits. One program objective is to develop analysis methods which will allow a rational approach to design and optimization of PDC drill bits.

Initial analyses by Yarrington [1] demonstrated the potential of using computer codes to model the cutting process, including the formation and propagation of fractures. As a continuation of this analytical effort, three tasks were identified:

i) Development of more complete material models including both tensile and shear failures.

ii) Performance of material property tests and prototypic fracture tests to verify the models.

iii) Analysis and laboratory testing of drag bit cutting.

This report documents progress on the above tasks.

The approach which has been taken is to use finite element models to analyze the cutting process. New constitutive models were incorporated into an existing finite element code. Because Berea sandstone samples were readily available, this material was used for verification tests and some drag bit cutting tests. Drag bit cutting tests have also been made on Tennessee Marble and Westerly Granite.

The remaining sections of this report document material property tests on Berea sandstone, describe the Berea sandstone verification tests and analysis, and describe drag bit cutting tests and analysis.

2.0 - BEREA SANDSTONE MATERIAL PROPERTY TESTS

Because Berea sandstone samples were readily available, this rock was used as the reference material for verification and initial drag bit cutting tests. Material property tests were performed to obtain data for the specific material used in the prototypic verification tests. The property tests consisted of uniaxial and triaxial compression tests and Brazilian tensile tests. The tests were performed by Atkinson - Noland & Associates, on whose report [2] this section is based.

Specimens for the material property tests were taken from a single 12 inch cube. For purposes of specimen identifiction, X and Y axes were defined in the bedding plane and the Z axis was defined normal to the bedding plane (Figure 1). Specimens were prepared using an NX size core (diameter approximately 2.140 inches) with a length of approximately 4.25 inches. The Brazilian test specimens were cut to a length of approximately 1.0 inch. The specimens were tested in an air dry state.

Uniaxial compression tests were performed for specimens oriented parallel to all three axes. Table 1 presents results of failure stress, Young's modulus and Poisson's ratio at 50% of peak load, and the failure strain. Figure 2 shows typical plots of axial load vs. axial deformation and lateral deformation vs. axial deformation. The load/deflection curve is nonlinear, with an initial increase in stiffness to an approximately linear region, and then a decrease in stiffness as the failure load is approached. As will be discussed, this same behavior is seen in some of the verification tests.

Triaxial tests were performed at confining pressures of 2000 psi, 4000 psi, 6000 psi, and 7500 psi. For these tests, the axial stress and confining pressures were increased in steps of 2000 psi until the desired confining pressure was reached, at which point the confining pressure was held constant and the axial deviator load increased. Tests were performed only on specimens whose axis was normal to the bedding plane. Results of the triaxial tests are presented in Table 2, including failure stress, Young's modulus and Poisson's ratio at 50% of peak load, and the failure strain. Typical plots of axial load vs. axial deformation and lateral deformation vs. axial load are shown in Figure 3. The load/deformation plot shows a constant residual strength after failure. Figure 4 shows photographs of typical failed specimens at two confining pressures.

Brazilian tensile tests were made by testing in a special apparatus having curved steel loading platens. This diametral point loading of a cylindrical specimen provides an indirect means of obtaining a tensile failure stress. Specimens cored parallel to the Z direction were loaded such that the tensile failure surface would be in the Y-Z plane. Specimens cored in the X and Y directions were tested such that the tensile failure surface occurred in the X-Y plane, i.e., parallel to the bedding plane. Results of the tensile tests are given in Table 3.

The uniaxial tests show that the compressive strength normal to the bedding planes is approximately 30% greater than that measured parallel to the bedding planes. Mohr circles for the average strength values from the uniaxial tests and from the four levels of triaxial confining pressure are plotted in Figure 5. The strength increases with pressure nonlinearly; the rate of increase is less at higher pressures than at low pressures.

The Young's Modulus (E) values determined from the uniaxial tests show a degree of anisotropy with an average E value in the Y direction equal to 1.82×10^6 psi, in the X direction equal to 1.99×10^6 psi, and equal to 2.21×10^6 psi in the Z direction. Stiffness data from the triaxial tests show a higher value of Young's Modulus and lower values of Poisson's ratio than those measured from uniaxial tests. The average value of Poisson's ratio calculated for uniaxial data in the X and Y directions is influenced by several values in the range of 0.50 to 0.69. It is speculated that these high values may reflect the enhanced development of dilatancy along the bedding plane surfaces. Where the effect did not occur, a base elastic value of Poisson's ratio (ν) in the range 0.20 to 0.24 seems justified.

Anisotropy is also evident from the tensile strength data, where it is seen that the tensile strength in a direction parallel to the bedding planes is approximately 13% greater than the strength across the bedding planes.

It should be noted that all values are calculated at 50% of peak load. To illustrate the variation of these properties as a function of stress, values of E, ν, and volume change were plotted versus normalized stress in Figure 6 for the response of triaxial Specimen Z-5-b tested with a 4,000 psi confining pressure. The Poisson's ratio shows a significant increase at the 85% stress level. A plot of volume change shows that the change from elastic response began at stresses greater than 55% of the failure stress. At about 85% of peak stress the material began to exhibit volume increase with load.

3.0 - CONSTITUTIVE MODELS

From the previous section, it is clear that the behavior of Berea sandstone in even relatively simple uniaxial and triaxial tests is complex and highly nonlinear. Any constitutive model will necessarily be a simplification of the true behavior. The minimum requirements for a model which includes crack formation and compressive failure are:

i) An elastic response corresponding to the observed linear portion of the material behavior.

ii) A pressure dependent failure (or yield) criterion in compression.

iii) A cracking criterion in tension.

Two constitutive models were developed which meet these requirements.

Both constitutive models exhibit the same behavior in tension, using a stress criterion to form cracks normal to the maximum principal stress at the element integration points. Failure occurs if the maximum tensile stress exceeds a specified fracture strength (see Section 3.4 for a discussion of the implications of modeling fracture at the constitutive level). In subsequent time steps, the normal and shear stress on the open crack faces are set equal to zero.

The first model acts in compression as an elastic-plastic material. This model (without cracking) was developed by Krieg [3]. The yield surface in principal stress space is described by a surface of revolution with a planar end cap. Plasticity is handled in two parts; a volumetric part and a deviatoric part.

In compression, the second model uses a Coulomb criterion to form explicit shear cracks at the element integration points. In subsequent time steps, the strains normal to both the tensile and shear cracks are monitored to determine if the cracks are open or closed. If a crack is open, the normal and shear stresses on the crack face are set equal to zero. If a crack is closed, a compressive normal stress can be carried, but the shear stress is limited to a value described by the Coulomb friction model.

The HONDO [4] finite element program into which these constitutive models have been added is designed to calculate the large deformation elastic and inelastic transient dynamic response of axisymmetric solids. The program does not form a global stiffness matrix, but instead uses an explicit time integration scheme to solve the problem dynamically so that only a local stiffness is required. For each time step, the element stresses are used to obtain nodal accelerations, the accelerations are integrated to obtain displacements, the element strains are updated, new stresses are calculated, and the cycle is then repeated. Because this approach is very efficient for short time dynamic loading of a continuum, models with a large number of elements can be analyzed at a reasonable cost.

The following three sections give a summary description of the implementation of these constitutive models. More detailed discussions can be found in Swenson and Taylor [5] and Swenson [6]. The last section gives a comparison of the two models and discusses some of the shortcomings of the models. I am greatly indebted to Lee Taylor who allowed me to base these sections on descriptions he had written for one of his reports where he used the same two material models.

3.1 Tensile Failure Criterion

At each material (integration) point in the element, the material is checked for a possible tensile failure. To do this, trial elastic stress increments are calclated for the time step from the strain increments, $\Delta\underset{\sim}{\varepsilon}$ by

$$\Delta\underset{\sim}{\sigma}_{trial} = \underset{\sim}{C}\Delta\underset{\sim}{\varepsilon} \tag{1}$$

where C is the matrix of elastic constants for the material. Only isotropic materials are considered. The trial stresses at the end of the time step are then given by

$$\underset{\sim}{\sigma}^{t+\Delta t}_{trial} = \underset{\sim}{\sigma}^{t} + \Delta\underset{\sim}{\sigma}_{trial} \tag{2}$$

where $\underset{\sim}{\sigma}^{t}$ are the stresses in the previous time step.

Tensile failure is assumed to occur if the maximum principal stress (tension is positive) based on the trial stresses exceeds a specified tensile strength.

$$\sigma_{trial}^{max} \geq T_o \tag{3}$$

If failure occurs, the crack plane is normal to the orientation of the maximum principal stress. Note that failure can occur either in a plane which intersects the R-Z plane (Figure 7.a) or in a plane normal to the circumferential or out-of-plane direction (Figure 7.b). We refer to the out-of-plane cracks as hoop cracks.

After a crack forms, the shear and normal stresses on the crack face are set equal to zero. This is accomplished by rotating the global trial stresses to the crack orientation, modifying the stresses, and then rotating the modified stress back to the global directions.

The strain normal to the crack is used to determine if the crack is open or closed. The normal strain is updated every time step. If a crack closes and the Coulomb model is being used in compression, the crack can carry a compressive normal stress and the shear stress is governed by the Coulomb criterion. If the plasticity model is being used, when a crack closes it heals and all memory of the crack is lost.

3.2 - Plasticity Model

The soils plasticity model used here is a standard material subroutine in the HONDO II code. The model was derived and coded by Krieg [3].

A yield surface is assumed for the material which is a surface of revolution about the hydrostat in principal stress space, as shown in Figure 8. The radius of the surface about the hydrostat is taken to be a quadratic function of the mean pressure, p, defined as

$$p = -\frac{1}{3}(\sigma_1 + \sigma_2 + \sigma_3) \tag{4}$$

The plasticity model includes both deviatoric and volumetric plasticity. The volumetric plasticity defines the position of the end cap on the normally open end of the surface of revolution.

The yield surface is most easily described as two functions, one describing the parabaloid and one describing a plane which is normal to the hydrostat.

$$\theta_s = J_2 - (a_0 + a_1 p + a_2 p^2) \tag{5}$$

$$\theta_p = p - f \tag{6}$$

where p is again the mean pressure (positive), a_0, a_1, and a_2 are material constants and J_2 is the second invariant of the deviatoric stresses, S. The quantity, f, is a function of the mean volumetric strain and defines the volumetric stress-strain curve for the material, as shown in Figure 9.

The strain increment, which includes corrections to account for crack opening strains, is decomposed into a mean volumetric strain increment, $\Delta\varepsilon_v$ and a deviatoric strain increment, $\Delta\underset{\sim}{e}$,

The plasticity theories for the volumetric and deviatoric parts are now taken to be completely independent. The volumetric part is treated first.

The mean volumetric strain is first updated as

$$\varepsilon_v^{t+\Delta t} = \varepsilon_v^{t} + \Delta\varepsilon_v \tag{7}$$

A check is then made to see if

$$\varepsilon_v^{t+\Delta t} > \varepsilon_u \tag{8}$$

where ε_u is the most negative volumetric strain previously experienced by the material (initialized to zero). If equation (8) is satisfied, the step is elastic and,

$$p^{t+\Delta t} = p^{t} - k_o \Delta\varepsilon_v \tag{9}$$

where K_o is the elastic bulk modulus for the material. If equation (8) is not satisfied,

$$p^{t+\Delta t} = f(\varepsilon_v{}^{t+\Delta t}) \tag{10}$$

and we set

$$\varepsilon_u = \varepsilon_v{}^{t+\Delta t} \tag{11}$$

The deviatoric part uses almost conventional plasticity theory. The deviatoric stress rate is written as a function of the deviatoric strain rate in a manner which is consistent with the constitutive assumptions in the plasticity model. These include the assumption that the total strain rate is decomposed into an elastic and plastic part, that linear elasticity is used for the elastic part, and that the plastic part is given by a normality condition.

$$\dot{\underset{\sim}{S}} = 2\,G\,\dot{\underset{\sim}{e}} - \frac{2\,G\,\underset{\sim}{S}\cdot\dot{\underset{\sim}{e}} - (a_1 + 2a_2 p)\,\dot{p}}{\underset{\sim}{S}\cdot\underset{\sim}{S}} \tag{12}$$

Assuming that the deviatoric strain rate, e, is constant throughout the time step, equation (12) can be integrated exactly so that the final stress state lies on the yield surface. The details of this exact integration are found in Krieg [3].

3.3 - Coulomb Failure Criterion

In this compressive failure model, explicit shear cracks are assumed to form at the element integration points. The Coulomb criterion assumes that the shear stress tending to cause failure across a plane is resisted by a cohesion of the material, S_0, and a linear function of the normal stress across the plane (Jaeger and Cook [7]).

$$|\tau| > S_0 + \mu\,\sigma_n \tag{13}$$

Where τ and σ_n are the shear stress and normal stress across the failure plane. The coefficient of internal friction for the material is denoted by μ. Only $|\tau|$ appears in equation (13) because the sign of τ only affects the direction of sliding.

The cohesion and the unconfined compressive strength of the material, C_0, are related by

$$S_o = \frac{C_o}{2[(\mu^2+1)^{1/2} + \mu]} \qquad (14)$$

When shear failure occurs, two cracks form simultaneously in the two equally probable shear directions inclined at angles $\pm \alpha$ on either side of the minimum (most compressive) stress direction

$$\alpha = \pm \frac{1}{2} \tan^{-1} (1/\mu) \qquad (15)$$

Figure 10 illustrates the Coulomb criterion pictorially using a Mohr circle representation. The radius of the circle is the principal (maximum) shear stress. When the stress state changes so that the Mohr circle touches the failure line, shear cracks form. In fact, there are three different Mohr circles which can be drawn which correspond to possible failure in the three different planes shown in Figure 11.

After a crack has formed, the state of stress is modified according to the Coulomb stress criterion. Crack opening strains are monitored and if the crack is closed, the Coulomb criterion is used to calculate the shear stress on the crack face.

3.4 Comparison and Limitations of the Two Models

A three-dimensional representation in principal stress space of the failure surfaces for both models is shown in Figure 12. The soils plasticity model is identical to a classical Von Mises elastic-plastic theory if the coefficients a_1 and a_2 of equation (5) are set to zero and an elastic volumetric response is used. Then the yield surface is just a cylinder parallel to the hydrostat. The Coulomb model becomes the same as a Tresca maximum shear stress theory if μ is zero in equation (13).

A comparison of the post failure response predicted by each model is easily understood in the context of a compression test. Figure 13.a illustrates (schematically) the post failure behavior predicted by both models for an unconfined compression test. Figure 13.b illustrates (schematically) the predicted post failure behavior at some confining pressure, p_o. As can be seen, after the failure the Coulomb model behaves essentially as a granular material capable of sustaining load only when confined.

One limitation of the model is the use of a stress criterion rather than a fracture mechanics criterion for crack propagation. For many geologic materials, linear elastic fracture mechanics appears applicable (see, for example, Saouma, Ingraffea, and Catalano [8] and Schmidt and Huddle [9]). Assuming linear elastic fracture mechanics is appropriate for this application, solutions obtained using a stress criterion become mesh size dependent. This problem occurs because of the stress singularity at a crack tip, where the analytic elastic solution predicts an infinite stress for a sharp crack. As the mesh size is reduced, the finite element calculation captures the stress singularity better (i.e., the element stresses at the crack tip become larger as the mesh size is reduced). As a result, the crack is predicted to grow under lower loads as the mesh is reduced. In the limit, the solution does not converge to the theoretical solution, but instead predicts the crack will propagate under zero load.

Since both the fracture mechanics and stress criterion approaches use the same method to predict crack initiation (for the fracture approach, the initiation stress is calculated by assuming a flaw size) the difference in the two approaches arises during crack propagation. It can be argued that a stress criterion is adequate for materials which have universally distributed flaws (i.e., many geologic materials). The tensile strength of these materials is low (because of the inherent flaws) and, therefore, from a global perspective, tensile stresses cannot carry significant loads and do not contribute significantly to the total internal energy of the structure. As a result, the overall response of the structure can be predicted using a stress criterion, although the detailed location and lengths of the fractures cannot be expected to be accurately predicted. A stress criterion also seems generally adequate for geologic problems where an in-situ stress exists. For this class of problems, the energy required to propagate a crack is much less than the energy required to open the crack against the combining stress, and so the fracture criterion becomes less important.

A second limitation of the model is that, because of displacement continuity in the finite element formulation, failure at fewer integration points is needed for a crack to extend parallel to the mesh lines than to extend diagonally across the mesh. As a result, cracks preferentially extend parallel to the element mesh lines. This does not preclude the possibility of cracks turning and running diagonally across the mesh, as is seen in some of the analyzed cases, but the orientation of the finite element discretization does have some effect on the orientation of the resulting crack pattern.

4.0 - INDENTION VERIFICATION TESTS

4.1 Experiments

Indention tests were performed on block samples of Berea sandstone to provide one method of verifying the computer model. Indention tests were chosen based on Hood's observation [10] of a good correlation between actual drag bit cutting and simulation by idention. Thus, failure of rock by indention should be similar to the actual cutting failure.

In the tests, a flat indentor (1 inch wide and 6 inches long) loaded the block specimen (3.75 inches x 3.75 inches x 6 inches long) which rested on a flat surface. All specimens were loaded with the bedding plane horizontal (parallel to the bottom support). Two levels of lateral pre-stress were applied to the specimens: 0.0 psi and -2100 psi. Preload stresses were applied by clamping the specimen between bolted steel blocks and were intended to simulate in-situ stress effects.

Measured data included the load and displacement of the indentor, strains on the end surface of the block at the centerpoint, and acoustic emissions during the tests. Three tests were performed at 0.0 psi pre-stress and two tests were made with a pre-stress of -2100 psi. The indentor was displaced slowly, so that failure occurred after several minutes.

Results of the unconfined indentor tests are presented in Figures 14 through 17. Figure 14 shows the test configuration and typical post-test fractures visible to the naked eye (see Figure 25 for a photograph). Unfortunately, the Berea sandstone was so porous that use of penetrants to observe fractures was impossible. Visual inspection of the top surface indicated a small permanent deformation under the indentor. The asymmetry in fractures was caused by the test machine. Although the loading platens appeared parallel, fracture consistently occurred first on the same side of the machine, indicating some non-uniform loading.

The measured loads as a function of indentor displacement are given in Figure 15. As was noted for the uniaxial material tests, the response is nonlinear with an initial stiffening. In general, the tests show good repeatability, failing at similar loads. The unloading curves support the conclusion that some permanent deformation occurred under the indentor, since zero load is reached for a positive indentor displacement.

The strains measured at the center of the end of the specimen for test #1 are shown in Figure 16. Again, the unloading measurements are consistent with some permanent deformation. The lag in strain when the indentor was initially displaced would appear to indicate some initial "settling in" of the indentor. This would be at least partially responsible for the increasing stiffness in the load/displacement response.

Acoustic emissions were also measured during the tests. Figure 17 shows the count as the indentor displaced for test #1. A large increase in emission rate occurred just before failure. This is consistent with visual observations during the test, where no cracks were observed until a rapid failure occurred.

Corresponding data for the tests with pre-stress are presented in Figures 18 through 21. The most obvious difference caused by pre-stress is the elimination of the long fractures extending through the specimens (See Figure 31 for a photograph). Instead, fractures were limited to the upper portion of the specimen and crushing occurred under the indentor. Pre-stress also increased the failure load to approximately twice the unconfined case. Peak strains did not increase, but were similar to the unconstrained case. For the pre-stressed case, the acoustic emission count shows more initial activity and a smoother increase.

All the above observations are consistent with intuition. The peak load increased under pressure and fractures (presumably tensile) were reduced under confining stress.

4.2 - Analysis

Analysis of the indention experiments was performed using both material models described in Section 3. Figures 22 and 28 show the finite element discretization of the problem (because of symmetry, the calculation was made using only one-half of the specimen). Contact between the rock (shown in red) and the steel components (shown in green) was represented using slide lines with a friction coefficient of 0.6. Plane strain assumptions were used. The specimens were loaded by displacing the indentor downward at a constant velocity chosen to be slow enough to give an essentially static solution. For the case with pre-stress, the specimen was given an initial lateral stress and then the restraining plates were fixed on their outer surfaces.

Material properties used in the analysis are given in Table 4. These properties are based on the material data

obtained in Section 2. The only value changed from the test data is the tensile strength, which was increased from the measured value of approximately 400 psi to 850 psi. The reasons for this are discussed below.

Calculated results for the unconfined test are given in Figures 23 through 27. The calculated fracture patterns are shown in Figures 23 and 24 for both material models. For the tensile/Coulomb model (Figure 23), yellow fractures indicate tensile cracks while magenta fractures indicate shear cracks. Comparing the calculated fractures to the photograph (Figure 25) shows a good correlation. Before the test was run, it was hypothesized that a central fracture would form under the indentor, rather than the two fractures extending from the indentor corners. In the analysis, a central crack did form if the tensile strength was reduced to 400 psi. Elasticity solutions for an indentor indicate tensile stresses under the indentor. This was also indicated in the finite element calculation. The reason a central fracture did not form in the tests is likely due to the sharp corners of the indentor. These probably initiated small cracks which then propagated downward. The finite element model does not have these sharp corners, thus there is the greater tendency to form a central crack. This question is also related to the use of a stress criterion to form cracks rather than a fracture mechanics criterion.

Figure 26 compares the calculated and measured indentor load/displacement curves. As expected from the linear approximation to the nonlinear material data, the initial calculated response is linear and does not exhibit the stiffening effect observed in the uniaxial tests. The calculated curves have been shifted to bring the "linear" regions closer together. Once a significant amount of fracturing occurs under the indentor, the load predicted using the tensile/Coulomb model drops off as material flows from under the indentor toward the unconfined free surface. This does not occur with the tensile/plasticity model, where the load continues to increase with displacement. The two models thus provide upper and lower estimates of the load (admittedly very large bounds).

A comparison of measured and calculated strains is shown in Figure 27 (shifted the same amount as in Figure 26). The calculated lateral strains are smaller than measured, while the vertical strains are similar to those measured. It should be recalled that strains were measured on the surface, while the calculated values represent interior values. The difference between surface and interior strains is not known. The tensile/Coulomb material model results reflect the drop in load that occurs after failure.

Figures 29 through 33 show corresponding results for the pre-stressed tests. The correlations with test results are similar to the unconfined case. The fracture patterns for the pre-stressed case were not sensitive to material parameters, similar results (i.e., crushing under the indentor) were obtained for a wide range of values.

4.3 - Discussion

Results of the previous section show both the shortcomings and capabilities of the finite element analysis. The predicted fractures correlate fairly well with experiment. For the pre-stressed case, the results are not sensitive to the fracture criterion, but for the unconfined case, there is some sensitivity. Because the corners of the indentor did not start sharp cracks, fracture down the center of the specimen was predicted using measured values of tensile strength. Calculations performed with a higher tensile strength did not form a central crack. The predicted loads bound the measured values, with the tensile/Coulomb model under-predicting loads and the tensile/plasticity model over-predicting loads. The reason for the different behavior is a result of the post-yield (post-failure) assumptions in the two models. The plasticity model maintains a post-yield strength, while the Coulomb model maintains strength after fracture only as long as the material is confined.

Based on these results, it would seem appropriate to use the models for analysis of drag bit cutting. However, we should not expect detailed correlation between the analysis and test. We can expect the analysis to indicate sensitivities to parameter changes in a manner similar to the changes predicted for the indention tests as the pre-stress was varied.

5.0 - DRAG BIT CUTTING

The objective of developing analytical tools is to make possible modeling of the cutting, leading to a more rational (and improved) approach to the design of drills and bits. Sandia's specific interest is the developement of polycrystalline diamond compact (PDC) bits. Figure 34 illustrates a single cutter consisting of a polycrystalline diamond facing on a tungsten carbide substrate attached to a mounting stud. Several cutters are then used to form a drill bit (Figure 35).

As a first step in solving this problem, single cutter tests were performed in the laboratory with corresponding analyses. Analyses have also been made for in-situ stress conditions which were not duplicated in the laboratory. Both the experiments and analyses are described in the following sections.

5.1 - Experiments

Single drag bit cutter experiments have been made using a modified milling machine (Figure 36). A single cutter is mounted in the machine head and forces on the cutter are measured in the thrust (parallel to cutter displacement), lateral, and vertical directions. The tests are conducted by mounting the specimen on the machine, fixing the cutter depth of cut relative to the rock surface, and then feeding the rock past the cutter. Figure 37 shows the cutter actually used for the tests. The rake angle for all tests was -20°. An artificial wearflat was ground on the cutter to simulate typical conditions after some use. Data consists of visual observations, high speed movies, cutting forces, and post-test examination of the specimen.

A typical chip formation sequence (for a worn cutter) is illustrated in Figure 38. As cutter moves into the rock where a chip has previously been removed, it levels the uneven rock and creates a large amount of dust. Some of the material is trapped between the cutter and the rock, leading to relatively large loads in fixed cutting depth experiments. At some point, the thrust and vertical loads become large enough that horizontal and dipping fractures form ahead of the cutter. The horizontal fractures form a chip which flys away and the cycle is repeated. This general sequence has also been observed by Hood [10], Fairhurst [11], and Friedman [12].

The cyclic nature of the cutting process is reflected in both the post-cutting fractures observed in the specimen and in the measured cutting forces. Figure 39 shows a photograph of a Tennessee Marble specimen which has been sliced and dye penetrated to highlight the fractures (in order to observe fractures, it was necessary to use a less porous rock type than sandstone). The subsurface damage is characterized by numerous fractures that consistently dip in the direction of cutter displacement, at angles ranging from quite shallow to 50°-60°. There is no observable shear displacement across the fractures, indicating that they are tensile in character. Sections made from Westerly Granite and Tennessee Marble specimens show similar fracture patterns. It is believed that essentially the same mechanisms operate in Berea Sandstone.

Measured cutting forces are shown in Figures 40 through 42. The forces represent variations in cutting depth and rock type. Figure 40 gives forces for cutting Berea sandstone at a depth of 0.050 inches while Figure 41 shows forces for a cutting depth of 0.100 inches. Both the peak and average forces approximately double when depth is doubled. It is also interesting to note that the vertical forces are the same magnitude as the thrust force. This indicates the cutting is not a clean knife-like operation, but that there is considerable grinding of the rock under the cutter. This is confirmed by visual observation of the specimens, where fine powder appears forced into the cutter path. The change to a stronger rock type (Tennessee Marble) increases the cutting loads significantly. For the marble, the vertical loads even exceed the thrust load. The measured loads for both rock types show a definite periodicity which appears related to the formation of major fractures. There is a rise in load followed by a sharp decrease. Comparing the distances between force cycles (Figure 42) and the distance between major fractures (Figure 39), there is a definite correlation with a cycle occurring about every 0.2 inch. By varying the cutter speed, we have shown that the cyclic response is not related significantly to the stiffness of the experiment fixture.

To summarize, laboratory tests at atmospheric pressure and fixed cutting depth show a definite cyclic process of cutter engagement, chip formation, and movement into the cleared zone.

5.2 - Analysis

Using the previously developed material models, calculations were made of the drag bit cutting process. The mesh used to analyze cutting is shown in Figure 43. The worn cutter configuration was approximated in the analysis with a rake angle of -20°. The friction coefficient on the slide

lines between the cutter and the rock was assumed either zero or 0.25. While performing the calculations, it became obvious that the assumed contact pattern between the cutter and the rock was an important parameter. Two meshes were used, one in which the rock surface was flat and one where 0.025 inches of rock was in direct contact with the cutter, with the rest of the cutting depth angling away from the cutter. Plane strain assumptions were used. Table 4 gives the material properties used in the analyses, and Table 5 gives the different cases examined.

For the first study, the rock surface was assumed flat and the cutter was displaced first downward, then forward. This loading is similar to an indention test. The tensile/Coulomb model with sandstone properties was used. Figure 44 shows the sequential fracture pattern for 0.001 inches vertical displacement; the results for 0.002 inches vertical displacement are given in Figure 45. The calculated forces are given in Figure 46. For the 0.002 inch vertical displacement case, the vertical loads drop due to fracturing under the cutter before the cutter is displaced forward. Both cases show a significant drop in vertical load when forward displacement starts.

It is clear that between 0.001 and 0.002 inches displacement, the vertical load becomes large enough to cause significant fracturing. In fact, the fractured region has many of the same characteristics as the experimentally observed fractures during cutting; the major fractures dip away from the cutter and there is a region of considerable damage under the cutter. This also correlates with Hood's observations [10] that indention caused fractures similar to those obtained in drag bit cutting. Thus, it appears that the vertical loads during cutting are sufficient to cause fracturing of the rock and so indention may actually be a significant drag bit cutting mechanism. The actual chip forming process is therefore more complex than the intuitive notion of drag bits forming chips only as a result of contact between the front face of the cutter and the rock.

The next study was an attempt to simulate laboratory cutting experiments on sandstone. This study modeled in increasing detail the assumed contact pattern between the cutter and the rock.

The first calculation assumed that 0.025 inches of the 0.100 inch cutting depth was in contact with the cutter. The cutter bottom was assumed flat and in contact with the rock. The cutter was displaced with a constant forward velocity of 10 in/sec; the vertical displacement was zero. This calculation was made with both the tensile/Coulomb material model (Figure 47) and the tensile/plasticity model (Figure 48).

Both models give similar predictions of fracture location. They both drive a long fracture ahead of the cutter and a vertical fracture down from the cutter. The material in front of the cutter is fractured in the tensile/Coulomb model, but remains unfractured (but plastically deforming) in the tensile/plasticity calculation. The forces follow the same pattern noted in the indentor calculations; the tensile/plasticity model predicts forces (Figure 49) that continue to increase, while the tensile/Coulomb model shows a peak force which then drops as the material in front of the cutter is crushed. Both models predict a tensile fracture extending downward from the cutter. This fracture is a consequence of both the assumed cutter/rock contact and the tendency of the model to propagate fractures along mesh lines. Accordingly, it was decided to examine further the consequences of changing the detailed assumptions of contact between the cutter and the rock using the tensile/Coulomb model.

Based on experimental observations, crushed rock is smeared under the cutter as the cutter displaces. This powdered rock tends to diffuse the contact between the cutter and the rock. Also, this powdered rock would be expected to be of lower strength than the intact rock. This effect was approximated in the model by locally reducing the failure strengths of the elements in contact with the cutter (See Figure 43.b). The strength in the four elements ahead and underneath the cutter were reduced by a factor of five. Figure 50 shows the resulting fractures. Comparing these results to Figure 47, the most noticeable effect of the local softening is to cause a fracture dipping at 45° ahead of the cutter. This is expected, since the locally weak material gives a pressure-type loading between the cutter and the rock, which would enhance the 45° fracture.

A third step in the study was to impose a vertical displacement on the cutter before displacing the cutter forward. Figure 51 shows the fractures for an initial downward vertical displacement of 0.001 inch, followed by forward motion. Because of compression under the cutter, the vertical fracture does not form, but both forward and dipping fractures do form. A trailing fracture is also formed by indention of the rear edge of the cutter.

The final step in making the contact assumptions closer to the actual case was to include some slope in the cutter wear flat. It was observed that wear flat of the cutter used in the experiments was not truly horizontal, but was tilted at an angle of $\approx 7°$ with the horizontal. This corresponds to approximately a 0.022 inch relief from front to back over the 0.18 inch long wear flat. In the analysis, a smaller tilt of

0.001 inch front to back was used. This smaller tilt provided qualitatively better answers than the measured tilt. Figures 52 and 53 show the results of these calculations for both material models. In general, there is qualitative agreement with the fractures observed in post-test examination (Figure 39). First, fractures extend ahead of the cutter in a manner that would be expected to form a chip. Second, there is a dipping tensile fracture ahead of the bit at an angle of approximately 45°. Third, there is considerable damage locally under the bit. The vertical fracture is the only fracture that does not correspond to observations, and is probably a result of the tendency of the model to predict fractures parallel to mesh lines.

Figure 54 shows the thrust and vertical forces for the above cases. In general, the thrust force did not change from case to case, but the vertical forces increased for the cases with a downward vertical cutter displacement.

A comparison of the forces for both material models in the final loading configuration is given in Figure 55. The magnitudes of the vertical forces are approximately the same as the horizontal forces. The calculated forces are approximately one-half measured values. Note that in Figure 55, the forces are represented for a cutter width of 1 inch. Normalizing this to the measured cutter width of 0.3 inches results in peak forces of 180 to 240 lbs. This compares with peak measured values of approximately 550 lb (Figure 40). The tensile/Coulomb model shows a drop in horizontal force as fractures form while the tensile/plasticity model predicts forces that continue to increase with displacement (although at a reduced slope).

Using this final configuration, three sensitivity studies were made using the tensile/Coulomb model:

1. Changing the rock type to Tennessee Marble.

2. Changing the sandstone cutting depth to 0.050 inch.

3. Applying a uniform pressure on the rock surface of 3000 psi with corresponding uniform initial hydrostatic in-situ stresses of -3000 psi.

The fracture patterns for Tennessee Marble are shown in Figure 56. They are similar to the sandstone fractures, but with a reduced dip fracture and an enhanced vertical fracture. The forces for marble (Figure 57) are approximately twice as large as the sandstone forces. This trend is in the right direction, however, the observed ratio of marble to sandstone thrust forces is approximately three and one-half. Thus, the model underestimates the effect of changing materials.

The effect of varying cutting depth is shown in Figure 58. The fractures are similar to the 0.100 inch cutting depth. The calculated forces are also similar (Figure 59), with a 0.050 inch depth peak force of 500 lb compared to a 600 lb peak force for a cutting depth of 0.100 inches. This change in cutting force is less than that observed experimentally, where the force dropped approximately in half for a factor of two reduction in depth.

Including in-situ stresses with a confining pressure has a marked effect on the results. First, all tensile fractures are inhibited and only shear fractures occur (Figure 60). This indicates a change in the drilling process when the rock is confined. This type of change in behavior from a brittle response to a plastic response was noted by Maurer [13] for indention tests. Secondly, cutting forces approximately doubled for the confined case (Figure 61). This change in response seems reasonable and could have significant implications for testing. If the fracture mechanisms change with confinement, tests performed at atmospheric pressure probably have little correlation with actual drilling conditions. Thus, we should be cautious about applying atmospheric test data to the design.

5.3 - Discussion

From the previous results, it is clear that detailed fracture predictions are sensitive to the assumed contact between the cutter and the rock. Because of this sensitivity, it is not appropriate to expect the model to correctly predict individual fractures. The model is useful predicting overall behavior and the effects of major changes in loading conditions.

The most significant result with respect to overall behavior is the ability of the vertical loads to form fractures. This leads to the conclusion that indention-type loading is probably one of the main drag bit cutting mechanisms, and not only contact between the front of the cutter and the rock. Note that the analysis and experiments were performed with a worn cutter. For sharp cutters, it is not clear that the same indention fractures will form. On one hand, the observed vertical and thrust forces are lower, on the other hand, fractures will form at lower loads as one approaches a point load.

With respect to the effects of changing loading conditions, the most important result is the effect of in-situ stresses and pressure on the rock surface. The model predicts a change in the cutting process from a tensile fracture process to a shear (plasticity) process when confined. This change in behavior appears correct intuitively and is also supported by the successful application of the model to the confined indention test.

6.0 - CONCLUSIONS

In this report, I have attempted to present a fairly complete picture of analytical work to date. The analysis has met with mixed success, being able to capture some features of the cutting process, but not all.

Part of the difficulty lies with modeling the material behavior. As shown in Section 2.0, the response of Berea Sandstone in even relatively simple uniaxial and triaxial tests is complex and highly nonlinear. The "elastic" properties are load dependent and failure is progressive, beginning at relatively low loads.

The constitutive models used to represent the material are necessarily simplifications of actual behavior (Section 3.0). They also include some theoretical shortcomings, such as use of a stress criterion for crack propagation. However, despite these limitations, verification analyses of indention tests correlated fairly well with observations (Section 4.0). Fracture patterns matched those obtained experimentally and calculated loads bounded the measured values.

The analysis of drag bit cutting has the added complication of requiring assumptions about contact between the cutter and the rock (Section 5.0). It was shown that the results were sensitive to this assumption. This necessity of assuming contact appears to be the major stumbling block to developing analysis methods which can model the cutting process in detail. Even if all the other limitations of the model were removed, this problem would still remain. The only apparent way to eliminate the need to assume contact is to have the cutter move a significant distance (several inches) in the analysis. This requires the ability to form and eject chips and to include the crushing of the rock under the cutter. Conceptually this is achievable with either a remesh capability or Eulerian approach, but the problem size and required computing time is formidable.

The present analysis is not without value, however. The model has the capability to predict overall behavior and the effects of major changes in loading.

The most significant result with respect to overall behavior is the prediction that vertical loads form fractures. This leads to the conclusion that indention-type loading is probably one of the major fracture forming mechanisms during drag bit cutting, not only contact between the front of the cutter and the rock. It thus appears that cutter life could be extended by improving the capability of cutters to withstand significant vertical and bottom shear loads, with a reduced emphasis on the front face of the cutter.

With respect to the effects of changing loading conditions, the most important result is the effect of in-situ stresses and pressure on the rock surface. The model predicts a change in the cutting process from a tensile fracture process to a shear (plasticity) process when confined. This change in behavior appears intuitively correct and is also supported by the demonstrated successful application of the model to the confined indention test. The change in cutting process has implications for both testing and design. If the cutting process at atmospheric pressure is not the same as when confined, the applicability of atmospheric test data is questionable. Tests under confined conditions would most closely represent actual conditions.

7.0 - RECOMMENDATIONS FOR FUTURE WORK

Many areas of research hold the potential of improving polycrystalline diamond compact cutters performance. In addition to the long-term type of research described in this report, work on failure oriented design improvements should be (and is being) pursued. Such areas include improving stud design to withstand peak loads, developing better methods of cooling cutters, and increasing thr wear resistance of the studs.

With respect to research into the mechanics of cutting, the present situation is such that laboratory tests do not simulate actual cutting conditions, and the model is least reliable at laboratory test conditions (atmospheric pressure). It is expected that the present model is most applicable to actual drilling conditions, where the rock is confined by drilling mud. Therefore, a primary objective should be to bring the laboratory test conditions closer to actual drilling conditions. Comparisons should then be made betwen the model and tests under simulated cutting conditions. It would also be useful to gather data on successful applications of PDC cutters and then relate laboratory tests and analysis to these conditions. I would recommend postponing further model developments until confined cutting data is available and comparisons are made using the present model.

8.0 - REFERENCES

1. S. G. Varnado, C. F. Huff, and P. Yarrington, "The Design and use of Polycrystalline Diamond Compact Drag Bits in the Geothermal Environment," 54th Annual Fall Conferences of the SPE of AIME, Las Vegas, Nevada, September, 1979.

2. "Constitutive Relations of Berea Sandstone," Atkinson-Noland & Associates, Boulder, Colorado, January, 1981.

3. R. D. Krieg, "A Simple Constitutive Description for Cellular Concrete," SC-DR-72-0883, Sandia National Laboratories, Albuquerque, NM, available from author.

4. S. W. Key, Z. E. Beisinger, and R. D. Krieg, "HONDO A Finite Element Computer Program for the Large Deformation Dynamic Response of Axisymmetric Solids," SAND78-0422, Sandia National Laboratories, Albuquerque, NM, October, 1978.

5. D. V. Swenson and L. M. Taylor, "A Finite Element Model for the Analysis of Tailored Pulse Stimulation of Boreholes," to be published in Int. Journal of Numerical and Analytical Methods in Geomechanics.

6. D. V. Swenson, "Implementation of Two Geologic Constitutive Models in the HONDO Finite Element Code, SAND83-0238, Sandia National Laboratories, Albuquerque, NM, to be issued.

7. J. C. Jaeger and N. G. W. Cook, "Fundamentals of Rock Mechanics," Third Edition, 1979, Chapter 4.

8. V. E. Saouma, A. R. Ingraffea, and D. M. Catalano, "Fracture Toughness of Concrete - K_{IC} Revisted," Report 80-9, Department of Structural Engineering, Cornell University, Ithaca, NY, October, 1980.

9. R. A. Schmidt and C. W. Huddle, "Effect of Confining Pressure on Fracture Toughness of Indiana Limestone," International Journal of Rock Mechanics and Mining Science, Vol 14, 1977, p. 289.

10. M. Hood, "A Study of Methods to Improve the Performance of Drag Bits Used to Cut Hard Rock," Chamber of Mines of South Africa, Mining Technology Laboratory, Project No. 6T2 No. 2, Report No. 35/77, August, 1977.

11. C. Fairhurst, W. D. Lacabanne, "Hard Rock Drilling Techniques," Mine & Quarry Engineering, April, 1957, pp. 157-161.

12. M. Friedman, "Analysis of Rock Deformation and Fracture Induced by Rock Cutting Tools Used in Coal Mining," SAND83-7007, Contractor Report, prepared for Sandia National Laboratories, Albuquerque, NM, March, 1983.

13. W. C. Maurer, "Bit-Tooth Penetration Under Simulated Borehole Conditions," Journal of Petroleum Technology, December, 1965, pp. 1433-1442.

SPECIMEN	FAILURE STRESS-psi	MODULUS E, x 10^6 psi	POISSON'S RATIO	FAILURE STRAIN, %
X-1-a	7500	1.98	0.20	0.53
X-2-a	7290	1.98	0.33	0.54
X-3-a	7640	2.02	0.65	0.56
X-3-b	7170	1.94	-	0.54
X-4-a	7290	2.01	0.61	0.54
Avg.	7380	1.99	0.45	0.54
Y-1-a	6960	1.74	0.36	0.52
Y-1-b	6810	1.76	0.69	0.49
Y-2-a	7430	1.84	0.24	0.51
Y-2-b	7510	1.87	0.22	0.54
Y-3-a	7520	1.93	0.50	0.55
Avg.	7250	1.82	0.40	0.52
Z-8-a	10190	2.26	0.22	0.68
Z-9-a	9440	2.17	0.23	0.70
Z-9-b	8970	2.09	0.30	0.76
Z-10-a	9310	2.22	0.11	0.64
Z-10-b	9850	2.33	0.29	0.63
Avg.	9550	2.21	0.23	0.68

Table 1: Uniaxial Test Results [2]

SPECIMEN	σ_3 psi	FAILURE STRESS-psi	YOUNG'S MODULUS x 10^6 psi	POISSON'S RATIO	FAILURE STRAIN, %
Z-7-a	2000	23890	2.69	0.27	1.35
Z-7-b	2000	23190	2.73	0.24	1.30
Z-8-b	2000	23210	2.54	0.28	1.28
Avg.		23430	2.65	0.26	1.31
Z-1-b	4000	32390	3.37	0.21	1.54
Z-5-b	4000	31350	3.06	0.21	1.63
Z-6-a	4000	32430	3.04	0.23	1.53
Avg.		32060	3.16	0.22	1.57
Z-1-a	6000	38850	2.71	0.10	1.73
Z-2-b	6000	38990	3.05	0.21	1.92
Z-3-b	6000	38130	2.92	0.22	1.77
Avg.		38660	2.89	0.18	1.81
Z-3-a	7500	43140	2.74	0.10	1.96
Z-4-a	7500	42920	3.17	0.20	1.91
Z-4-b	7500	43540	3.08	0.21	1.97
Avg.		43200	2.99	0.17	1.95

Table 2: Triaxial Test Results [2]

SPECIMEN	DIAM. inch	LENGTH inch	FAILURE LOAD-lbs.		FAILURE STRESS-psi
X-1-b	2.140	1.062	1440		403
X-1-c	2.141	1.017	1185		346
X-1-d	2.140	.963	1265		391
X-2-b	2.140	1.052	1235		349
X-2-c	2.140	1.013	1140		335
X-2-d	2.139	1.056	1232.5		347
				Avg.	362
Y-1-c	2.140	1.028	1402.5		406
Y-1-d	2.140	.958	1012.5		314
Y-2-c	2.140	1.018	1165		340
Y-2-d	2.140	.995	1135		339
Y-3-c	2.141	1.038	1265		362
Y-3-d	2.141	1.026	1560		452
				Avg.	369
Z-1-c	2.143	1.033	1422.5		409
Z-1-d	2.143	1.021	1467.5		427
Z-2-c	2.141	1.022	1315		383
Z-2-d	2.141	1.007	1747.5		516
Z-3-c	2.142	.996	1172.5		350
Z-3-d	2.142	1.025	1397.5		405
				Avg.	415

Table 3: Tensile Test Results [2]

PROPERTY	BEREA SANDSTONE	TENNESSEE MARBLE
YOUNG'S MODULUS (psi)	2.5×10^6	9.0×10^6
POISSON'S RATIO	0.20	0.316
TENSILE STRENGTH (psi)	850.	2000.
UNCONFINED COMPRESSIVE STRENGTH (psi)	9500.	17,000.
INTERNAL COEFFICIENT OF FRICTION	1.	1.
DENSITY (lb sec^2/in^4)	.000187	.000253

Table 4: Material Properties Used in Calculations

CASE	ROCK/CUTTER INTERFACE	VERTICAL DISPLACE. (in)	HORIZ. DISPL. (in)	ROCK TYPE	CONSTITUTIVE MODEL	LOCAL SOFTENING UNDER CUTTER	CUTTER BOTTOM TILT	CONFINING PRESSURE (psi)
1	Flat Rock	0.001	0.003	Berea Sandstone	Tensile/Coulomb	No	0.0	0.0
2	Flat Rock	0.002	0.002	"	"	No	0.0	0.0
3	0.100 inch Kerf	0.0	0.003	"	"	No	0.0	0.0
4	"	0.0	0.003	"	Tensile/Plasticity	No	0.0	0.0
5	"	0.0	0.003	"	Tensile/Coulomb	Yes	0.0	0.0
6	"	0.001	0.002	"	"	Yes	0.0	0.0
7	"	0.001	0.002	"	"	Yes	0.001	0.0
8	"	0.001	0.002	"	Tensile/Plasticity	Yes	0.001	0.0
9	"	0.001	0.0015	Tennessee Marble	Tensile/Coulomb	Yes	0.001	0.0
10	0.050 inch Kerf	0.001	0.003	Berea Sandstone	"	Yes	0.001	0.0
11	0.100 inch Kerf	0.001	0.003	"	"	Yes	0.001	3000

Table 5: Cases Examined in Drag Bit Calculations

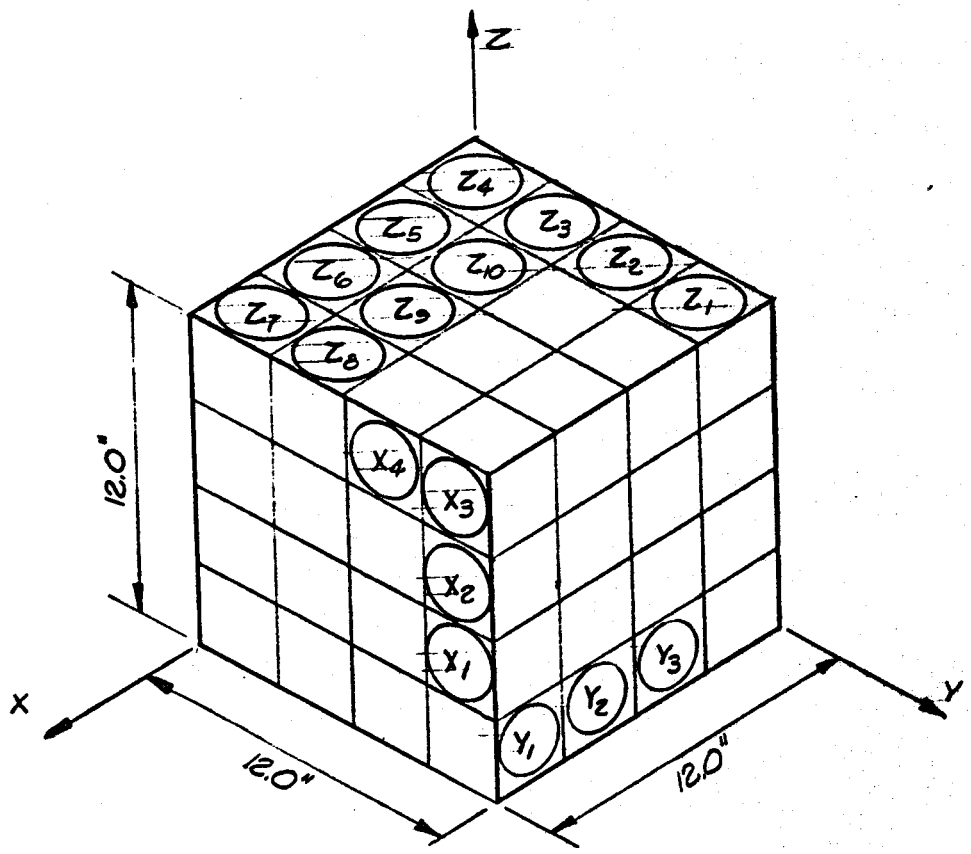

Coring Sequence:

Z_1, Z_2, Z_3, Z_4

Y_1, Y_2, Y_3

X_1, X_2, X_3, X_4

Z_5, Z_6, Z_7, Z_8, Z_9, Z_{10}

Figure 1: Rock Coring Plan [2]

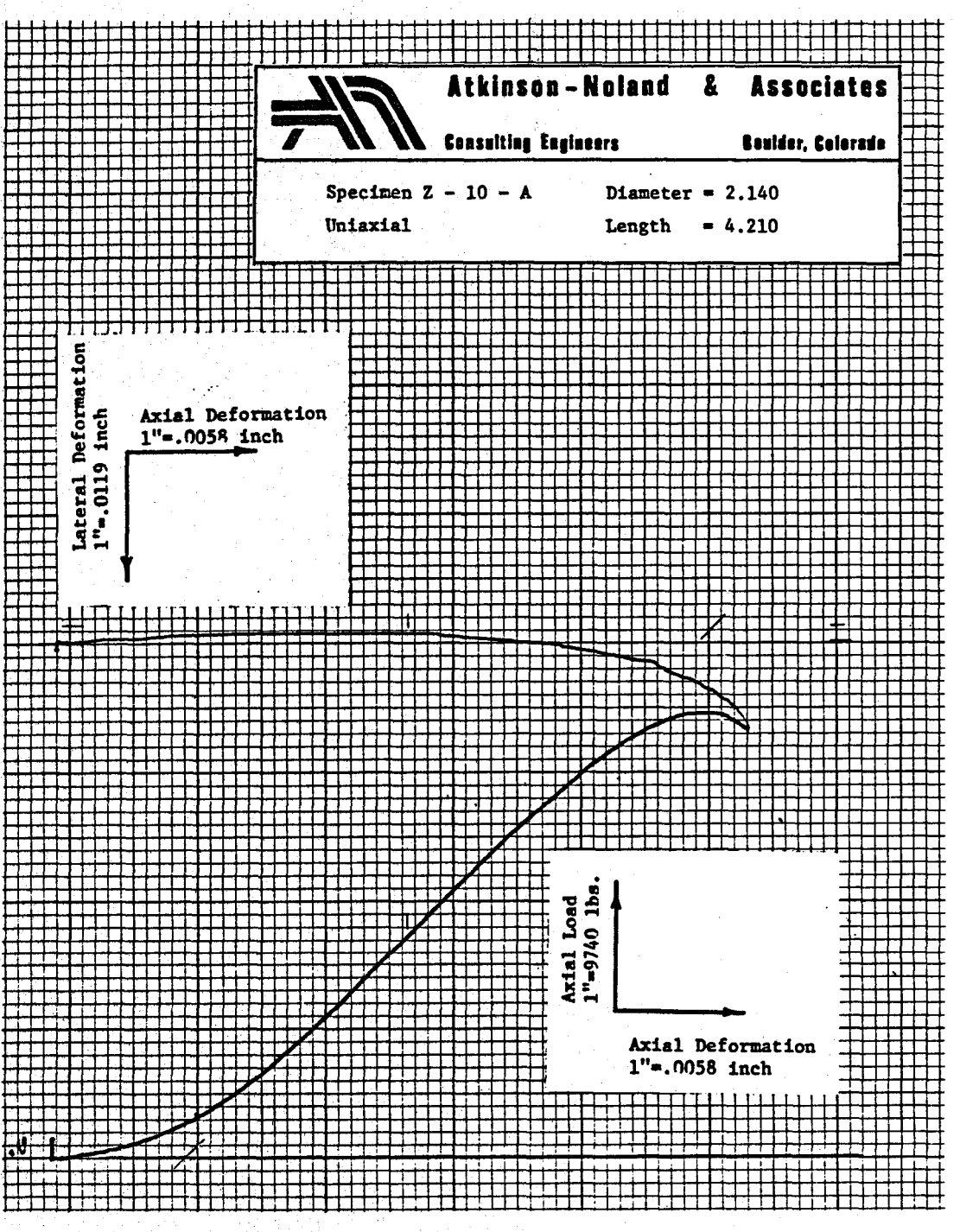

Figure 2: Typical Unconfined Load-Deformation Response [2]

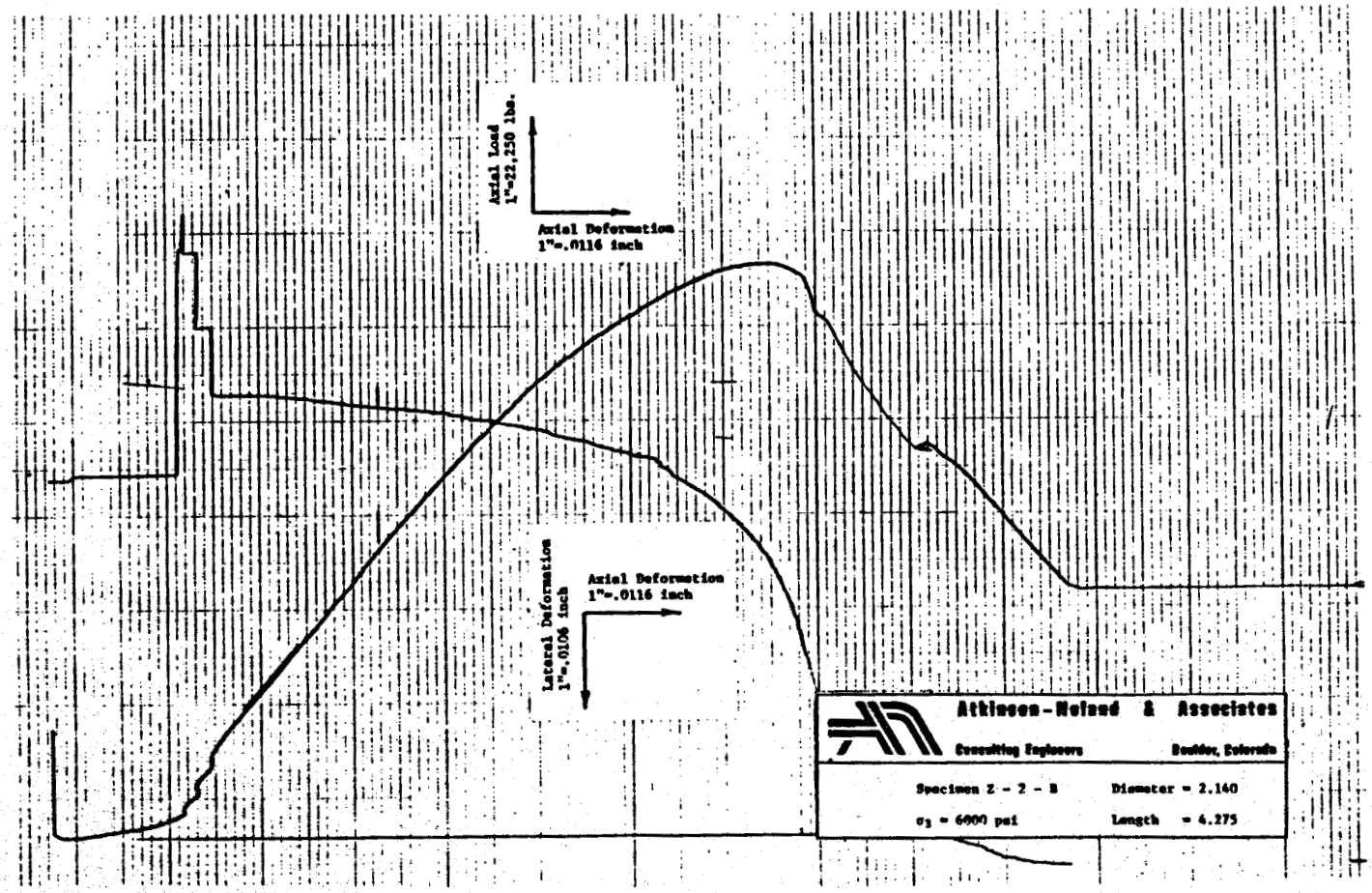

Figure 3: Typical Confined Load-Deformation Response [2]

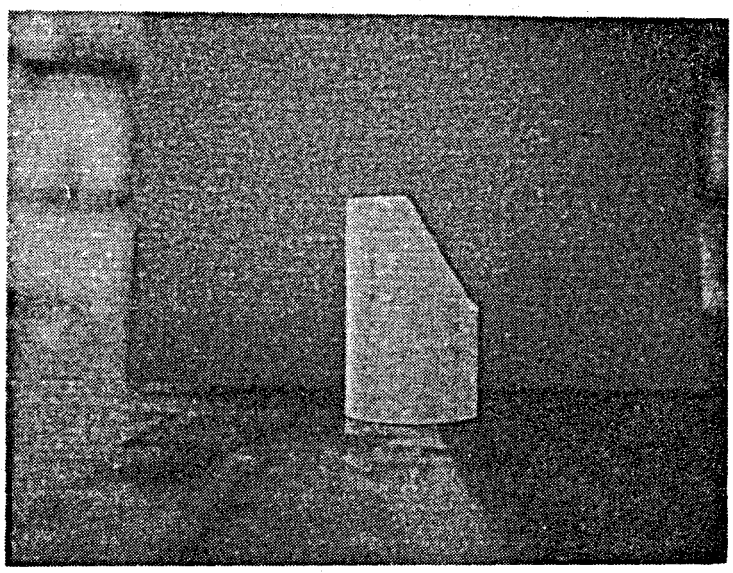

a. Z-3-a
σ_3 = 7500 psi

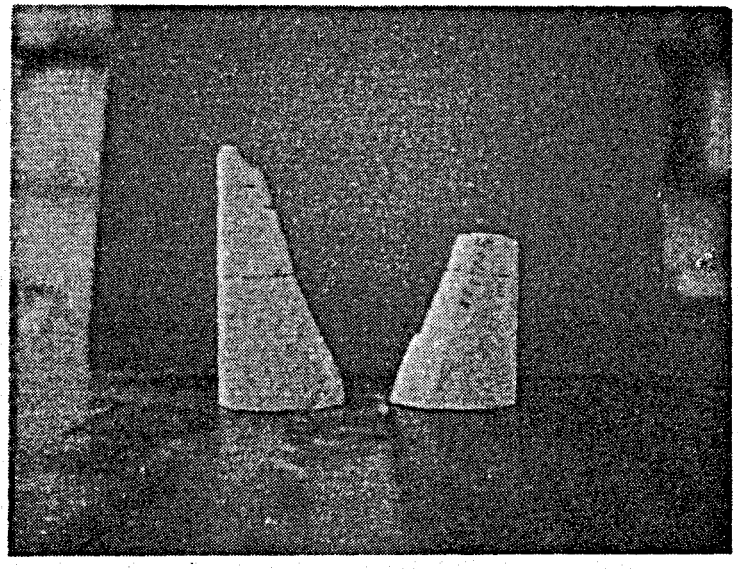

b. Z-7-a
σ_3 = 2000 psi

Figure 4: Photographs of Typical Failed Specimens [2]

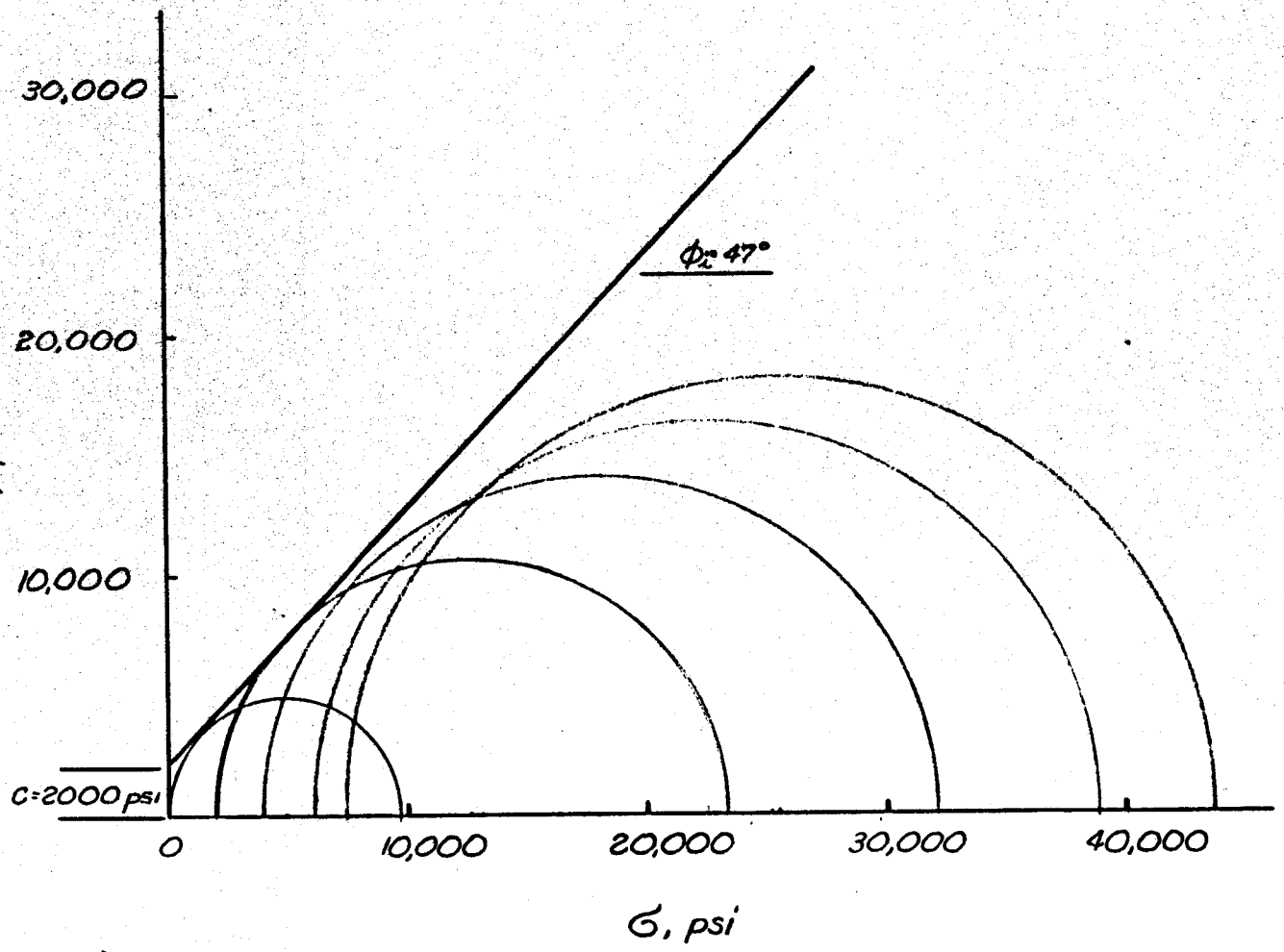

Figure 5: Mohr Circles of Average Failure Data [2]

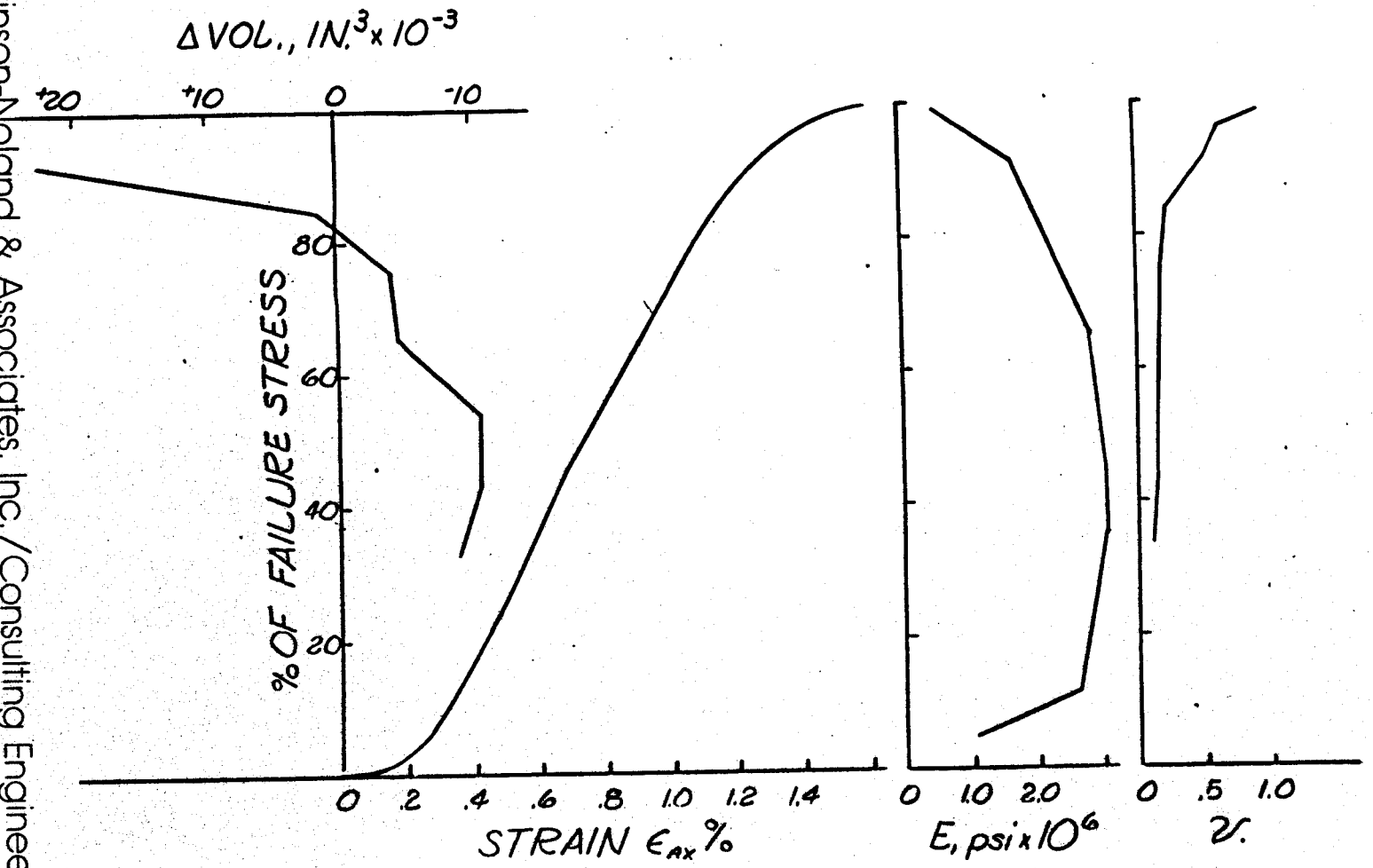

Figure 6: Property Variation as a Function of Stress
Specimen Z-5-b, σ_3 = 4,000 psi

a. Maximum Stress in R-Z Plane (R-Z Crack)

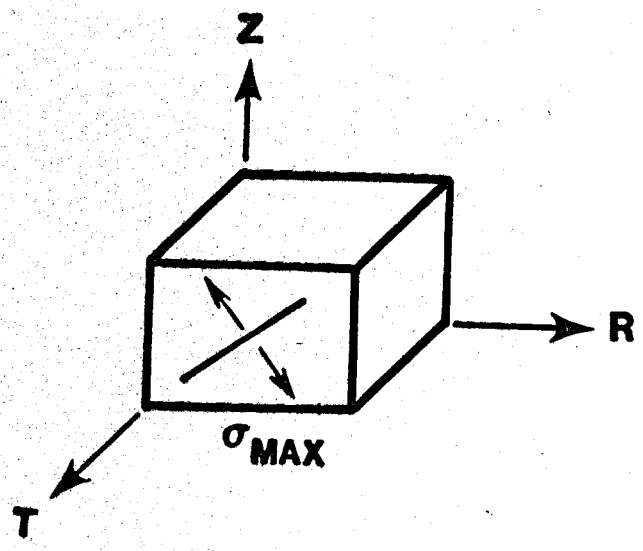

b. Maximum Stress in Hoop Plane (Hoop Crack)

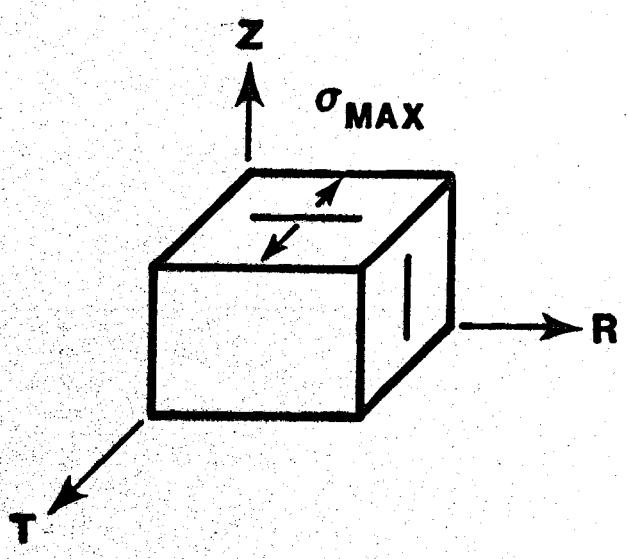

Figure 7: Tensile Crack Orientations in Axisymmetric Coordinates

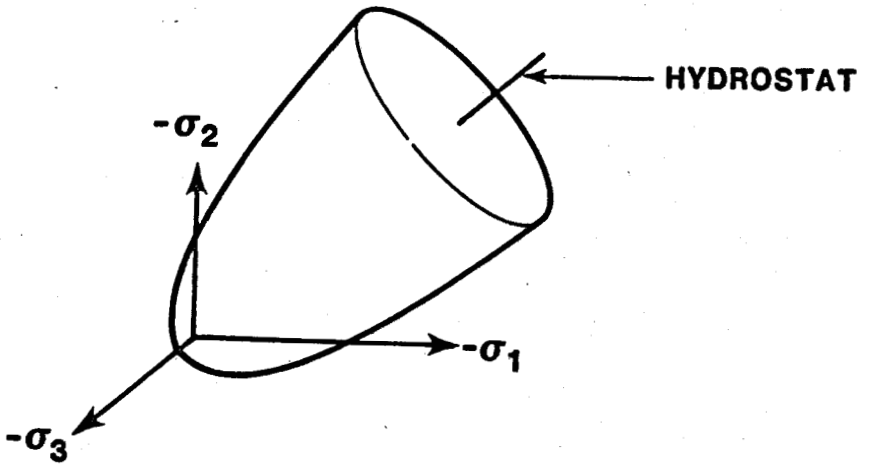

Figure 8: Plasticity Yield Surface in Principal Stress Space

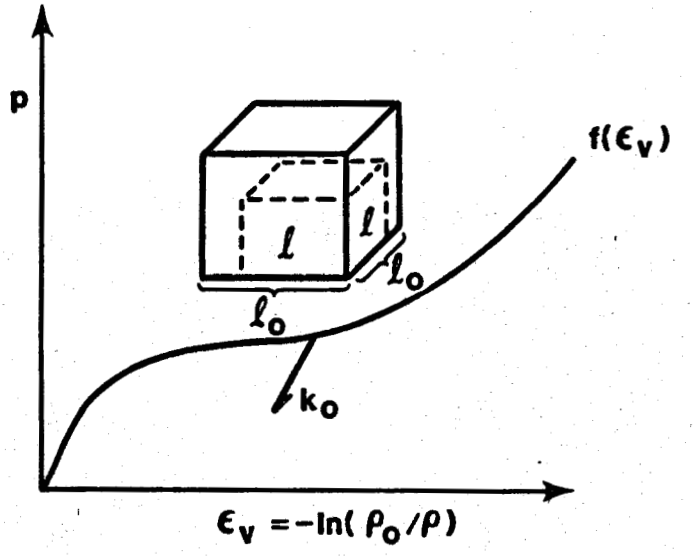

Figure 9: The Pressure vs Finite Volume Strain Behavior of the Plasticity Model

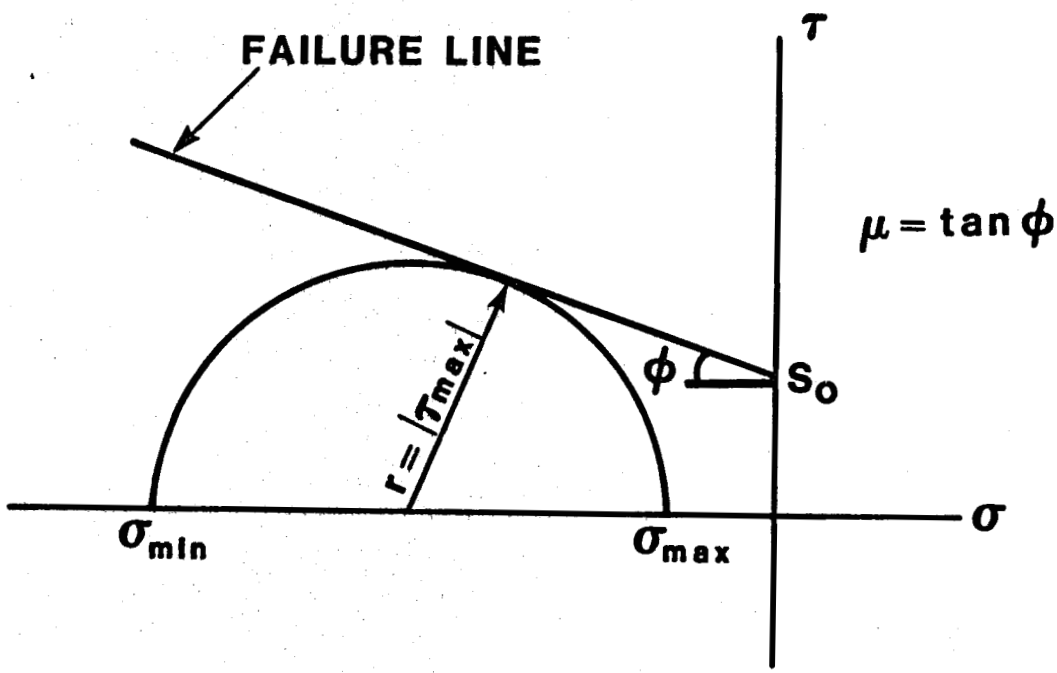

Figure 10: Mohr Circle Representation of Coulomb Failure Criterion

(a) Minimum and Maximum Stress in R-Z Plane (R-Z Crack)

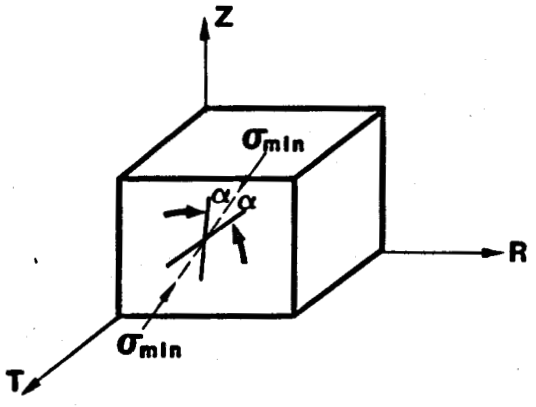

(b) Minimum Stress in R-Z Plane and Maximum in Hoop Plane (Hoop Crack)

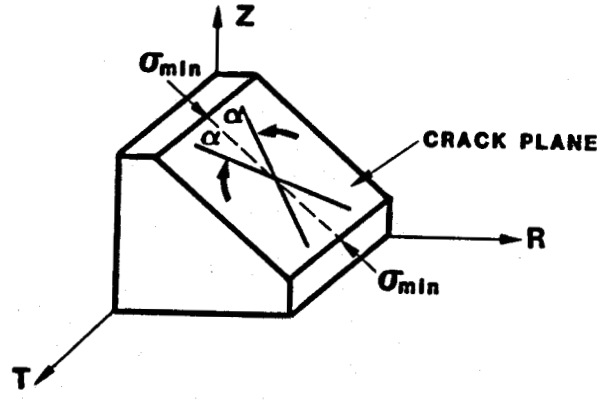

(c) Minimum Stress in Hoop Plane and Maximum in R-Z Plane (Hoop Crack)

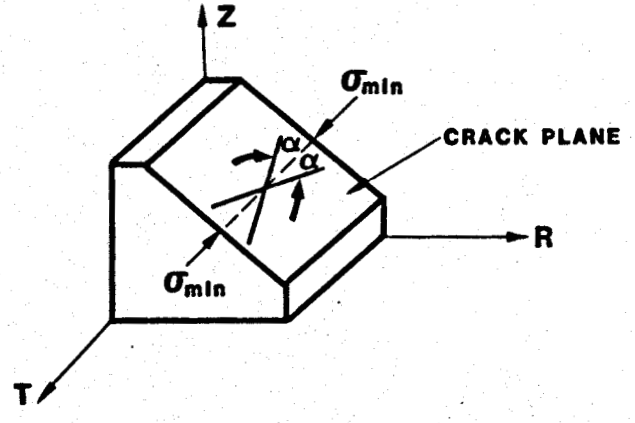

Figure 11: Shear Crack Orientations in Axisymmetric Coordinates

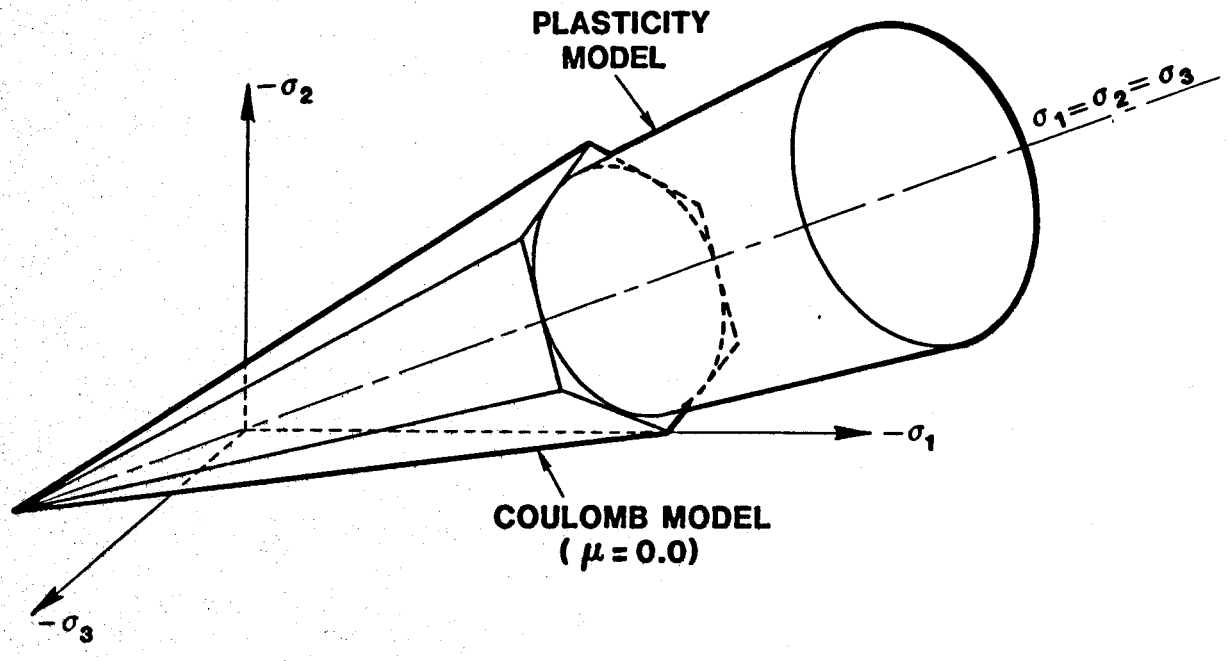

Figure 12: Coulomb and Plasticity Model Yield Surfaces in Principal Stress Space

a. Unconfined Compression Test

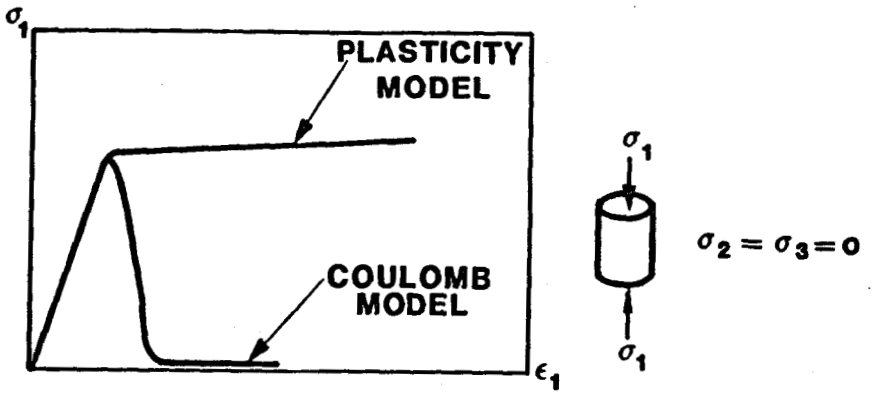

b. Confined Compression Test

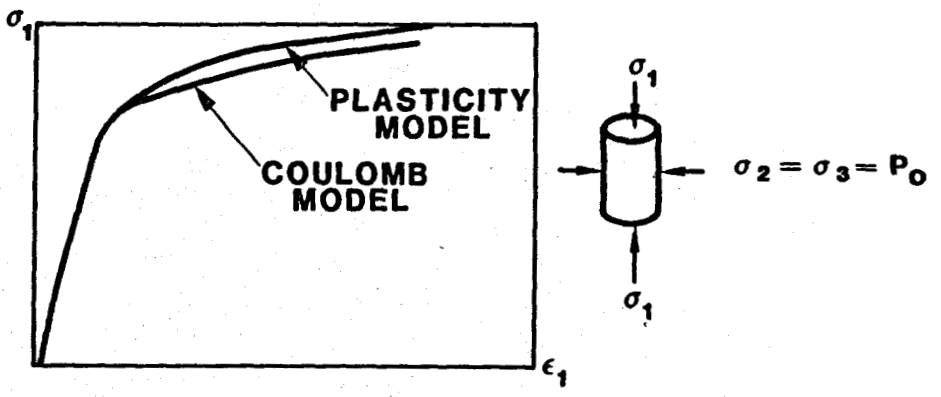

Figure 13: Post-Failure Response of the Two Models

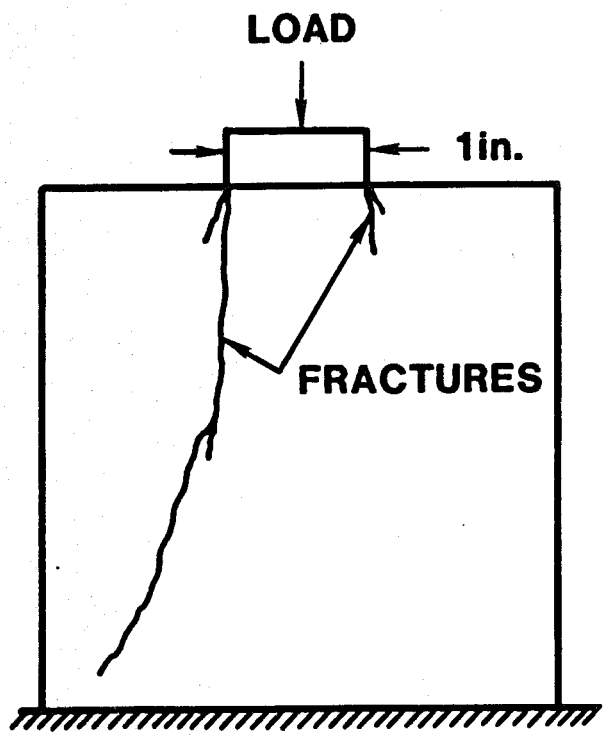

Figure 14: Post-Test Fractures in a Typical Unconfined Indention Specimen

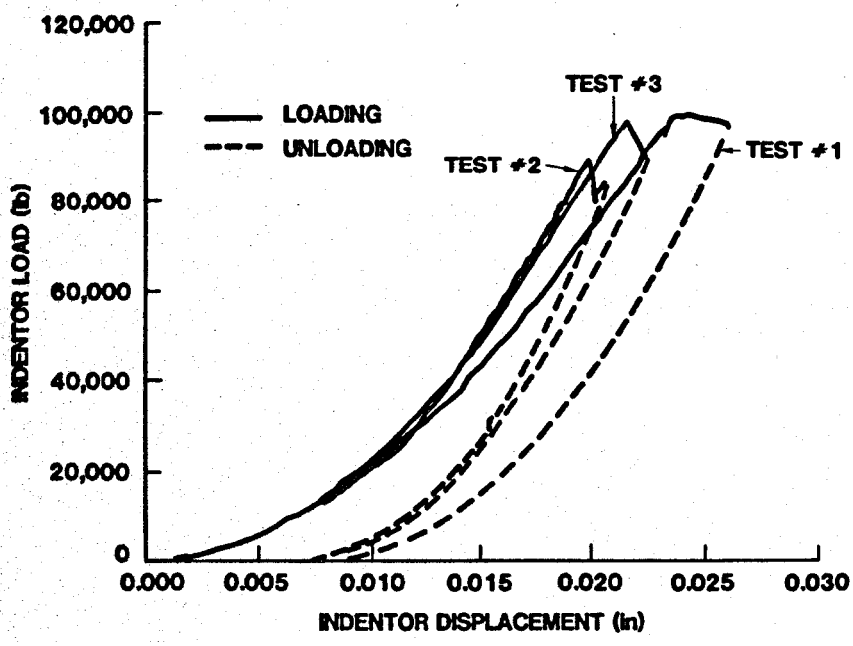

Figure 15: Load/Displacement Response of Unconfined Indention Test

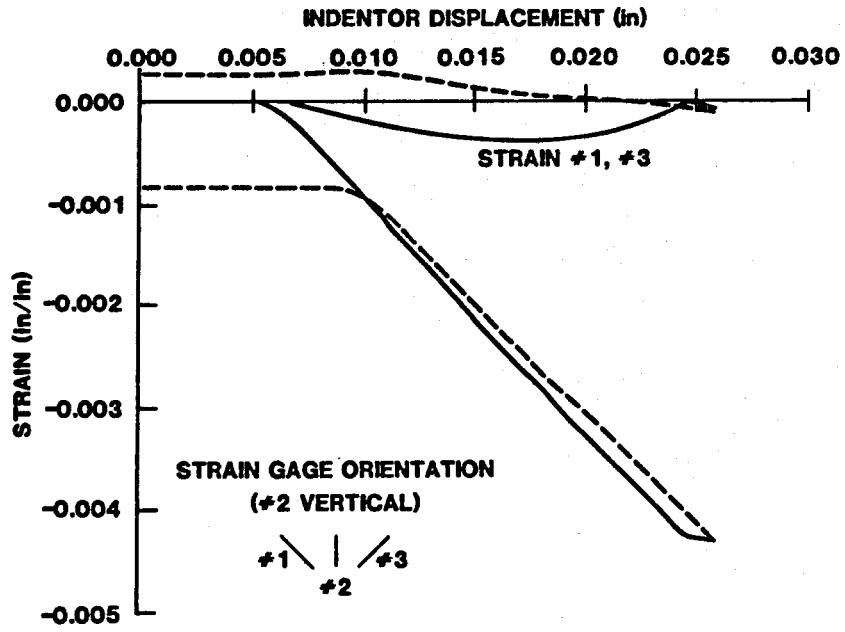

Figure 16: Strain Measurements for Unconfined Indention Test #1

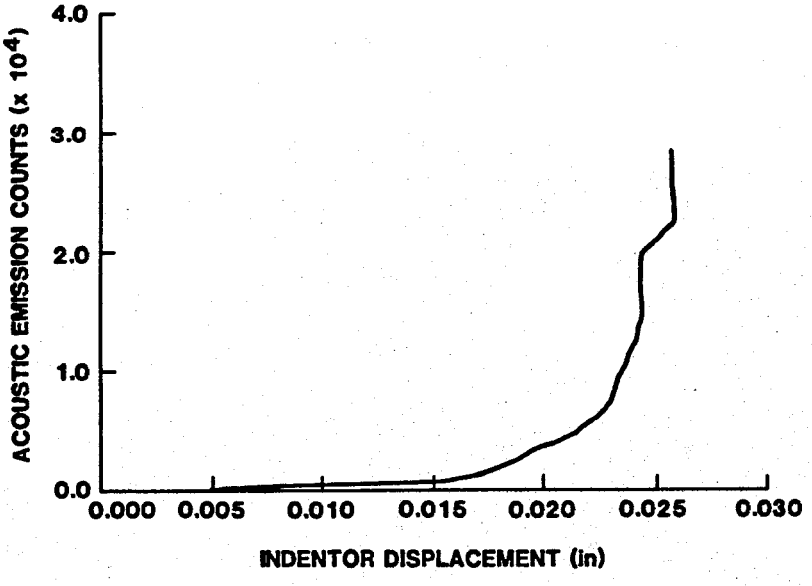

Figure 17: Accoustic Emission Counts for Unconfined Indention Test #1

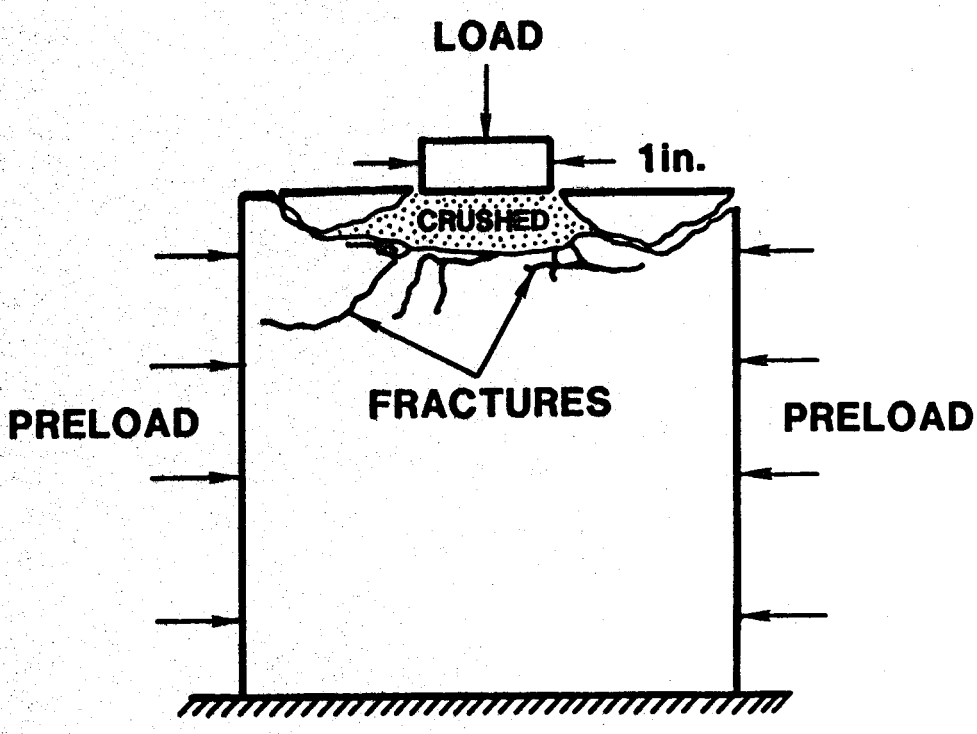

Figure 18: Post-Test Fractures in a Typical Confined Indention Specimen (-2100 psi pre-stress)

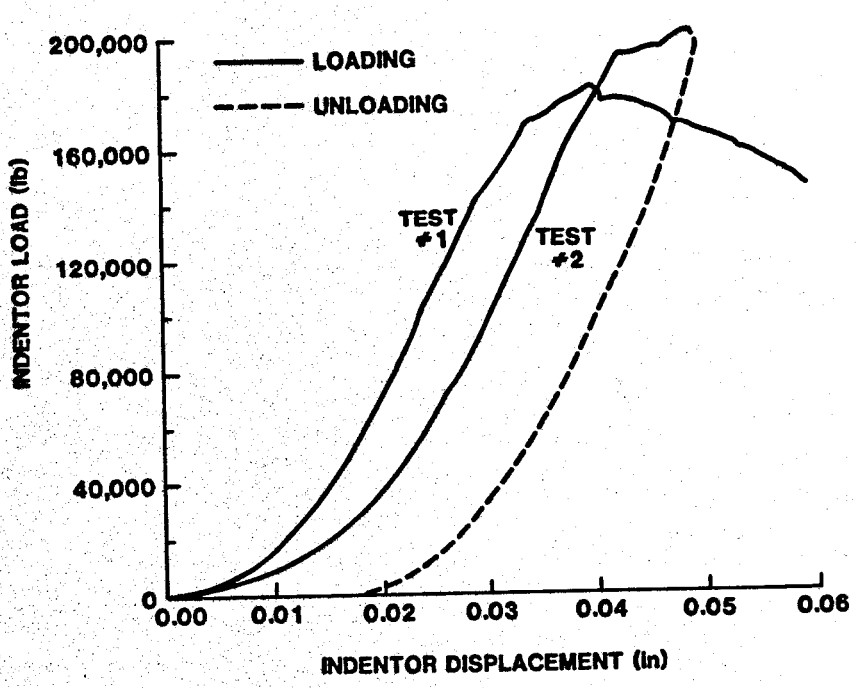

Figure 19: Load/Displacement Response of Confined Indention Tests

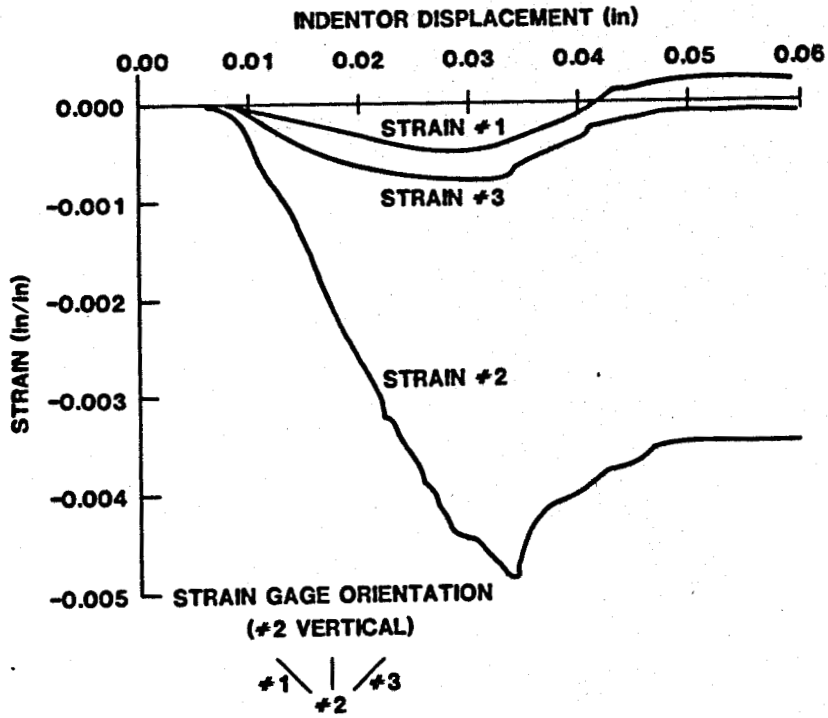

Figure 20: Strain Measurements for Confined Indention Test #1

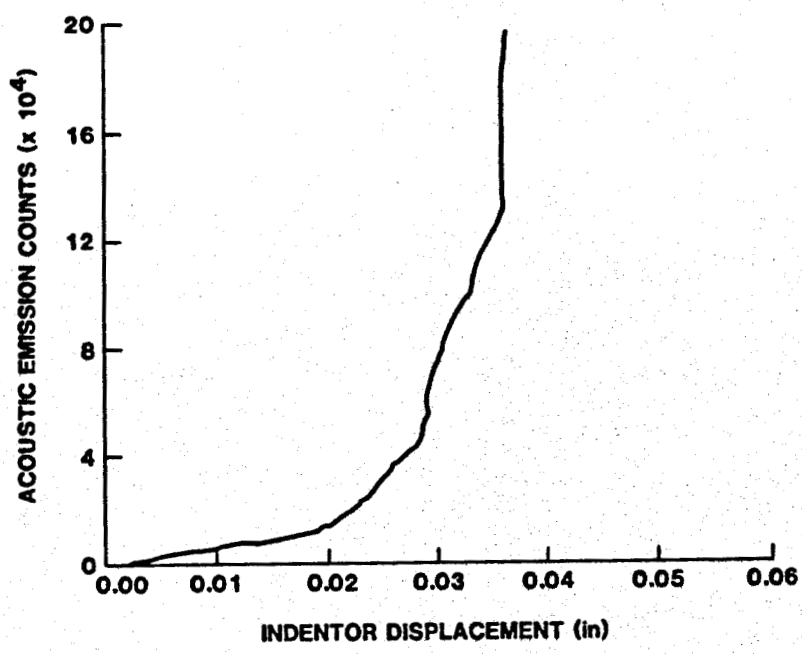

Figure 21: Accoustic Emission Counts for Confined Indention Test #2

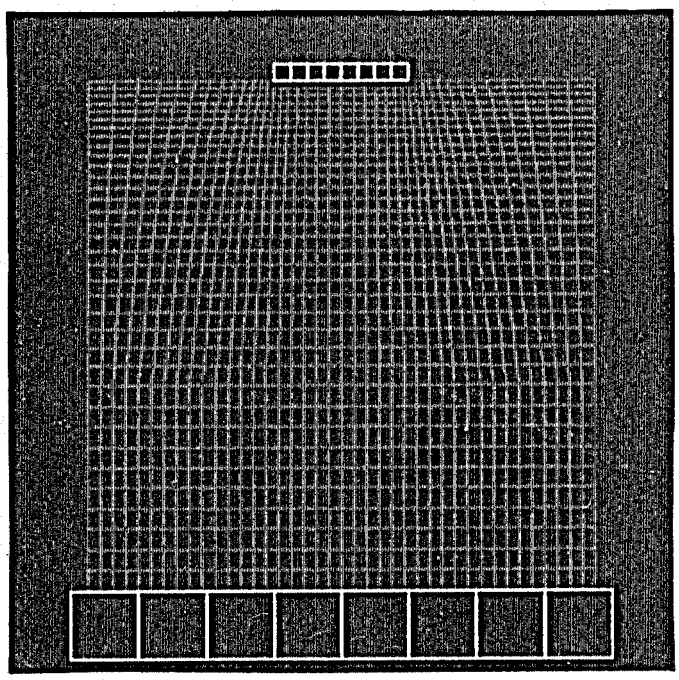

Figure 22: Finite Element Mesh Used for Analysis of Unconfined Indention Tests

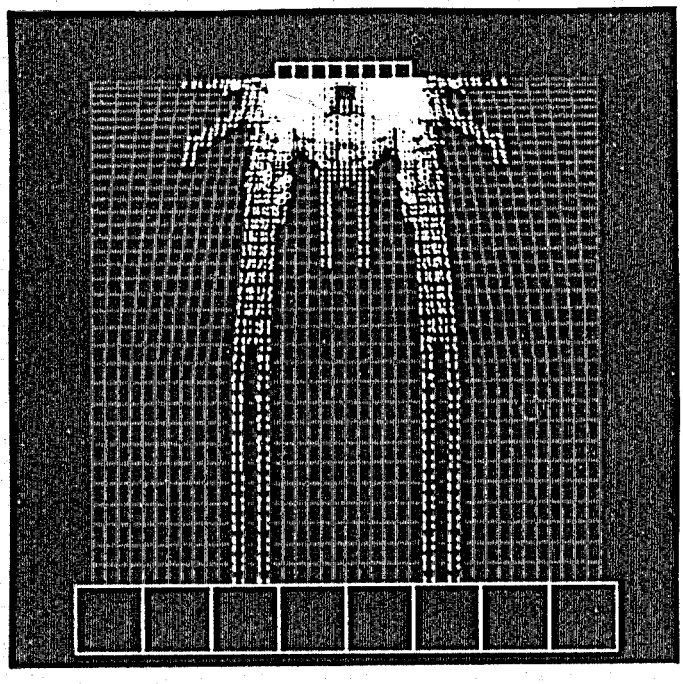

Figure 23: Predicted Fracture Pattern for Unconfined Indention Test, Tensile/Coulomb Model

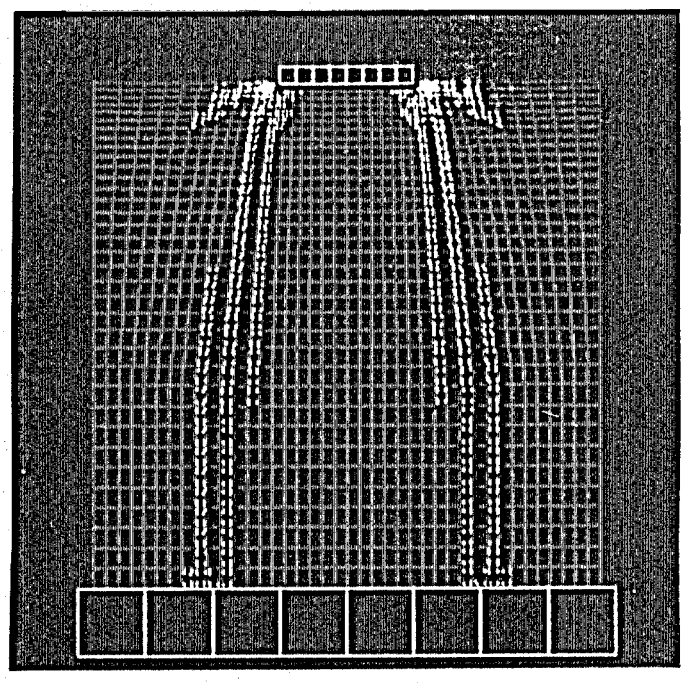

Figure 24: Predicted Fracture Pattern for Unconfined Indention Test, Tensile/Plasticity Model

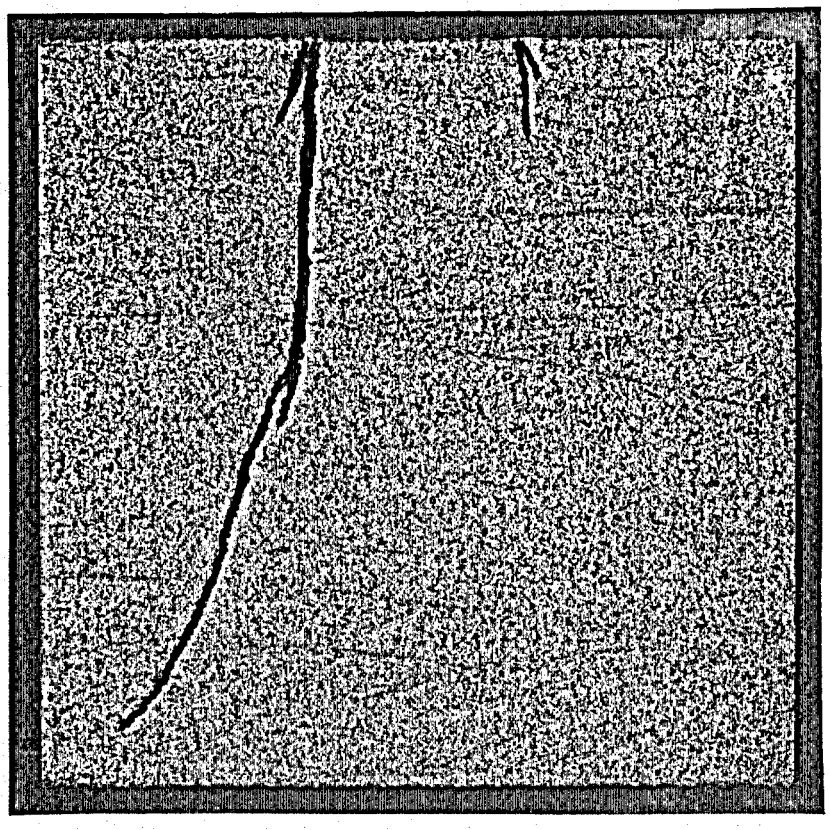

Figure 25: Post-Test Photograph of a Typical Unconfined Indention Specimen

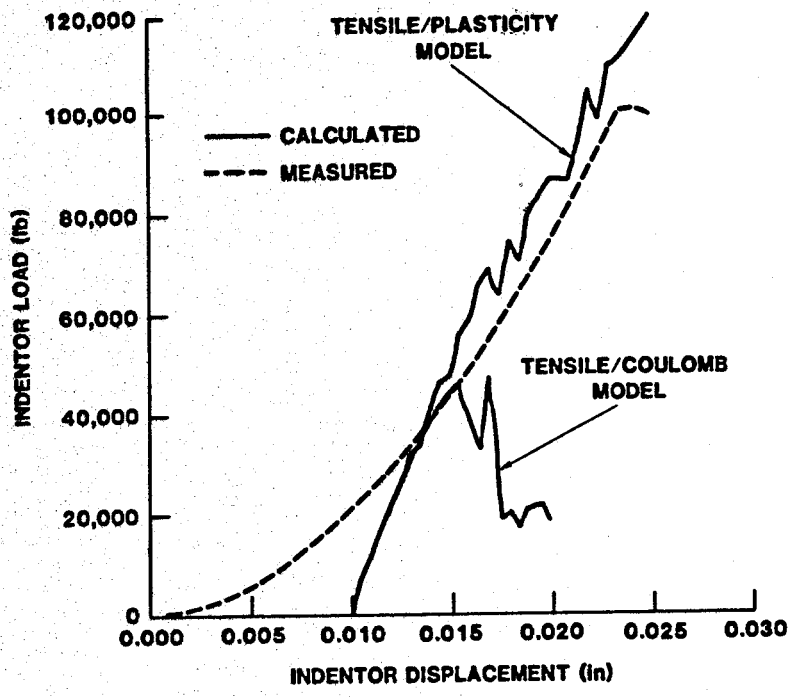

Figure 26: Comparison of Predicted and Measured Indentor Loads for Unconfined Tests (Calculated Loads Shifted 0.010 in)

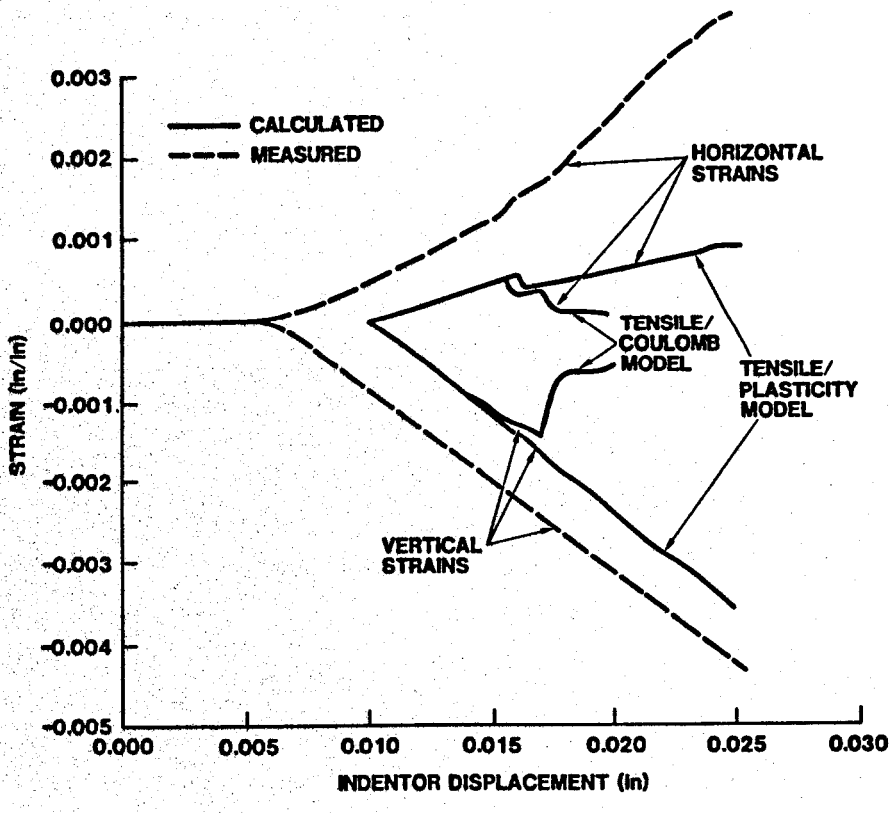

Figure 27: Comparison of Predicted and Measured Strains for Unconfined Tests (Calculated Strains Shifted 0.010 in)

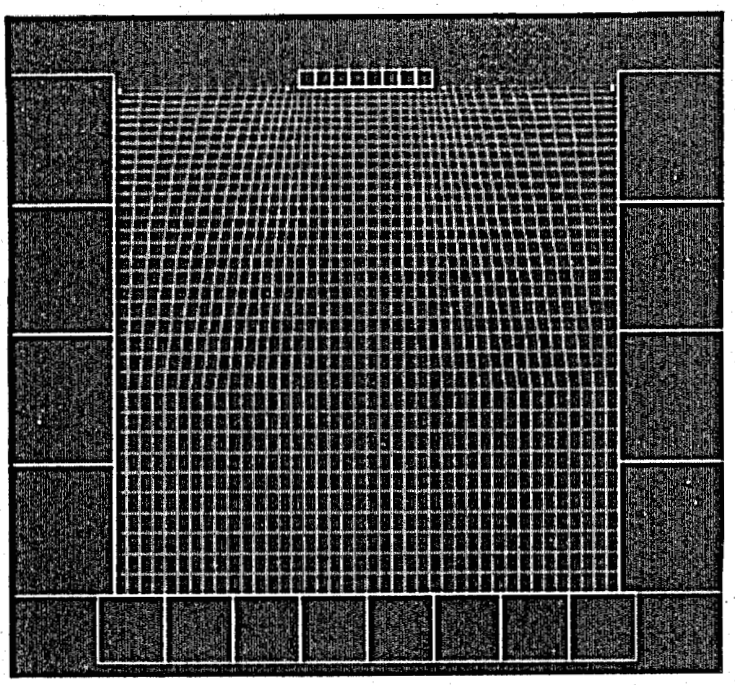

Figure 28: Finite Element Mesh Used for Analysis of Confined Indention Tests

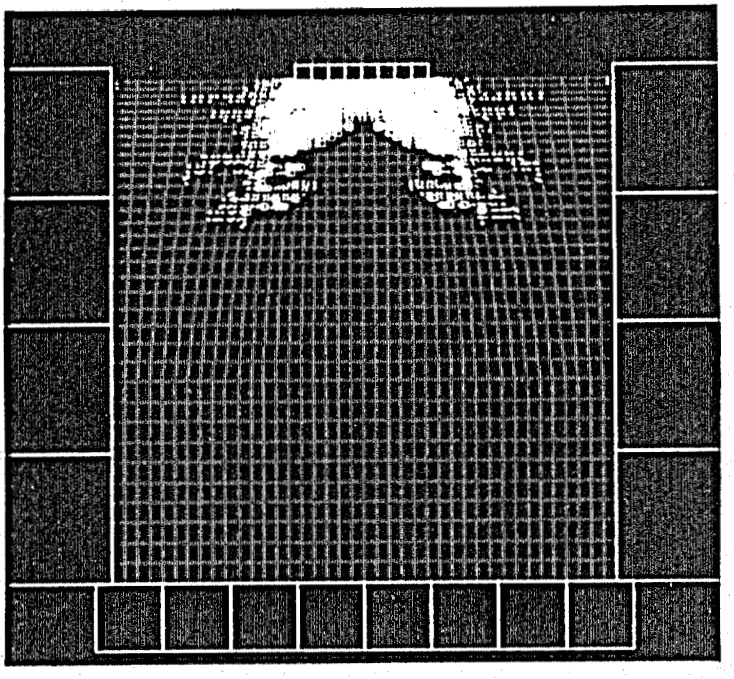

Figure 29: Predicted Fracture Pattern for Confined Indention Test, Tensile/Coulomb Model

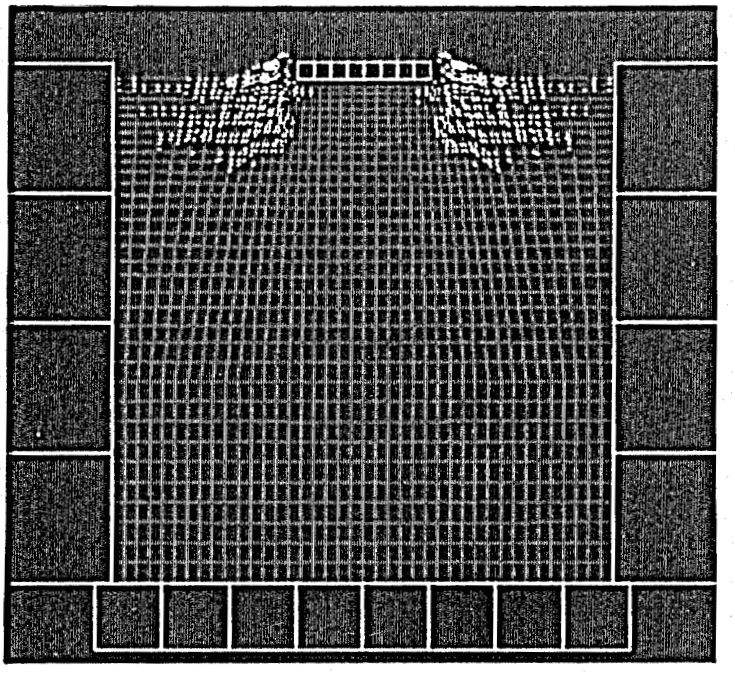

Figure 30: Predicted Fracture Pattern for Confined Indention Test, Tensile/Plasticity Model

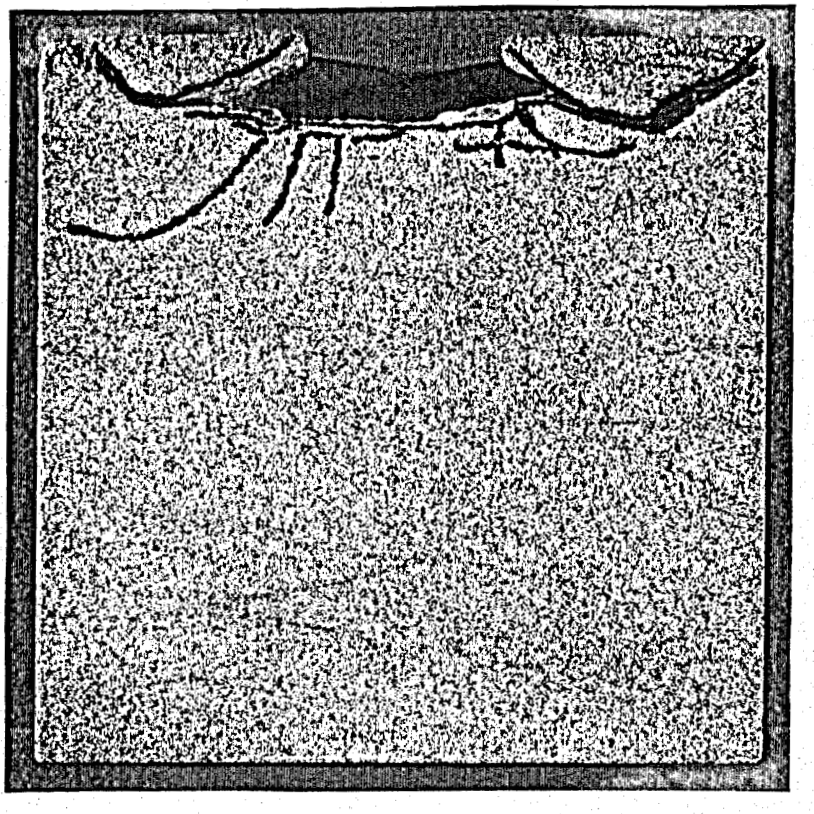

Figure 31: Post-Test Photograph of a Typical Confined Indention Specimen

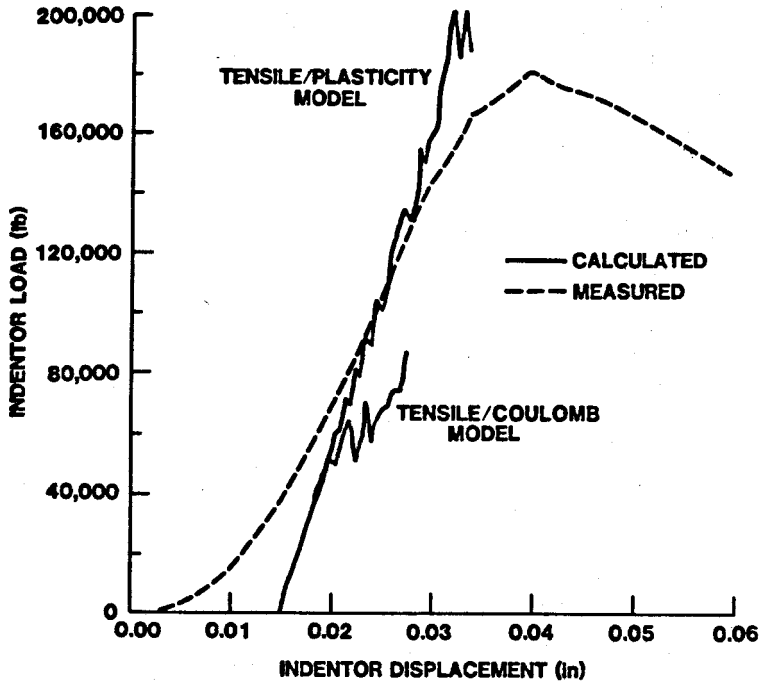

Figure 32: Comparison of Predicted and Measured Indentor Loads for Confined Tests (Calculated Loads Shifted 0.015 in)

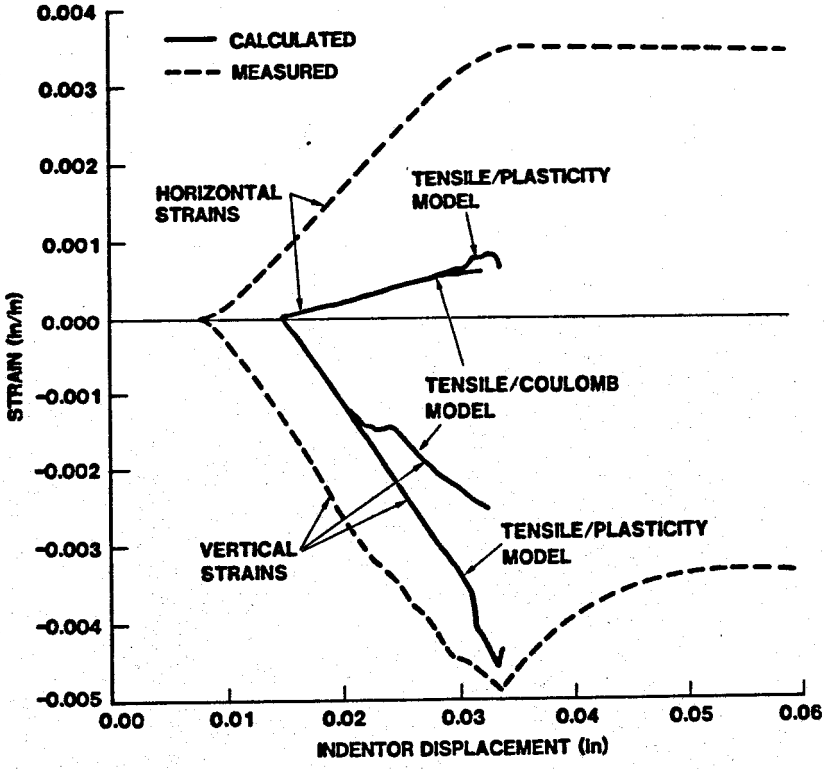

Figure 33: Comparison of Predicted and Measured Strains for Confined Tests (Calculated Strains Shifted 0.015 in)

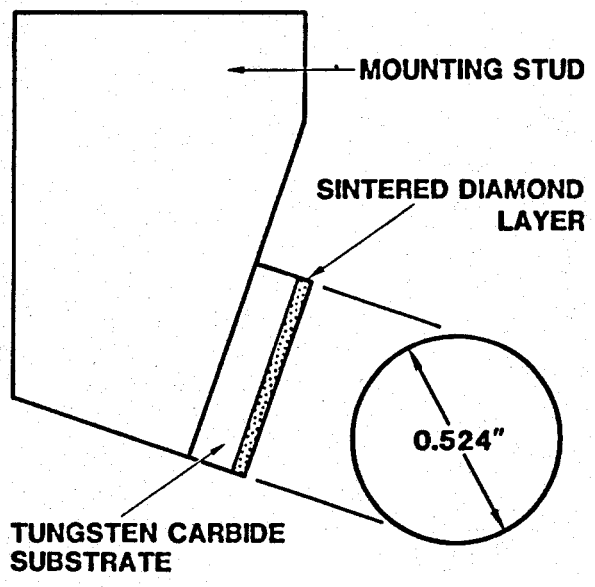

Figure 34: Polycrystalline Diamond Cutter

Figure 35: Drill Bits Made Using Polycrystalline Diamond Cutters

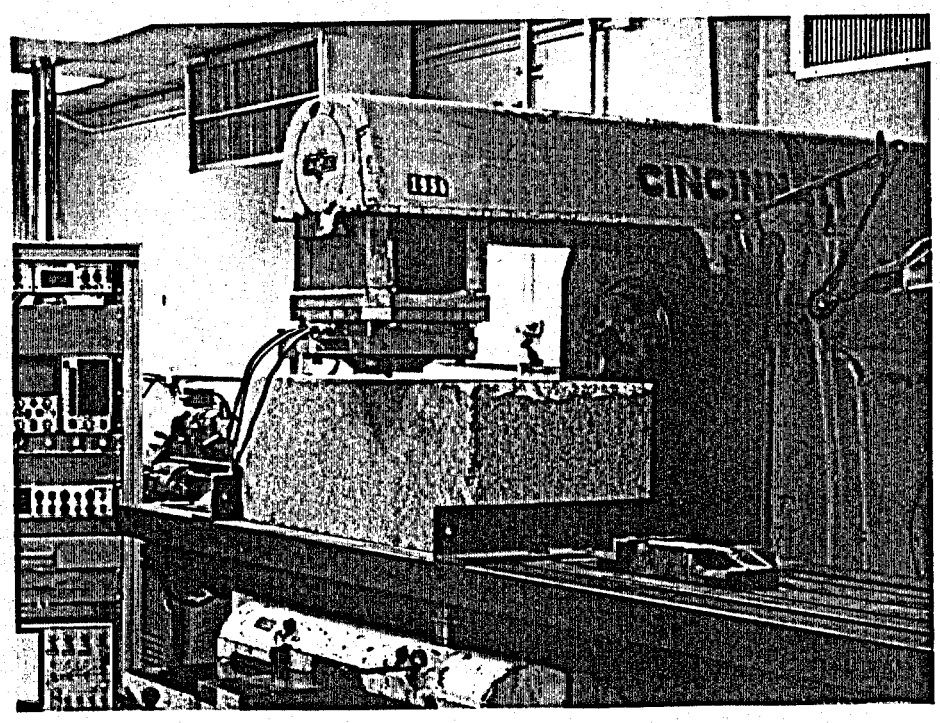

Figure 36: Milling Machine Used for Single Cutter Tests

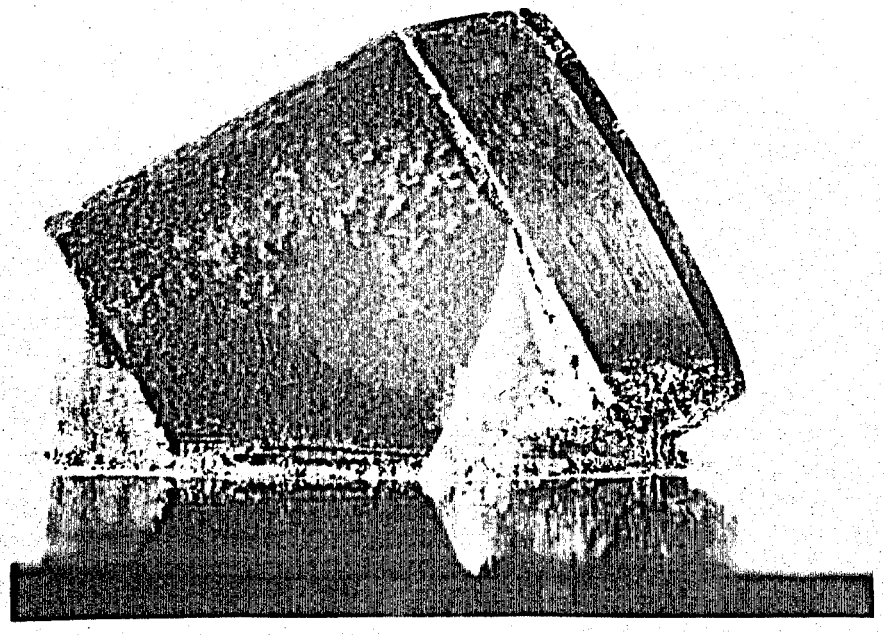

Figure 37: Photograph of Single Cutter Used in Tests

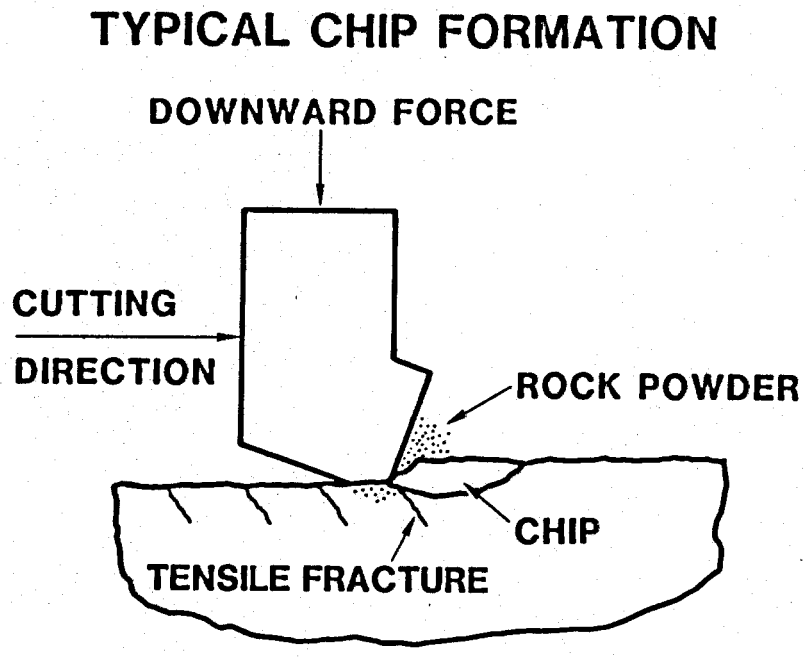

Figure 38: Observed Fracture Process

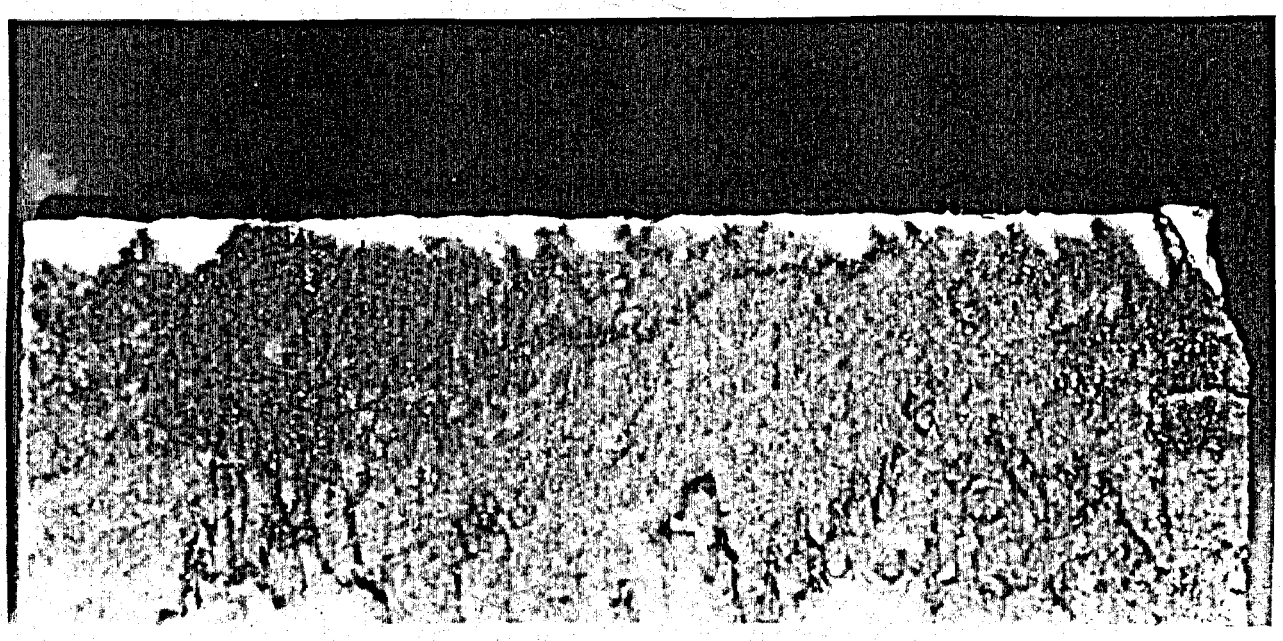

Figure 39: Photograph of Sectioned Tennessee Marble Specimen Impregnated with Fluorescent Dye (Specimen length is 3.85 in)

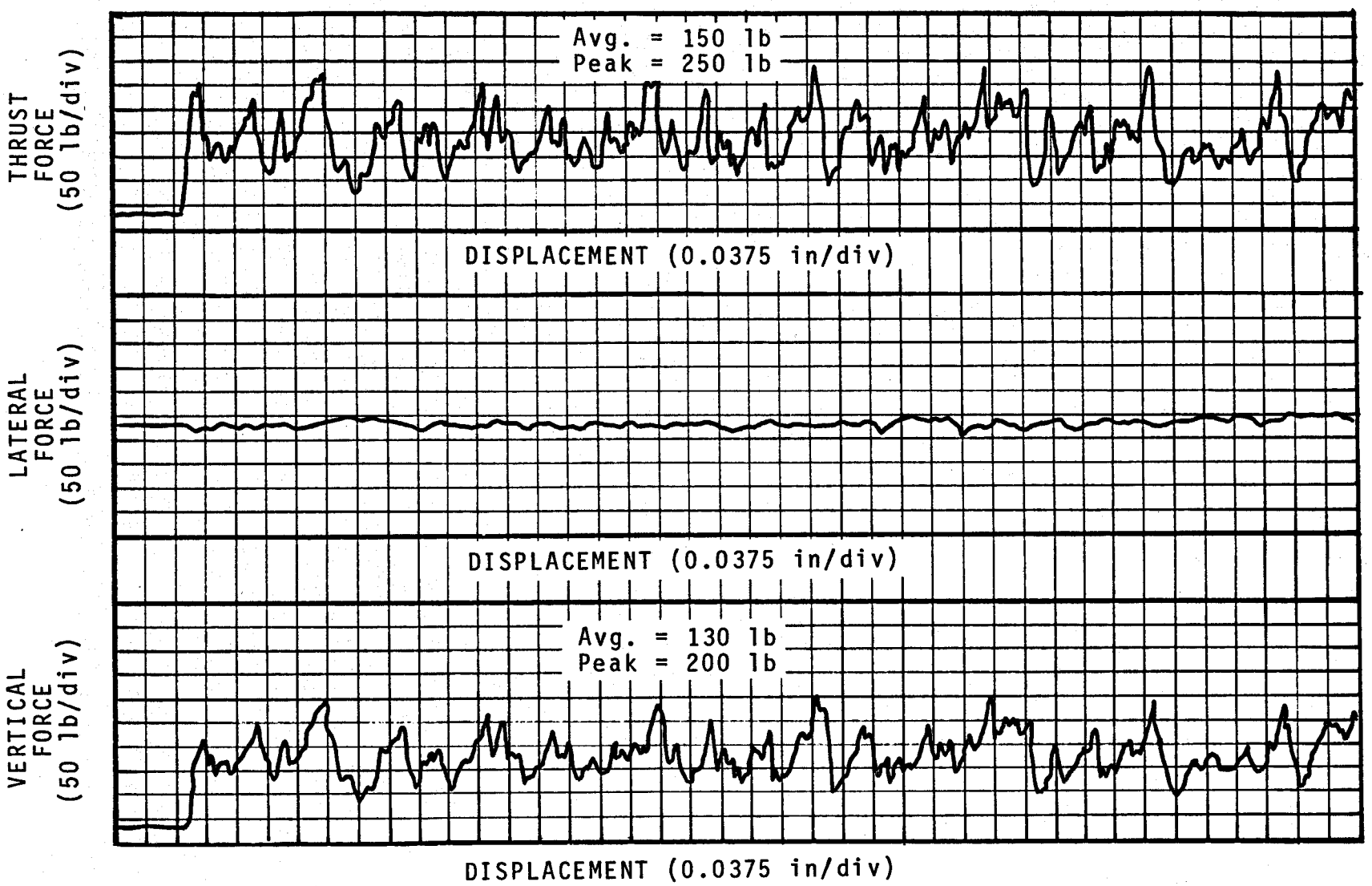

Figure 40: Cutting Forces for Berea Sandstone
0.050 inch Cutting Depth

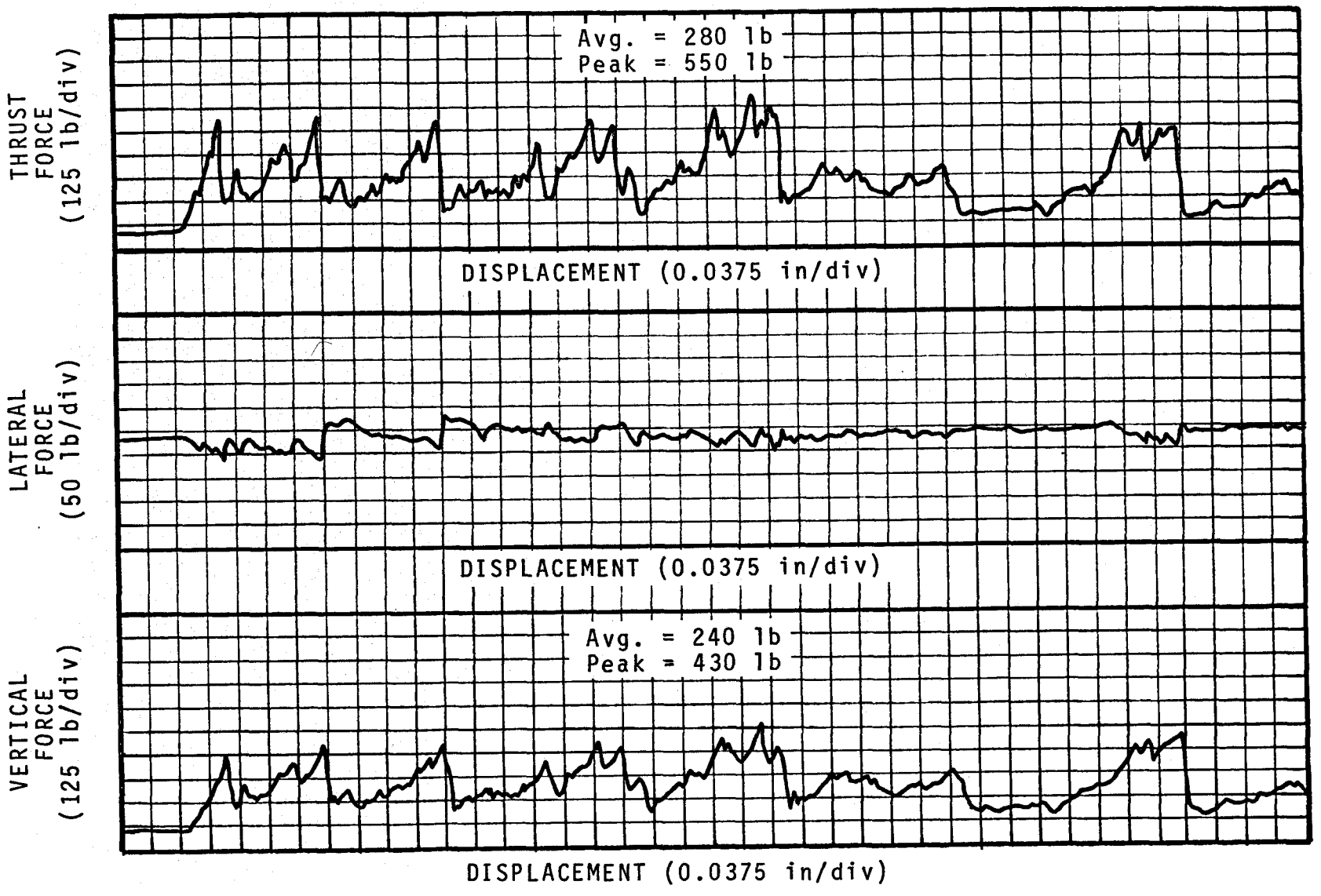

Figure 41: Cutting Forces for Berea Sandstone
0.100 inch Cutting Depth

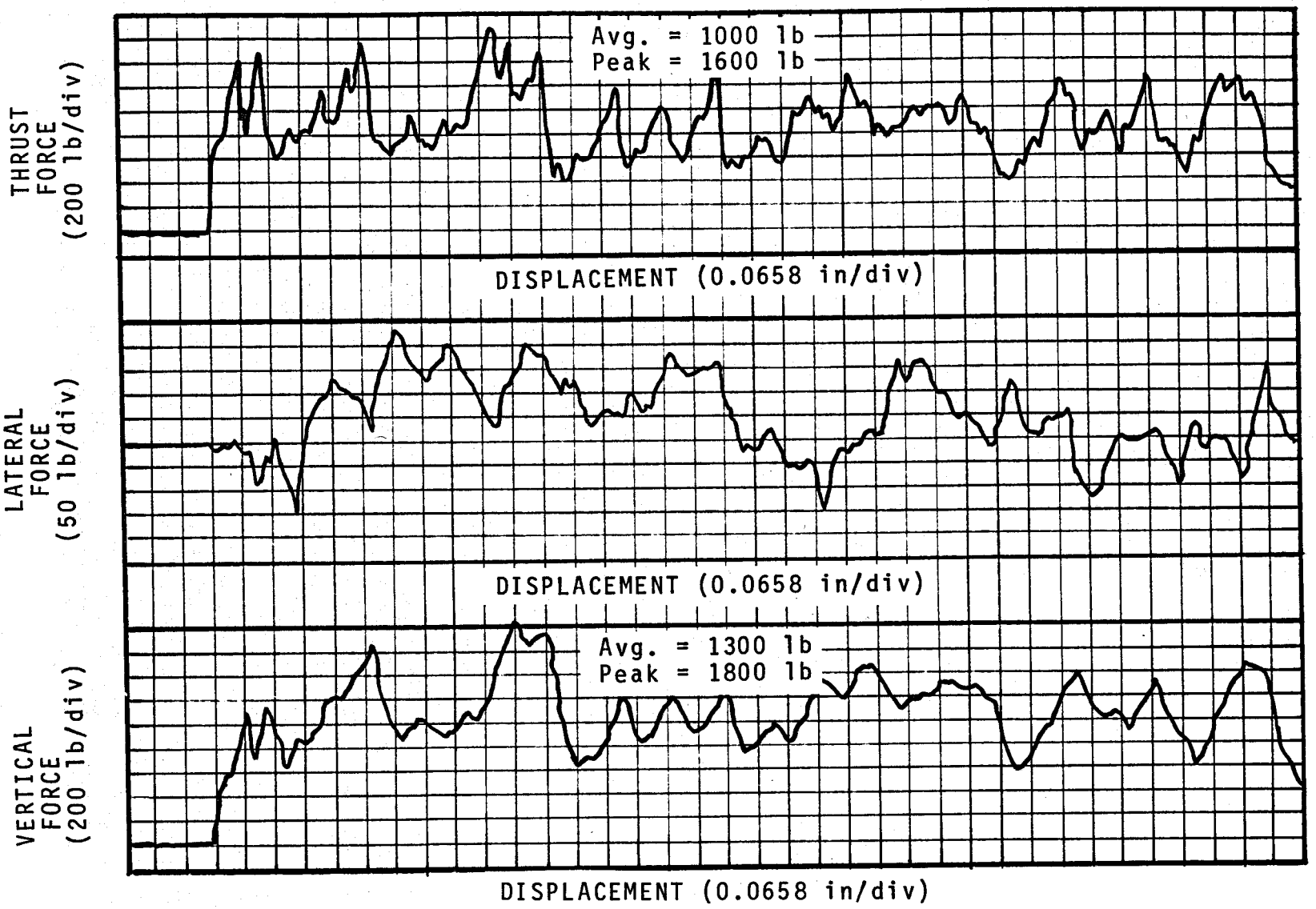

Figure 42: Cutting Forces for Tennesses Marble
0.100 inch Cutting Depth

a. Entire Mesh

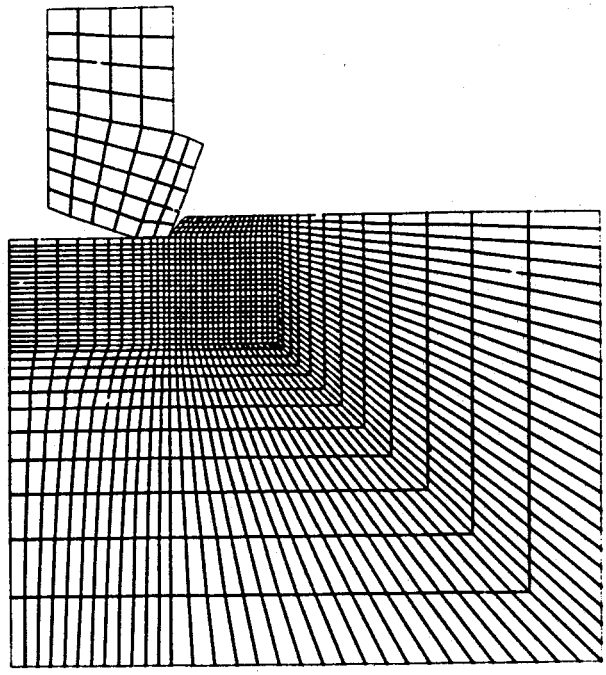

b. Detail of Rock/Cutter Interface
(* In some cases, material properties
of these elements were softened)

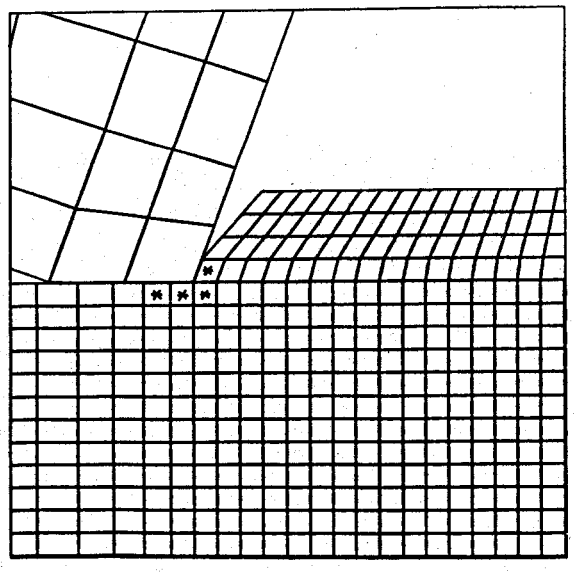

Figure 43: Finite Element Mesh Used for Analysis of Single Cutter

a. Initial Conditions

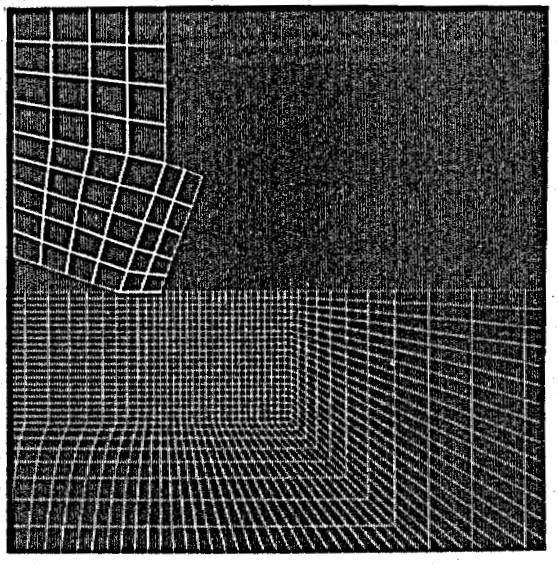

b. After 0.001 inch Vertical Displacement

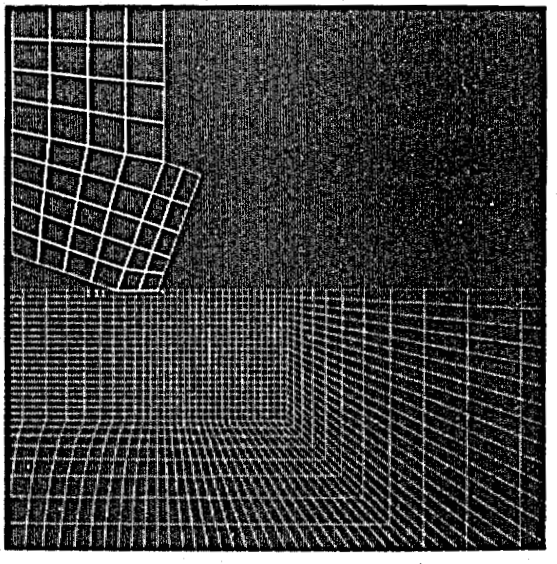

c. After 0.001 inch Horizontal Displacement (Vertical Displacement Held at 0.001 inch)

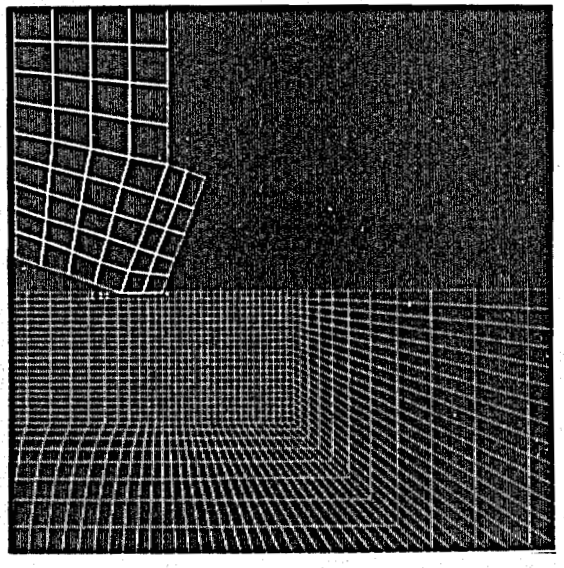

d. After 0.002 inch Horizontal Displacement (Vertical Displacement Held at 0.001 inch)

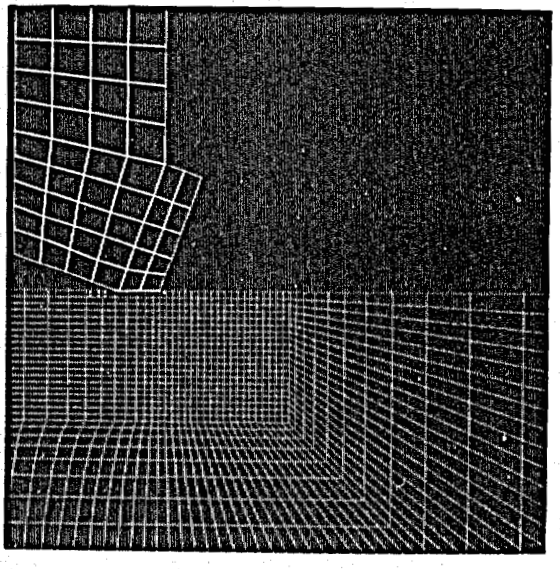

Figure 44: Prediction of Fractures in Berea Sandstone for a Flat Rock Surface (0.001 inch Vertical Displacement) Case #1

a. Initial Conditions

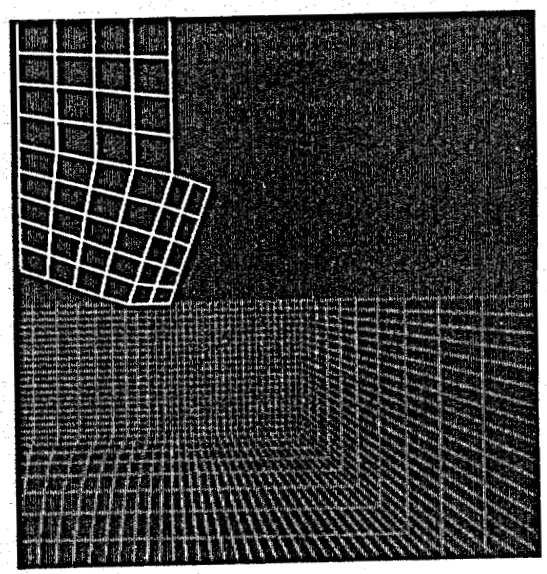

b. After 0.002 inch Vertical Displacement

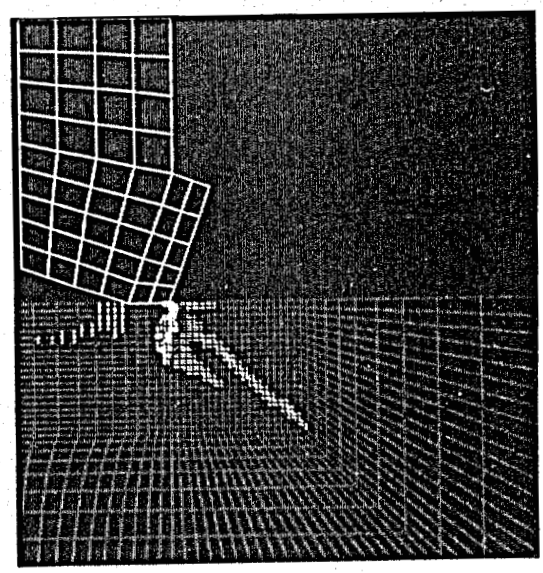

c. After 0.001 inch Horizontal Displacement (Vertical Displacement Held at 0.002 inch)

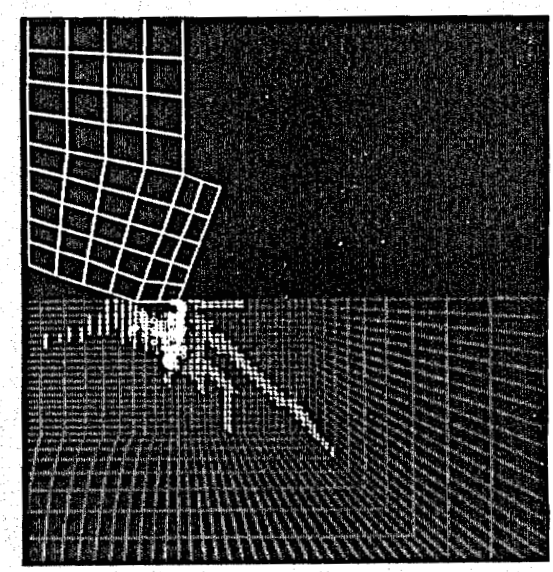

d. After 0.002 inch Horizontal Displacement (Vertical Displacement Held at 0.002 inch)

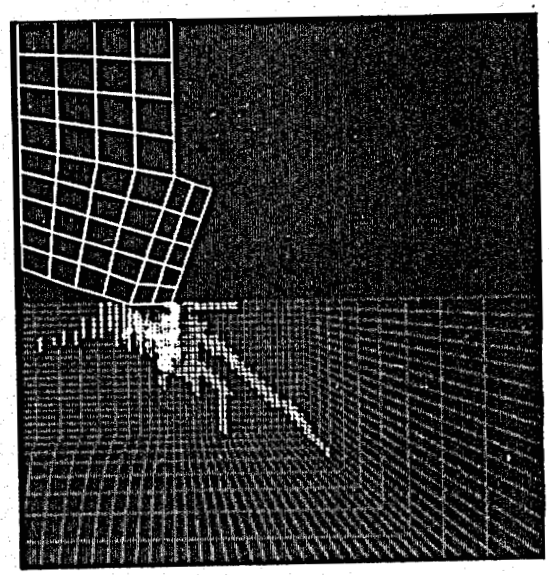

Figure 45: Predicted Fractures in Berea Sandstone for a Flat Rock Surface (0.002 inch Vertical Displacement) Case #2

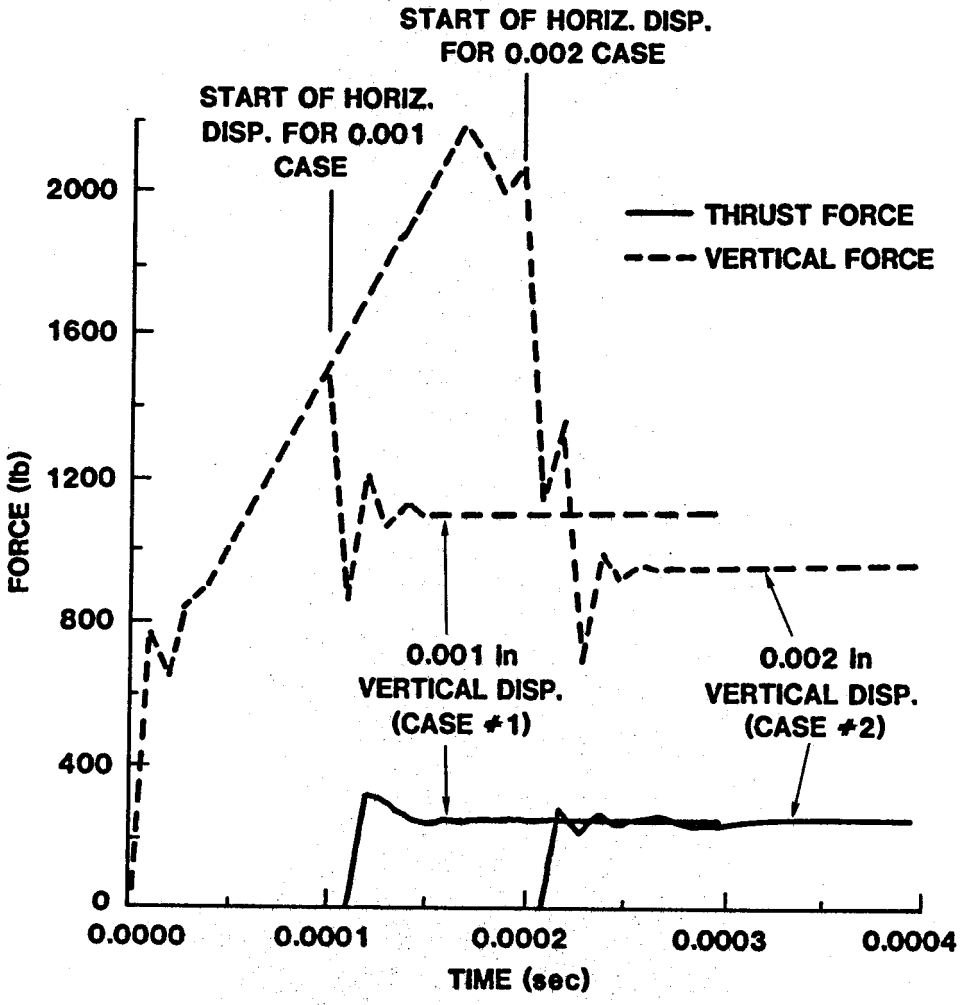

Figure 46: Predicted Cutter Loads for Berea Sandstone Flat Rock Surface Calculations (loads given for a 1 inch wide cutter) Cases #1 and #2

a. Initial Conditions

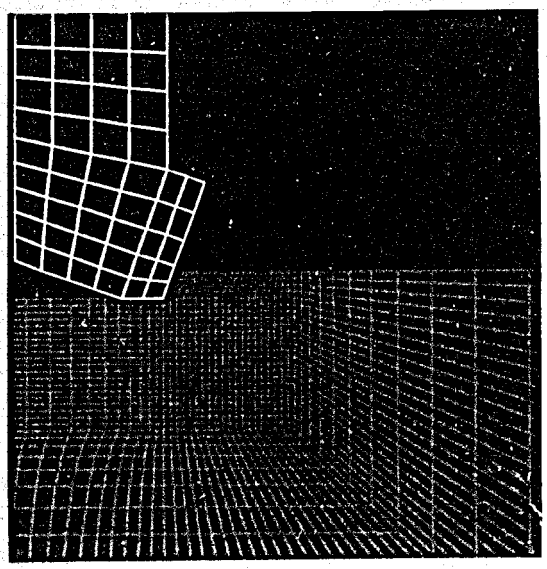

b. After 0.001 inch Horizontal Displacement

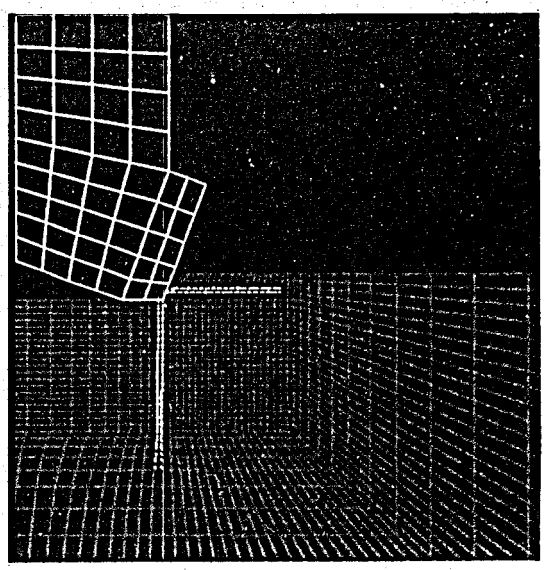

c. After 0.002 inch Horizontal Displacement

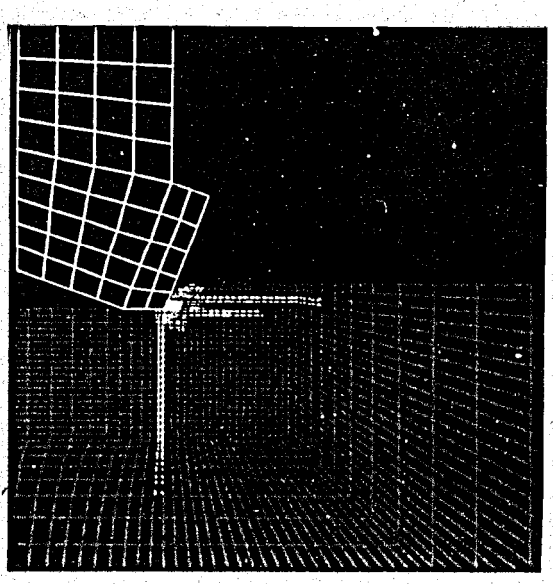

d. After 0.003 inch Horizontal Displacement

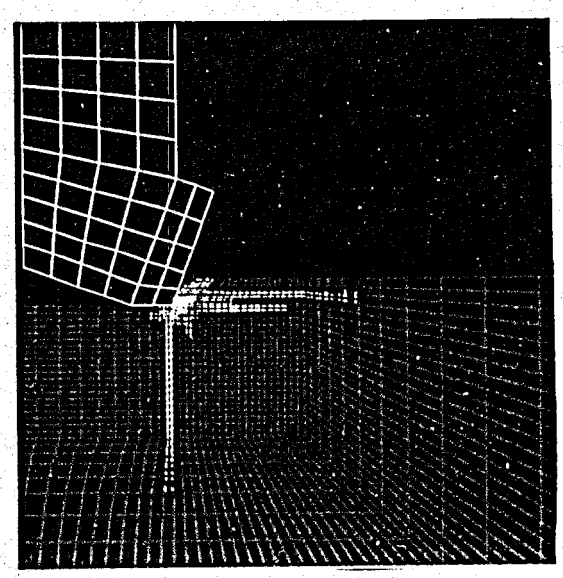

Figure 47: Predicted Fractures in Berea Sandstone for a 0.100 inch Cutting Depth, Tensile/Coulomb Model Case #3

a. Initial Conditions

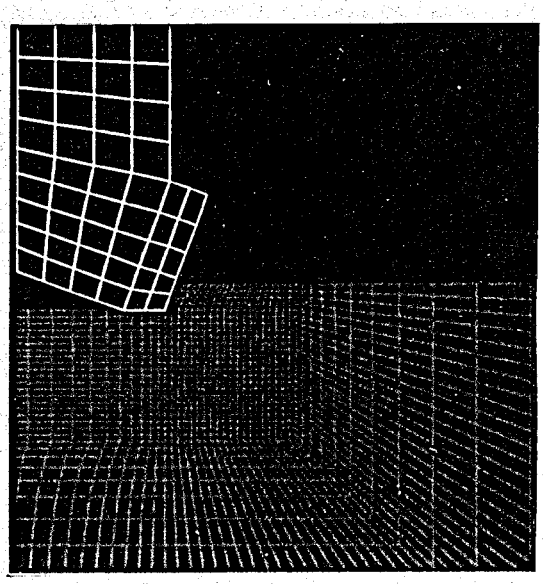

b. After 0.001 inch Horizontal Displacement

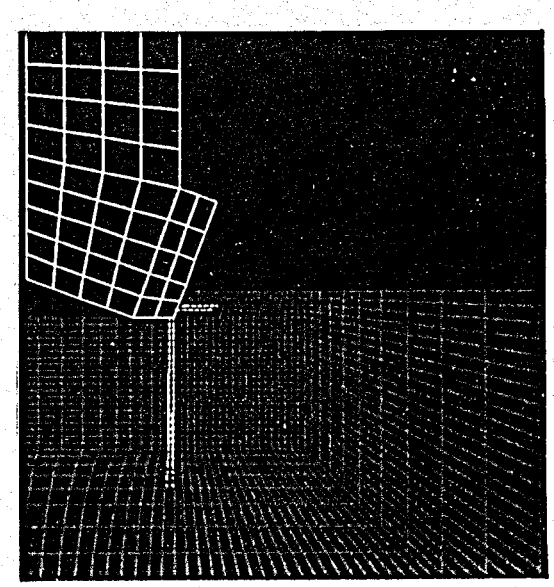

c. After 0.002 inch Horizontal Displacement

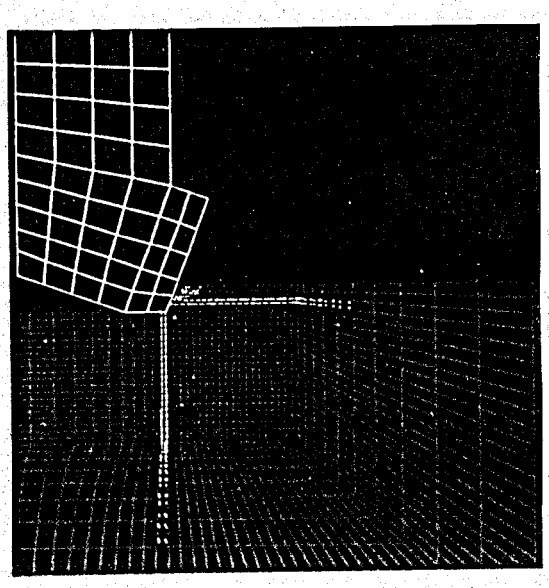

d. After 0.003 inch Horizontal Displacement

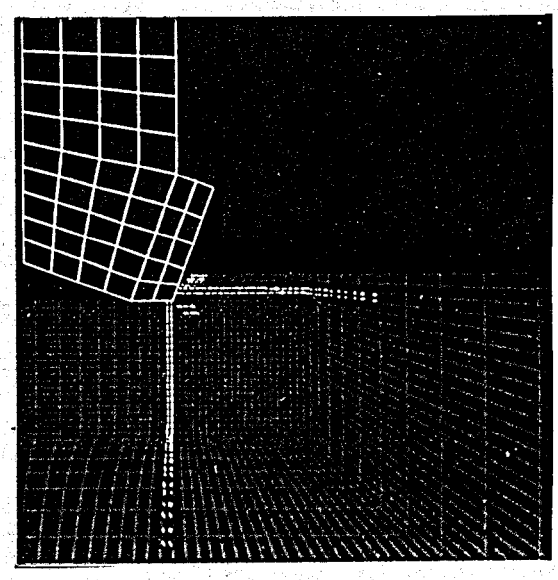

Figure 48: Predicted Fractures in Berea Sandstone for a 0.100 inch Cutting Depth, Tensile/Plasticity Model Case #4

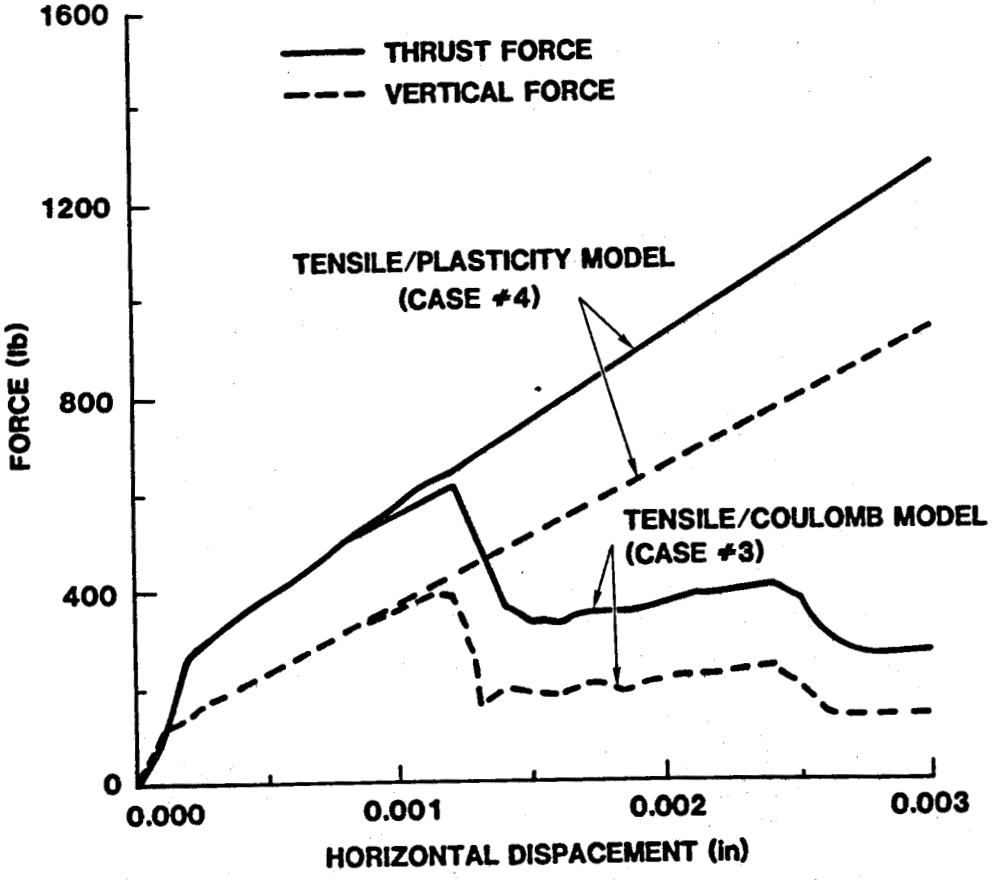

Figure 49: Predicted Cutter Loads for Berea Sandstone 0.100 inch Cutting Depth (loads given for a 1 inch wide cutter) Cases #3 and #4

a. Initial Conditions

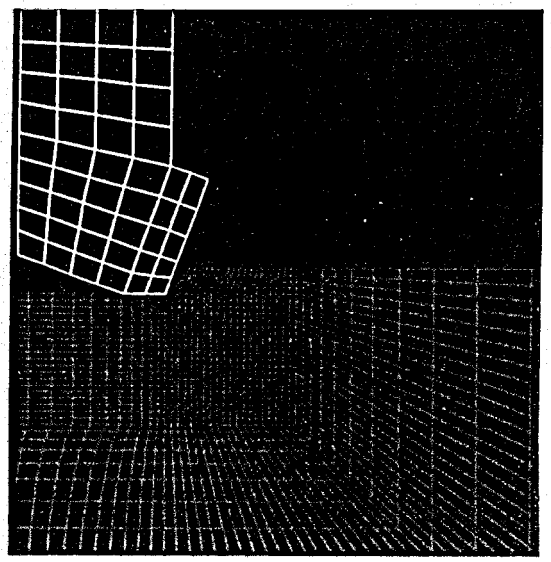

b. After 0.001 inch Horizontal Displacement

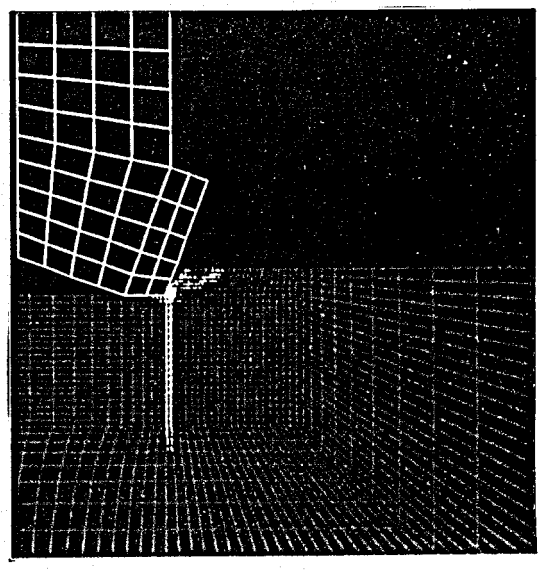

c. After 0.002 inch Horizontal Displacement

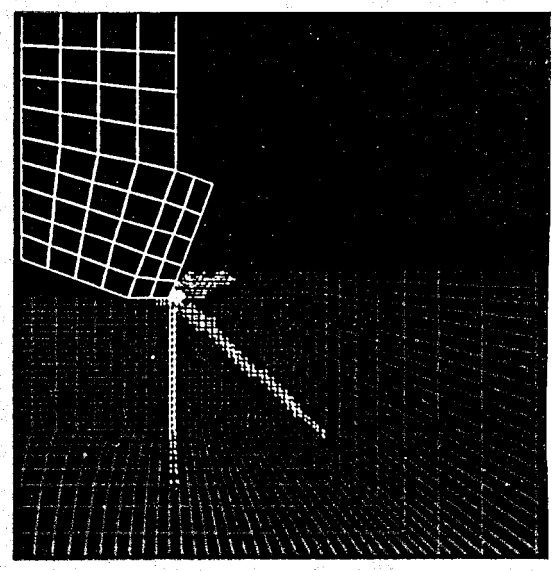

d. After 0.003 inch Horizontal Displacement

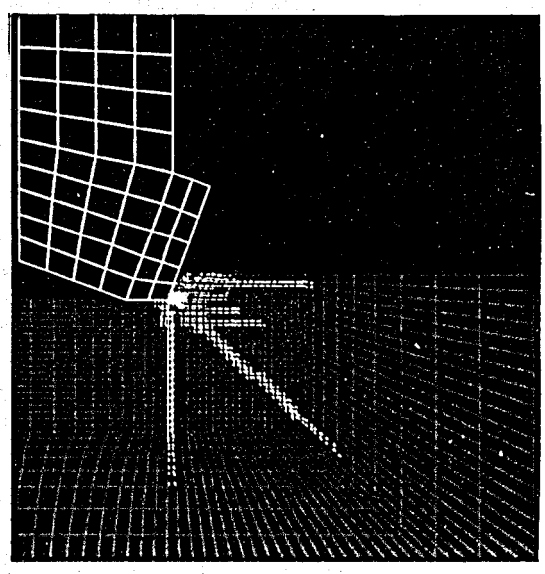

Figure 50: Predicted Fractures in Berea Sandstone for a 0.100 inch Cutting Depth, Tensile/Coulomb Model, Local Soft Region Under Cutter, Case #5

a. Initial Conditions

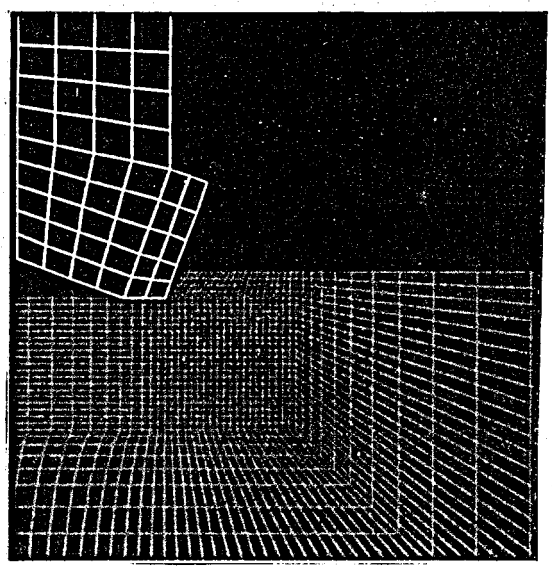

b. After 0.001 inch Vertical Displacement

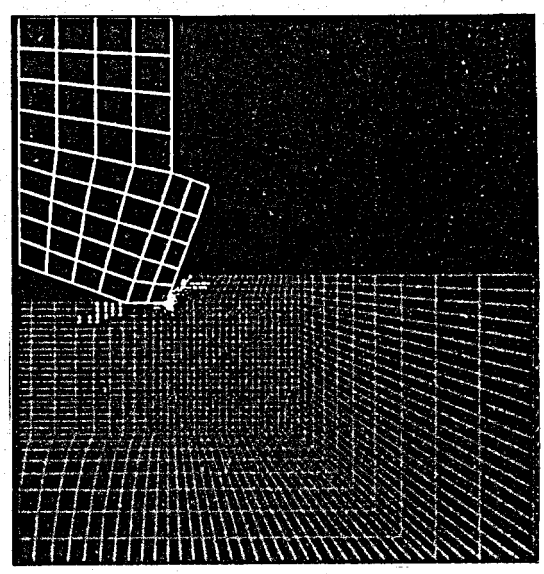

c. After 0.001 inch Horizontal Displacement (Vertical Displacement Held at 0.001 inch)

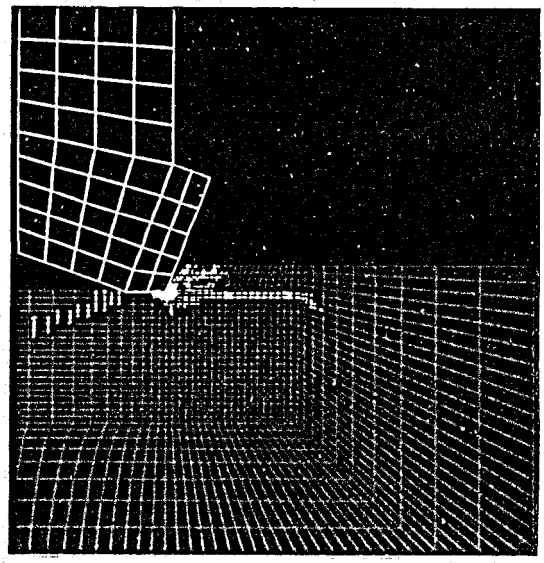

d. After 0.002 inch Horizontal Displacement (Vertical Displacement Held at 0.001 inch)

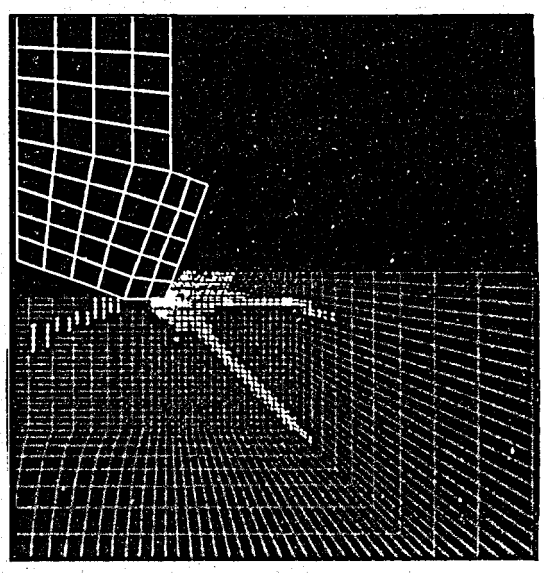

Figure 51: Predicted Fractures in Berea Sandstone for a 0.100 inch Cutting Depth, Tensile/Coulomb Model, Local Soft Region Under Cutter, 0.001 inch Vertical Displacement, Case #6

a. Initial Conditions

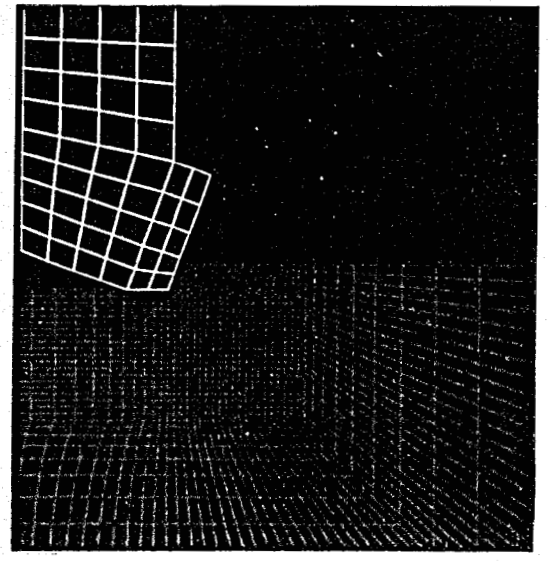

b. After 0.001 inch Vertical Displacement

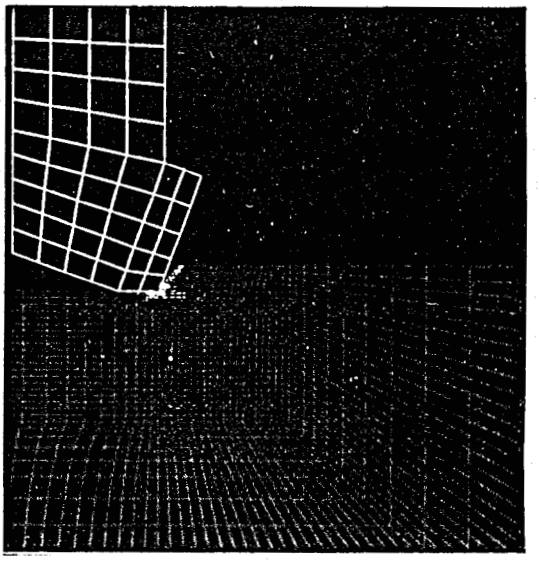

c. After 0.001 inch Horizontal Displacement (Vertical Displacement Held at 0.001 inch)

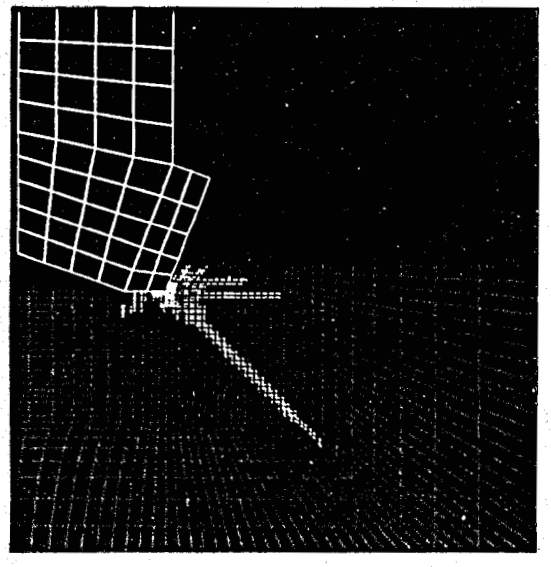

d. After 0.002 inch Horizontal Displacement (Vertical Displacement Held at 0.001 inch)

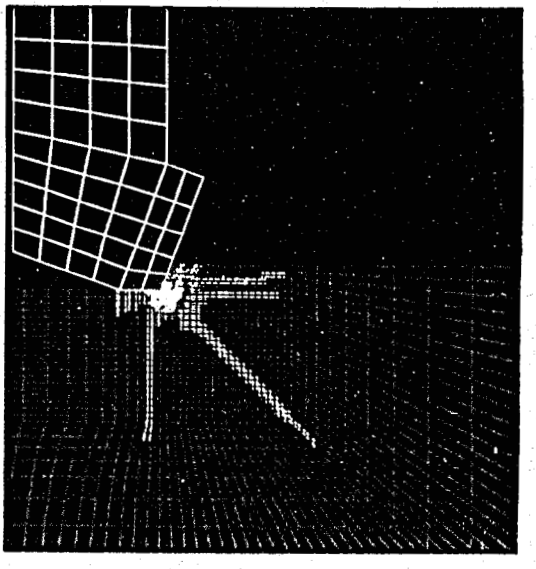

Figure 52: Predicted Fractures in Berea Sandstone for a 0.100 inch Cutting Depth, Tensile/Coulomb Model, Local Soft Region Under Cutter, 0.001 inch Vertical Displacement,0.001 inch Cutter Bottom Slope, Case #7

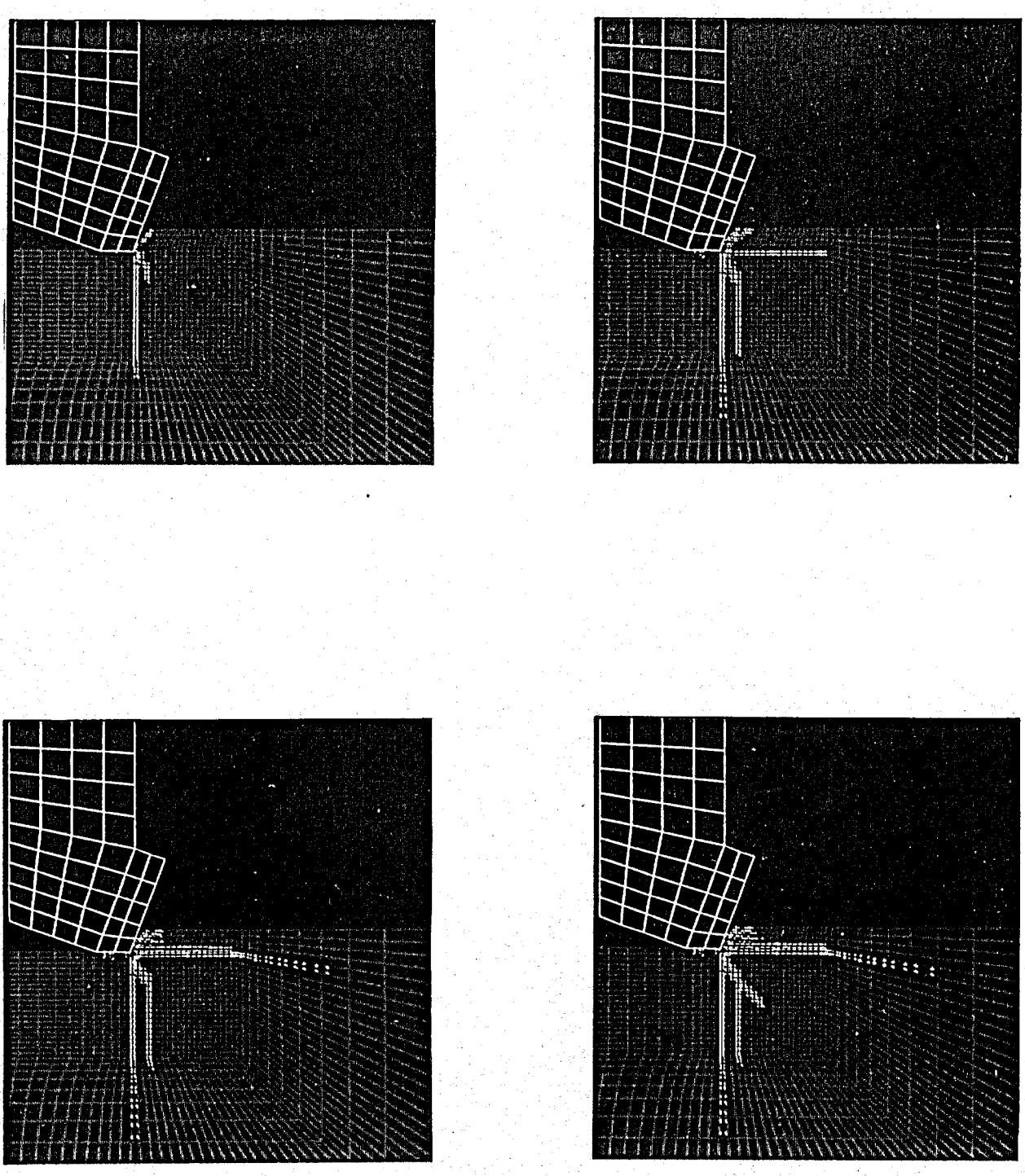

Figure 53: Predicted Fractures in Berea Sandstone for a 0.100 inch Cutting Depth, Tensile/Plasticity Model, Local Soft Region Under Cutter, 0.001 inch Vertical Displacement,0.001 inch Cutter Bottom Slope, Case #8

a. Vertical Loads

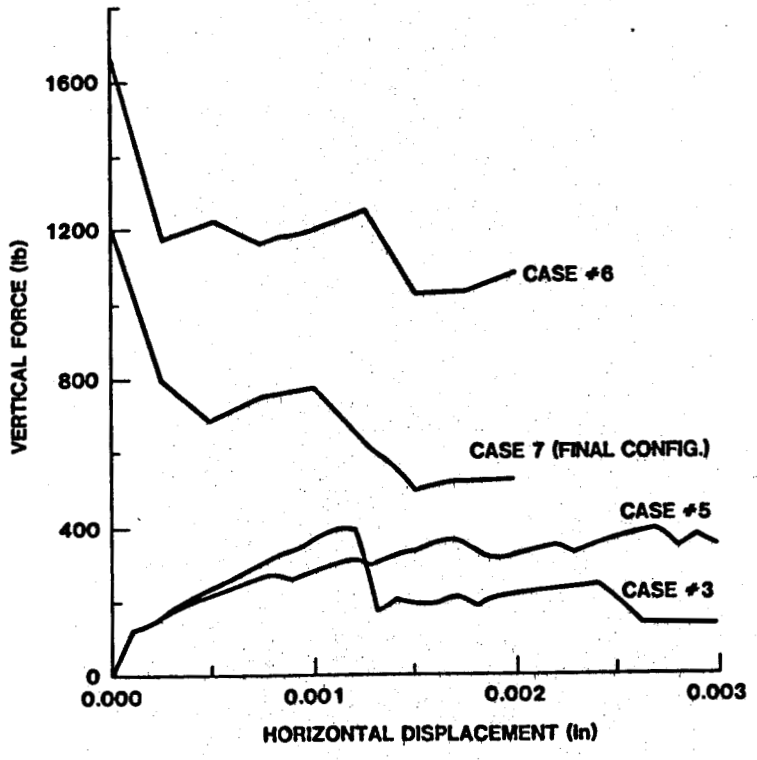

b. Horizontal Loads

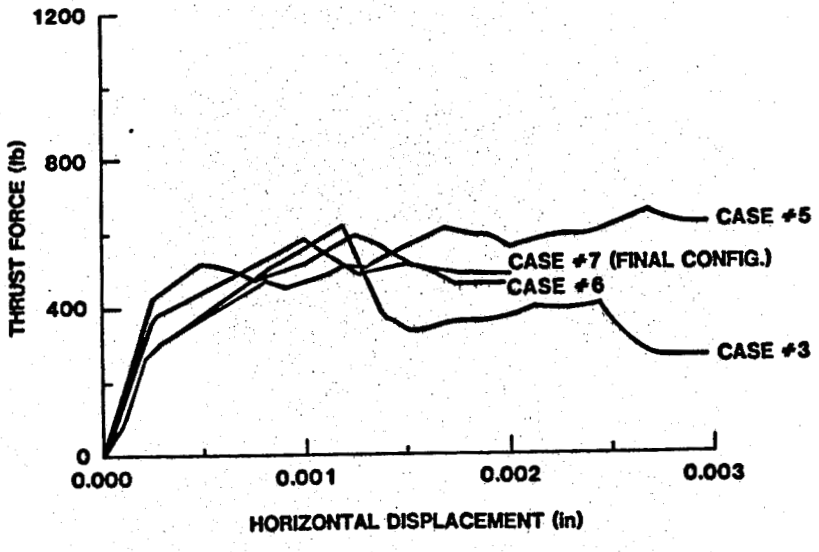

Figure 54: Effect of Changing Rock/Cutter Interface Details on Predicted Cutter Loads for Berea Sandstone 0.100 inch Cutting Depth (loads given for a 1 inch wide cutter) Cases #3, #5, #6, #7

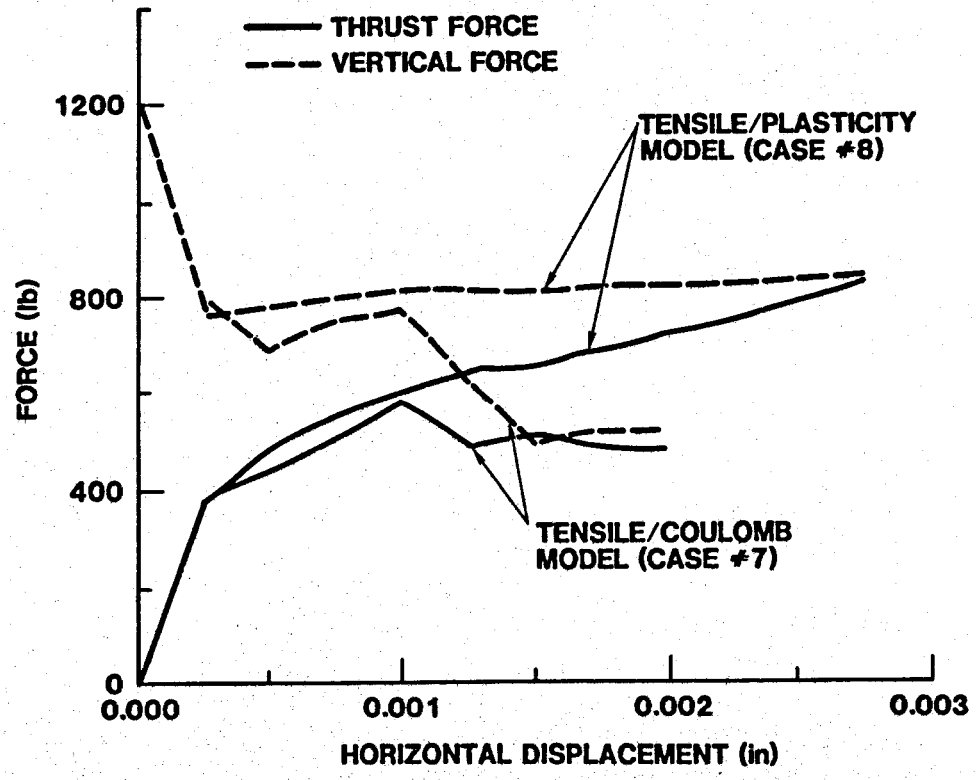

Figure 55: Comparison of Predicted Cutter Loads for Berea Sandstone 0.100 inch Cutting Depth Using the Two Constitutive Models Cases #7 and #8

a. Initial Conditions

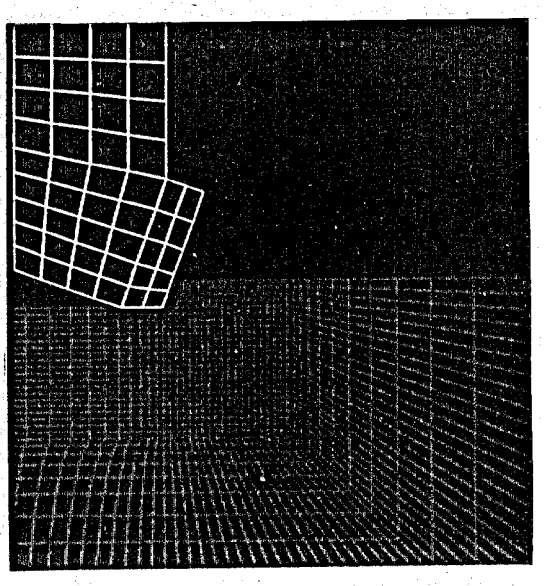

b. After 0.001 inch Vertical Displacement

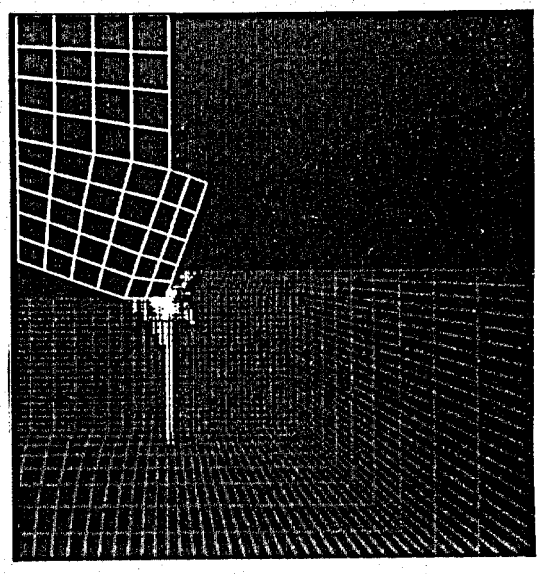

c. After 0.001 inch Horizontal Displacement (Vertical Displacement Held at 0.001 inch)

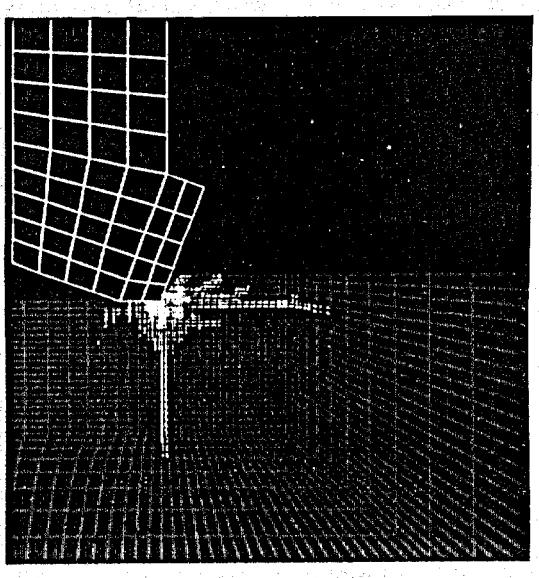

d. After 0.0015 inch Horizontal Displacement (Vertical Displacement Held at 0.001 inch)

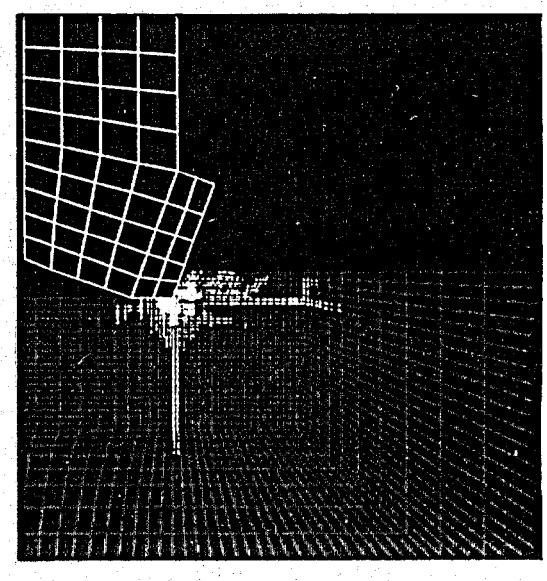

Figure 56: Predicted Fractures in Tennessee Marble for a 0.100 inch Cutting Depth, Tensile/Coulomb Model, Local Soft Region Under Cutter, 0.001 inch Vertical Displacement, 0.001 inch Cutter Bottom Slope, Case #9

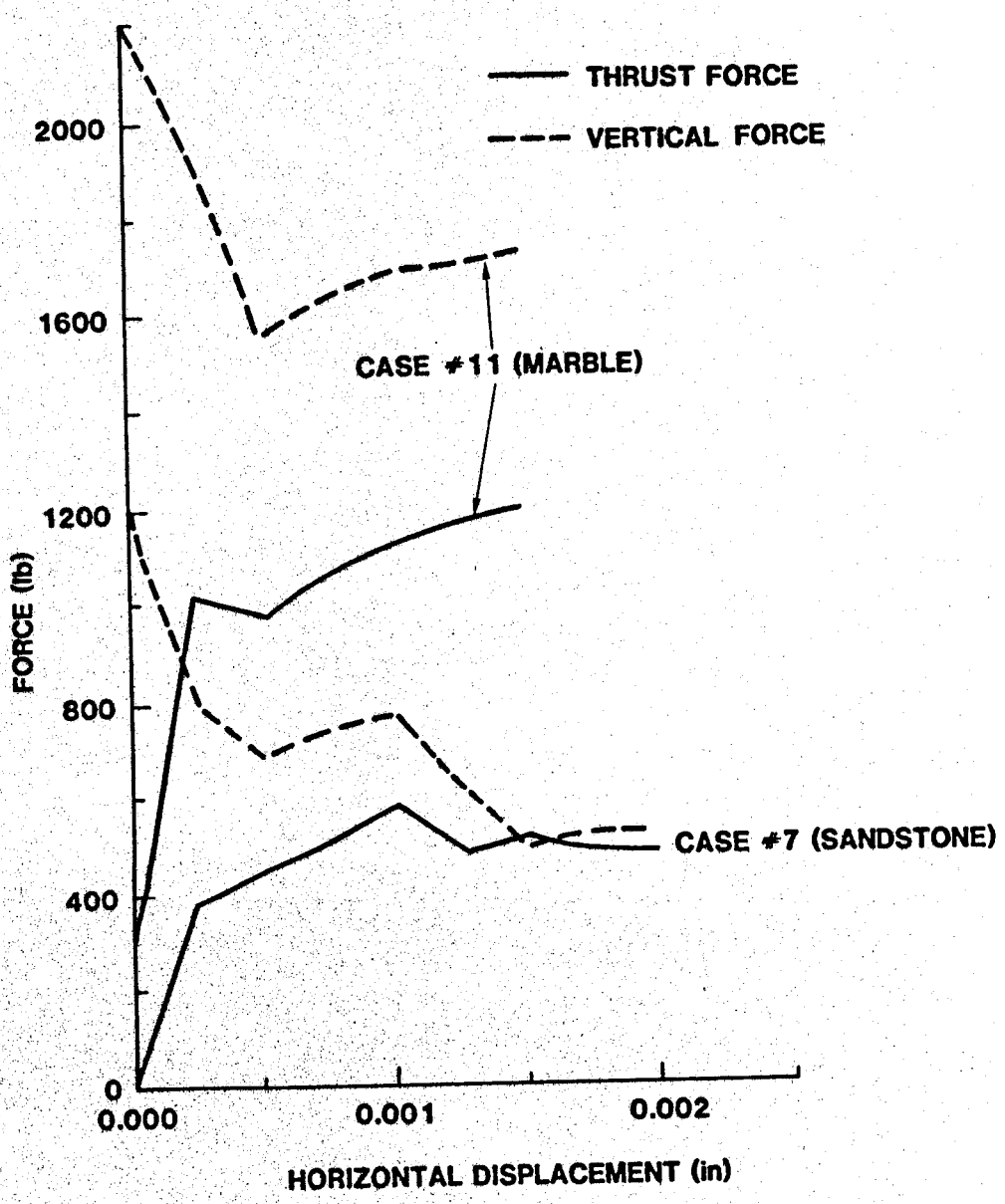

Figure 57: Comparison of Predicted Cutter Loads for Berea Sandstone and Tennessee Marble, 0.100 inch Cutting Depth (loads given for a 1 inch wide cutter) Case #7 and #9

a. After 0.001 inch Vertical Displacement

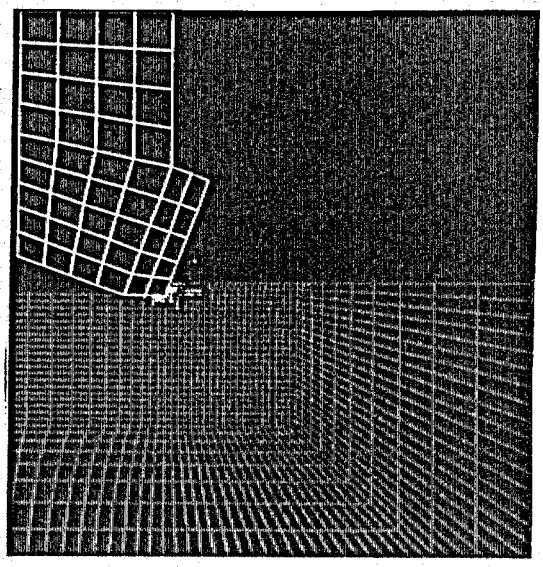

b. After 0.001 inch Horizontal Displacement (Vertical Displacement Held at 0.001 inch)

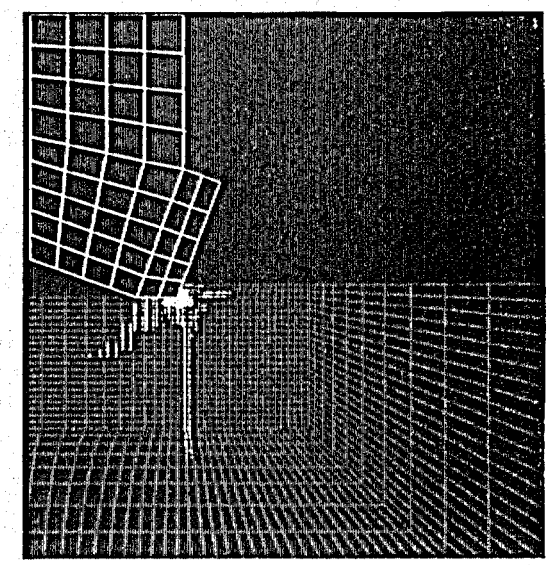

c. After 0.002 inch Horizontal Displacement (Vertical Displacement Held at 0.001 inch)

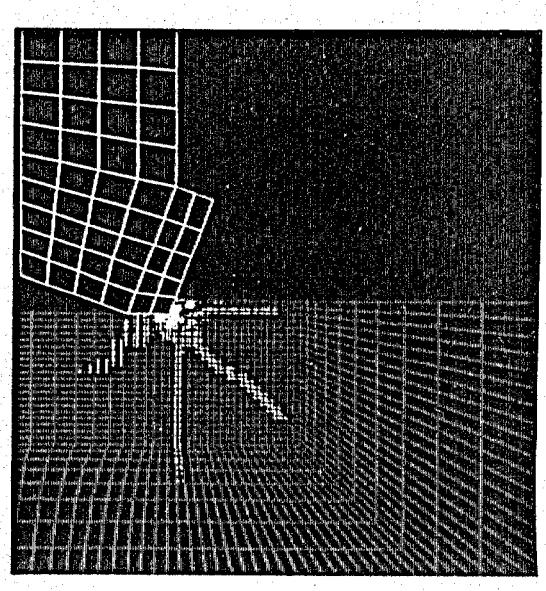

d. After 0.003 inch Horizontal Displacement (Vertical Displacement Held at 0.001 inch)

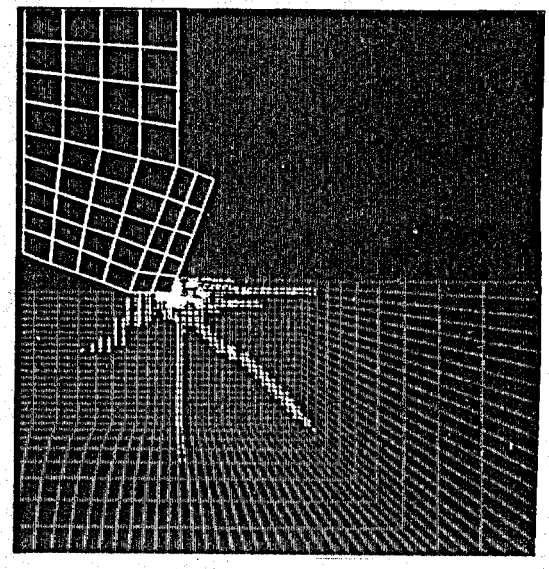

Figure 58: Predicted Fractures in Berea Sandstone for a 0.050 inch Cutting Depth, Tensile Coulomb Model, Local Soft Region Under Cutter, 0.001 inch Vertical Displacement, 0.001 inch Cutter Bottom Slope, Case #10

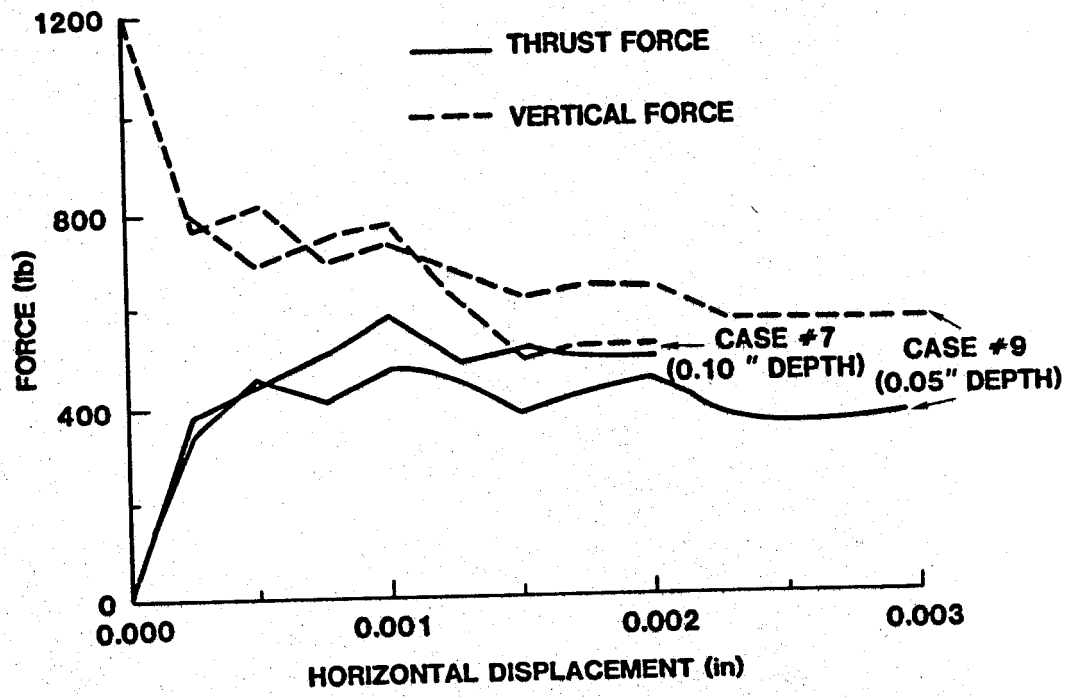

Figure 59: Comparison of Predicted Cutter Loads for Berea Sandstone with 0.100 and 0.050 inch Cutting Depths (loads given for a 1 inch wide cutter) Case #7 and #10

a. After 0.001 inch Vertical Displacement

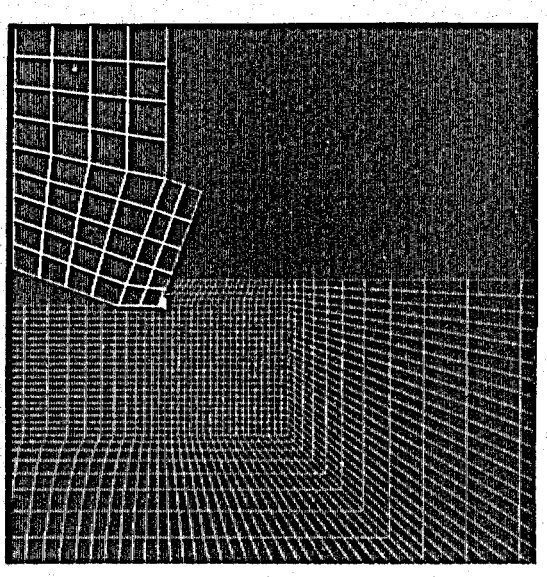

b. After 0.001 inch Horizontal Displacement (Vertical Displacement Held at 0.001 inch)

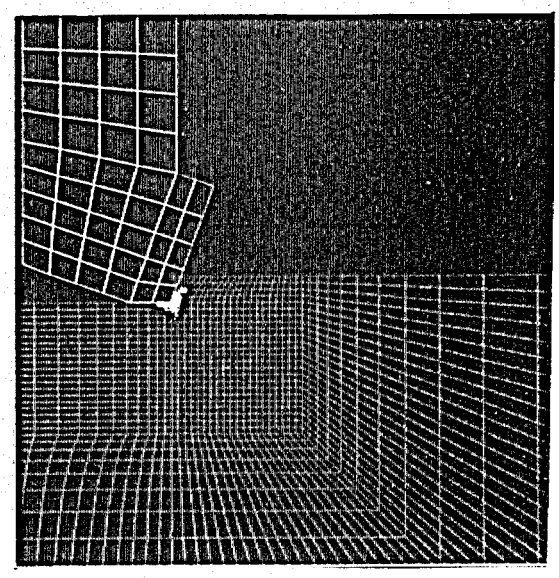

c. After 0.002 inch Horizontal Displacement (Vertical Displacement Held at 0.001 inch)

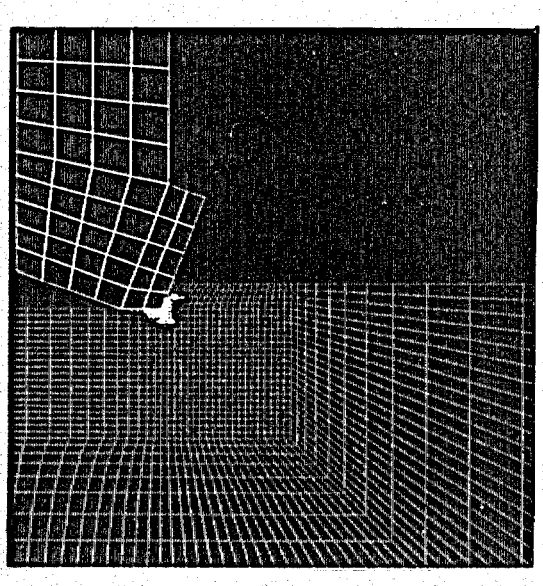

d. After 0.003 inch Horizontal Displacement (Vertical Displacement Held at 0.001 inch)

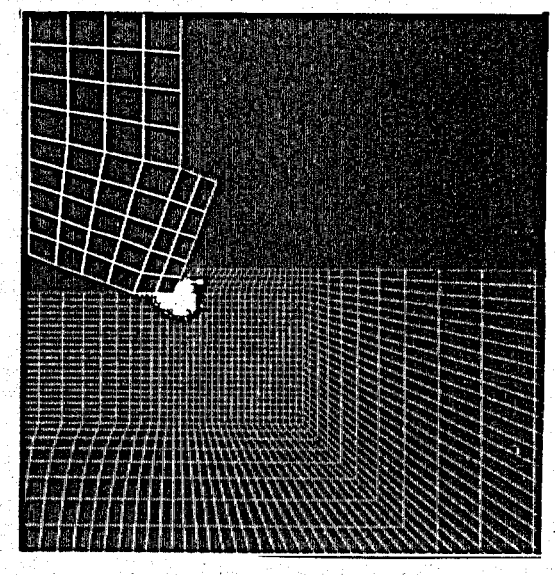

Figure 60: Predicted Fractures in Berea Sandstone for a 0.100 inch Cutting Depth, Tensile/Coulomb Model, Local Soft Region Under Cutter, 0.001 inch Vertical Displacement, 0.001 inch Cutter Bottom Slope, Confining Pressure of 3,000 psi, Case #11

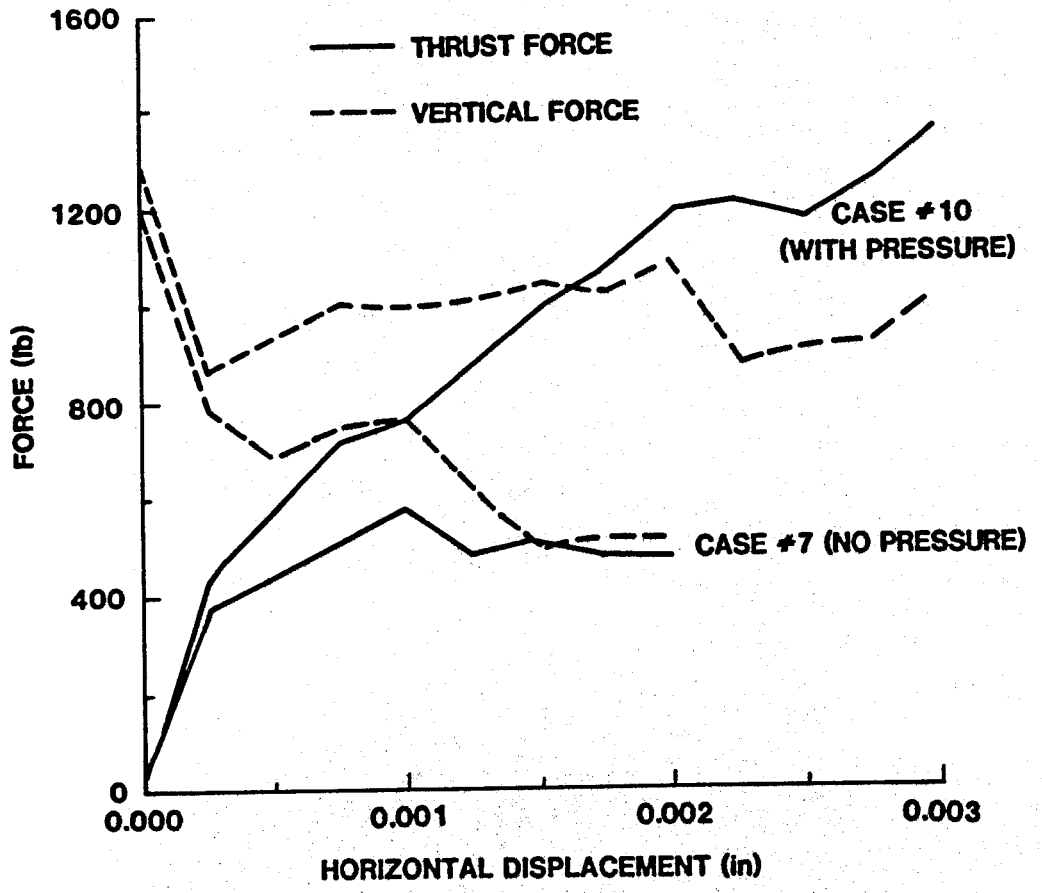

Figure 61: Comparison of Predicted Cutting Loads With and Without Confining Pressure, Berea Sandstone, 0.100 inch Cutting Depth, Cases #7 and #11

DISTRIBUTION:
RE/SPEC Inc.
PO Box 14984
Albuquerque, NM 87191
Attn: S. W. Key

TPL Inc.
3409 Bryn Mawr NE
Albuquerque, NM 87107
Attn: H. M. Stoller

NMERI
Campus
PO Box 25
Albuquerque, NM 897131
Attn: H. L. Schreyer

Drilling Resources
Development Corp.
Suite 415
Skyline East 1 Bldg
6111 East Skelly Dr
Tulsa, OK 74135
Attn: S. Jordan

Kenroc Tools Ltd
3370 Dundas St. West
Toronto, ONTARIO M6S 2S2
Attn: J. Chan

Reed Rock Bit Co.
PO Box 2119
Houston, TX 77001
Attn: Dr. G. C. Feng
P. E. Pastusek
B. Schwind

Venture Innovation
PO Box 35845
Houston, TX 77035
Attn: T. Anderson

Shell Oil Company
Two Shell Plaza
PO Box 2099
Houston, TX 77001
Attn: E. Bingman

Dyna-Drill
PO Box C-19576
Irvine, CA 92713
Attn: L. Diamond

NL Petroleum Services
PO Box 60087
Houston, TX 77205
Attn: J. E. Fontenot
D. L. Wesenberg

Texas A&M University
Center for Tectonophysics
and Dept. of Geology
College Station, TX 77843
Attn: Dr. M. Friedman
Professor of Geology

Phillips Petroleum Company
Geothermal Operations
655 East 4500 South
Salt Lake City, UT 84107
Attn: T. Turner

Smith Tool
Geothermal Operations
PO Box C-19511
Irvine, CA 92713
Attn: J. Kingsolver

Dresser Industries, Inc.
Security Division
PO Box 24647
Dallas, TX 75224
Attn: J. W. Langford

Harvey E. Mallory
PO Box 54696
Tulsa, OK 74155

NL Baroid
6400 Uptown Blvd NE, 365W
Albuquerque, NM 87110
Attn: G. Polk

Union Oil Co. of California
Union Geothermal Division
Union Oil Center
Los Angeles, CA 90017
Attn: D. E. Pyle

Los Alamos National Labs
Mail Stop 570
Los Alamos, NM 87545
Attn: J. C. Rowley

Otis Research Development
PO Box 34380
Dallas, TX 75234
Attn: W. D. Rumbaugh

Halliburton
Drawer 1431
Duncan, OK 73533
Attn: D. Smith

Amoco Production Company
Research Center
PO Box 591
Tulsa, OK 74102
Attn: T. Warren

Superior Oil
Eastern Division
PO Box 51108 OCS
Layayett, LA 70505
Attn: E. Martin
S. C. Malguarnera

B. J. Livesay
129 Liverpool
Cardiff, CA 92007

US Department of (4)
Energy
Geothermal Hydropower
Technologies Division
Forrestal Bldg, CE 324
1000 Independence Ave SW
Washington, DC 20585
Attn: J. Bresee
D. Clements
R. Toms
D. Allen

W. P. Grace
Nuclear & Geosciences
Division
DOE/ALO

Systems, Science,
and Software
3398 Carmel Mt. Road
San Diego, CA 92121
Attn: K. J. Cheverton

Schluberger
Drilling and Production
Services
42, rue Saint Dominique
75007 Paris
FRANCE
Attn: B. Vivet

Stanford University
Division of Applied
Mechanics
Department of Mechanical
Engineering
Stanford, CA 94305
Attn: T. J. R. Hughes

D. Hibbitt
Hibbitt, Karlson
and Sorensen, Inc.
35 South Angell St.
Providence, RI 02906

MARC Analysis Research
Corporation
260 Sheridan Ave, Suite 314
Palo Alto, CA 94306
Attn: J. Nagtegaal

Swanson Engineering Assoc.
340 S. Washington Road
McMurray, PA 15317
Attn: J. Swanson

GTE Laboratories
40 Sylvan Road
Waltham, MA 02254
Attn: R. Joshi

A. R. Ingraffea
School of Civil and
Environ. Engineering
Hollister Hall
Cornell University
Ithaca, NY 14853

Christensen Diamond Products
PO Box 387
1937 S. 300 West
Salt Lake City, UT 94110
Attn: B. Iversen

Shell Development Co.
Bellaire Research Center
PO Box 481
Houston, TX 77001

CIRES
PO Box 449
University of Colorado
Boulder, CO 80309
Attn: N. Brodsky

Peter Leary
Dept. of Geological Sciences
Univ. of Southern California
Los Angeles, CA 90089

Steve Benzley
368 CB
Brigham Young University
Provo, UT 84602

R. H. Atkinson
Atkinson-Noland and
Associates
2619 Spruce Street
Boulder, CO 80302

Michael Hood
Dept. of Material Science
and Mineral Engineering
Univeristy of California
Berkeley, CA 94720

Victor E. Saouma
School of Engineering
Univ. of Pittsburgh
934 Benedum Hall
Pittsburgh, PA 15261

John Cheatham
Dept. of Mechanical
Engineering
Rice University
Houston, TX 77001

W. C. Maurer
Maurer Engineering, Inc
2916 West T. C. Jester
Houston, TX 77018

Stratabit
600 Kenrick
Suite A-1
Houston, TX 77060
Attn: Terry Dailey
Larry Matson

1510	D. B. Hayes
1520	T. B. Lane
1521	R. D. Krieg
1521	C. M. Stone
1522	T. G. Priddy
1524	W. N. Sullivan
1524	D. V. Swenson (30)
1524	L. M. Taylor
1524	R. K. Thomas
1530	L. W. Davison
1533	P. Yarrington
1540	W. C. Luth
1542	B. M. Butcher
9700	E. H. Beckner
9730	W. D. Weart
9740	R. K. Traeger
9741	J. R. Kelsey (20)
9741	J. T. Finger (20)
9747	P. J. Hommert
9750	V. L. Dugan
9752	L. M. Ford
9753	D. A. Northrop
8214	M. A. Pound
3141	L. J. Erickson (5)
3151	W. L. Garner (3)
3154-3	C. H. Dalin (25) for DOE/TIC (Unlimited Release)